



# **Development of a miniaturized microscope for depth-scanning imaging at subcellular resolution in freely behaving animals**

**Thèse**

**Arutyun Bagramyan**

**Doctorat en physique**  
Philosophiæ doctor (Ph. D.)

Québec, Canada

# **Development of a miniaturized microscope for depth-scanning imaging at subcellular resolution in freely behaving animals**

**Thèse**

**Arutyun Bagramyan**

Sous la direction de:

Tigran Galstian, directeur de recherche



# Résumé

Le fonctionnement du cerveau humain est fascinant. En seulement quelques millisecondes, des milliards de neurones synchronisés perçoivent, traitent et redirigent les informations permettant le contrôle de notre corps, de nos sentiments et de nos pensées. Malheureusement, notre compréhension du cerveau reste limitée et de multiples questions physiologiques demeurent. Comment sont exactement reliés le fonctionnement neuronal et le comportement humain ?

L'imagerie de l'activité neuronale au moyen de systèmes miniatures est l'une des voies les plus prometteuses permettant d'étudier le cerveau des animaux se déplaçant librement. Cependant, le développement de ces outils n'est pas évident et de multiples compromis techniques doivent être faits pour arriver à des systèmes suffisamment petits et légers. Les outils actuels ont donc souvent des limitations concernant leurs caractéristiques physiques et optiques. L'un des problèmes majeur est le manque d'une lentille miniature électriquement réglable et à faible consommation d'énergie permettant l'imagerie avec un balayage en profondeur.

Dans cette thèse, nous proposons un nouveau type de dispositif d'imagerie miniature qui présente de multiples avantages mécaniques, électriques et optiques par rapport aux systèmes existants. Le faible poids, la petite dimension, la capacité de moduler électriquement la distance focale à l'aide d'une lentille à cristaux liquides (CL) et la capacité d'imager des structures fines sont au cœur des innovations proposées. Dans un premier temps, nous présenterons nos travaux (théoriques et expérimentaux) de conception, assemblage et optimisation de la lentille à CL accordable (TLCL, pour *tunable liquid crystal lens*). Deuxièmement, nous présenterons la preuve de concept macroscopique du couplage optique entre la TLCL et la lentille à gradient d'indice (GRIN, pour *gradient index*) en forme d'une tige. Utilisant le même système, nous démontrerons la capacité de balayage en profondeur dans le cerveau des animaux anesthésiés. Troisièmement, nous montrerons un dispositif d'imagerie (2D) miniature avec de nouvelles caractéristiques mécaniques et optiques permettant d'imager de fines structures neuronales dans des tranches de tissus cérébraux fixes. Enfin, nous présenterons le dispositif miniaturisé, avec une TLCL intégrée. Grâce à notre système, nous obtenons  $\approx 100 \mu\text{m}$  d'ajustement électrique de la profondeur d'imagerie qui permet d'enregistrer l'activité de fines structures neuronales lors des différents comportements (toiletage, marche, etc.) de la souris.

# Abstract

The functioning of the human brain is fascinating. In only a few milliseconds, billions of finely tuned and synchronized neurons perceive, process and exit the information that drives our body, our feelings and our thoughts. Unfortunately, our understating of the brain is limited and multiple physiological questions remain. How exactly are related neural functioning and human behavior ?

The imaging of the neuronal activity by means of miniaturized systems is one of the most promising avenues allowing to study the brain of the freely moving subjects. However, the development of these tools is not obvious and multiple technical trade-offs must be made to build a system that is sufficiently small and light. Therefore, the available tools have different limitations regarding their physical and optical characteristics. One of the major problems is the lack of an electrically adjustable and energy-efficient miniature lens allowing to scan in depth.

In this thesis, we propose a new type of miniature imaging device that has multiple mechanical, electrical and optical advantages over existing systems. The low weight, the small size, the ability to electrically modulate the focal distance using a liquid crystal (LC) lens and the ability to image fine structures are among the proposed innovations. First, we present our work (theoretical and experimental) of design, assembling and optimization of the tunable LC lens (TLCL). Second, we present the macroscopic proof-of-concept optical coupling between the TLCL and the gradient index lens (GRIN) in the form of a rod. Using the same system, we demonstrate the depth scanning ability in the brain of anaesthetized animals. Third, we show a miniature (2D) imaging device with new mechanical and optical features allowing to image fine neural structures in fixed brain tissue slices. Finally, we present a state-of-the-art miniaturized device with an integrated TLCL. Using our system, we obtain a  $\approx 100 \mu\text{m}$  electrical depth adjustment that allows to record the activity of fine neuronal structures during the various behaviours (grooming, walking, etc.) of the mouse.

# Contents

<b>Résumé</b>	<b>iii</b>
<b>Abstract</b>	<b>iv</b>
<b>Contents</b>	<b>v</b>
<b>List of Tables</b>	<b>vii</b>
<b>List of Figures</b>	<b>viii</b>
<b>Acknowledgements</b>	<b>xii</b>
<b>Foreword</b>	<b>xiii</b>
<b>Introduction</b>	<b>1</b>
I.1 Imaging, the power of light . . . . .	1
I.2 Fluorescence, imaging the brain . . . . .	2
I.3 <i>In vivo</i> , benchtop systems . . . . .	3
I.4 <i>In vivo</i> , miniaturized systems . . . . .	5
I.5 Summary of existing limitations . . . . .	8
I.6 Liquid crystals . . . . .	10
<b>1 Dynamic control of polarisation mismatch and coma aberrations in rod GRIN assemblies</b>	<b>20</b>
1.1 Résumé . . . . .	20
1.2 Abstract . . . . .	21
1.3 Introduction . . . . .	21
1.4 Coma aberration . . . . .	22
1.5 Polarization aberration . . . . .	25
1.6 Discussions and conclusions . . . . .	28
1.7 Appendix . . . . .	29
<b>2 Motion-free endoscopic system for brain imaging at variable focal depth using liquid crystal lenses</b>	<b>31</b>
2.1 Résumé . . . . .	31
2.2 Abstract . . . . .	32
2.3 Introduction . . . . .	32
2.4 Materials and methods/experimental . . . . .	35
2.5 Results and discussion . . . . .	41

2.6	Conclusion . . . . .	50
<b>3</b>	<b>Lightweight 1-photon miniscope for imaging in freely behaving animals at subcellular resolution</b>	<b>51</b>
3.1	Résumé . . . . .	51
3.2	Abstract . . . . .	51
3.3	Introduction . . . . .	52
3.4	Design and fabrication . . . . .	52
3.5	Results and discussion . . . . .	56
3.6	Conclusion . . . . .	59
<b>4</b>	<b>Focus tunable microscope for subcellular imaging in freely behaving animals</b>	<b>60</b>
4.1	Résumé . . . . .	60
4.2	Abstract . . . . .	61
4.3	Introduction . . . . .	61
4.4	Results . . . . .	62
4.5	Discussion . . . . .	70
4.6	Appendix . . . . .	72
	<b>Conclusion</b>	<b>76</b>
5.1	Summary . . . . .	76
5.2	Conclusions . . . . .	79
5.3	Future developments . . . . .	79
	<b>Publication</b>	<b>81</b>
	<b>Bibliography</b>	<b>82</b>

# List of Tables

I.1	Comparison between the TLCL and the EWL . . . . .	18
1.1	Values of drive parameters used for obtaining minimal polarization mismatch	26
2.1	Resolution table of three different imaging configurations . . . . .	44

# List of Figures

I.1	Functioning and biological application of the fluorescent proteins . . . . .	2
I.2	Benchtop 2-photon microscope design adapted for <i>in vivo</i> imaging . . . . .	4
I.3	Miniaturized 1-photon microscope design . . . . .	5
I.4	Miniaturized multi-photon microscope designs . . . . .	7
I.5	Different phases of matter . . . . .	10
I.6	Different states of matter, thermotropic LCs . . . . .	11
I.7	Elongated elliptic model of NLCs . . . . .	12
I.8	Electrical alignment of LC molecules . . . . .	14
I.9	Tunable LC cell . . . . .	15
I.10	Resistivity and distribution of the electrical field . . . . .	16
I.11	Rubbing and the alignment LC molecules . . . . .	17
I.12	Miniaturised depth scanning devices . . . . .	18
1.1	Optical power, RMS aberrations and coma versus control frequency . . . . .	23
1.2	Demonstration of the strong coma correction using 2 TLCLs . . . . .	24
1.3	Schematic demonstration of one possible TLCL stacking option and polarization mismatch correction . . . . .	26
1.4	Characterization of the impact of polarization mismatch on the quality of images . . . . .	28
1.5	Polarimetry set-up . . . . .	29
1.6	Shack-Hartmann set-up . . . . .	29
2.1	Schematic representation of the TLCL . . . . .	34
2.2	The optical probe and experimental set-up . . . . .	40
2.3	Characterization of the TLCL . . . . .	42
2.4	Characterization of the optical resolution of the assembly in the water . . . . .	43
2.5	Imaging granule neurons in the adult olfactory bulb in thick brain sections . . . . .	45
2.6	Imaging dendrites and spines with the optical probe assembly . . . . .	47
2.7	Motion-free variable-depth <i>in vivo</i> imaging of interneurons in the adult mouse cortex . . . . .	48
2.8	Motion-free variable-depth <i>in vivo</i> imaging of interneurons in the adult OB . . . . .	49
3.1	Design of the proposed M1S . . . . .	53
3.2	Optical probe assembly . . . . .	54
3.3	Schematics of the developed system . . . . .	55
3.4	Resolution characterization . . . . .	56
3.5	Imaging with the developed M1S system . . . . .	58
4.1	Tunable liquid crystal lens design and characterisation . . . . .	64
4.2	Schematic presentation of the ensemble of the imaging system . . . . .	65

4.3	Electrical focal shift and characterisation of optical parameters of the mDS1s .	66
4.4	Time-lapse imaging of $\text{Ca}^{2+}$ activity from GCaMP6s-labeled neurons of the motor cortex . . . . .	68
4.5	Electrical focus adjustment and time-lapse imaging of $\text{Ca}^{2+}$ activity from neuronal structures in the motor cortex of a freely behaving animal . . . . .	69
4.6	Characterization of the TLCL . . . . .	72
4.7	Portability test of the mDS1s . . . . .	73

*To my beloved mother, father, sister  
and my beautiful girlfriend who  
helped me all the way through this  
long Journey.*



The best way out of a difficulty is  
through it.

---

Will Rogers

# Acknowledgements

It has been a long journey. Now that I look at all these years that I have spent to complete this work, I clearly see that I could not do it without the help of many people who stand alongside me and supported me. For that, I want to thank them.

First, I would like to thank Professor Tigran Galstian for his support and supervision. This work had plenty of difficulties, repeated ups and downs and without the constant support of Prof. Galstian, nothing would have been possible. His scientific knowledge, rigour and passion are inspiring and I truly consider myself lucky, to be around and to learn as much as I can from the best.

I would like also to thank technicians Éric Rousseau, Stéphane Gagnon and Patrick Larochelle for their help. Their professionalism and wise advises were key to the success of the project. Thank you for your patience, curiosity and generosity, always giving 100% of what was possible. After all these hours we passed together, all this work, I truly consider you as my friends rather than simple colleagues. Thank you !

I would like to thank my friends in both departments: physics and biology. Here I thinking about Loïc Tabourin, Louis Bégel, Justin Stevens, Marc-Antoine Boulé, Oleksandr Sova, Anastasiia Pusenkova, Ali Rastqarfarajzadeh, Cedric Bressan, Sarah Malvaut, Archana Gengatharan, Delphine Hardy, Bakhshetyan Karen, Ruggiero Francavilla, etc. Thank you guys for your support and everyday energy ! Our laughs, brainstorming moments, dinner evenings, sports and many other activities were amazing. I wish you success in finishing your studies and hope you will find a job that completes you and makes you happy. All the best !!

Finally, but probably most importantly, I would like to thank my family. My father, my mother, my sister and my girlfriend who were of indescribable support. They made me believe in myself, gave me confidence and support so I can pursue my studies, going this far. Each difficulty I had, each time I was down, they were present, giving me the energy and motivation to continue. For their unconditional love and support, I would like to kindly thank them. Love you guys !

# Foreword

This thesis presents the development of a miniaturized epifluorescence microscope system with integrated liquid crystal lens enabling electrical modulation of the focal distance. The detailed optical design, fabrication, characterization and the experimental utility of the device will be presented. Various mechanical and optical novelties will also be discussed alongside the potential application ideas. This thesis has five chapters. The first chapter is the **Introduction**, where I present the subject, existing limitations and our motivation for the development of a miniaturized depth scanning imaging system. The historical review of anterior miniaturized systems and the description of the liquid crystal lens are also presented to help better understand the upcoming chapters.

Each of 4 **chapters** corresponds to an article published or submitted for publication during my doctorate studies. Note that the original text content has been preserved while the numbering of legends of the equations, tables, figures and references has been adapted to the layout of the thesis. This work was carried out under the supervision of Tigran Galstian at the Center for Optics, Photonics and Laser at Laval University. The contribution of collaborators and co-authors of the papers will be explained.

**Chapter 1:** A. Bagramyan, T. Galstian, "Dynamic control of polarization mismatch and coma aberrations in rod-GRIN assemblies," *Optics Express*, OE 27, 14144–14151 (2019).

*This paper presents the development of small diameter liquid crystal lens adapted for our application. The utility of the lens, correction of optical aberrations and compensation of the polarisation miss-match are presented. My role in this publication was to design-build-characterize different liquid crystal lenses under the supervision of professor T. Galstian.*

**Chapter 2:** A. Bagramyan, A. Saghatelian, T. Galstian, "Motion-free endoscopic system for brain imaging at variable focal depth using liquid crystal lenses," *Journal of Biophotonics* 10, 762–774 (2017).

*Prior to the miniaturisation, the developed liquid crystal lens was integrated and tested in a macroscopic imaging system. The experimental utility of the lens was demonstrated by electrically adjusting the focal plane position in the brain of anesthetized, head restrained animals. My role in this publication was to design-build-characterize, the optical set-up under the supervision of*

*Professor T. Galstian. I also performed the surgery, imaging of the animals under the supervision of professor A. Saghatelyan. All authors participated in data interpretation and writing of the manuscript.*

**Chapter 3:** A. Bagramyan, "Lightweight 1-photon miniscope for imaging in freely behaving animals at subcellular resolution," *IEEE Photonics Technology Letters* **32**, 909–912 (2020).

*This publication presents the development of an optimised miniaturized imaging system with fixed focal plane. The novel mechanical (weight, size) and optical features (resolution, magnification) of the device are described. My role in this publication was to design-build-characterize the novel miniaturized device. I also tested the imaging capacity of the system, analysed the data and wrote the Manuscript.*

**Chapter 4:** A. Bagramyan, L. Tabourin, A. Rastqar, F. Bretzner, T. Galstian, "Focus tunable microscope for subcellular imaging in freely behaving animals," *submitted, Nature Methods*, 2020.

*This paper presents the integration of the liquid crystal lens device in the 2D system described earlier. The experimental utility of the final system is demonstrated by electrically adjusting the focal plane position in the brain of freely behaving animals. My role in this publication was to design-build-characterize the imaging capacity of the miniaturized device. Alongside A. Rastqar (master student in Neuroscience) and L. Tabourin (doctorate student in Physics) I performed the surgery and imaging of the animals under the supervision of Professor F. Bretzner. All authors participated in data interpretation and writing of the manuscript.*

# Introduction

## I.1 Imaging, the power of light

Optical imaging is one of the most established methods for the studying of small biological features, invisible by the naked eye. Behind this success are the different properties of the light allowing to efficiently study the structural and functional characteristics of living organisms [1; 2].

First, light is non-invasive. In contrast to classical surgical methods, it allows investigation in absence of direct physical contact with the object being imaged [3]. In biomedical applications, this is crucial, as it allows to study living specimens in their natural environment with minimal modification of their original behaviour.

Second, light is diverse. The vast spectrum of light offers multitude of wavelengths, substantially broadening the experimental repertoire and adding to the diversity of light-tissue interactions [4].

Third, light is precise. The use of optical filters, gratings, etc. allows to choose, very precisely, among the different spatial characteristics (amplitude, polarisation, etc.) of the light, adding to the specificity and accuracy of light-tissue interactions.

Finally, light is fast. Biological events, such as neuronal activity, for instance, are quite rapid [5] and therefore require the use of tools with a high sampling rate.

Until recently, the human eye was the only tool allowing to capture the light, observe and analyze objects. Thus, the application repertoire of optical imaging was defined by the limited capacity of human visual system (eye, brain) that was unable to take full advantage of light's potential [6; 7].

In the past decades, revolutionary advances in optics [8; 9] (development of various light sources, lasers, etc.), electronics [10] (powerful computers, high-speed data storing devices, etc.) and optoelectronics [11] (camera sensors (complementary metal oxide semiconductor (CMOS) or charge-coupled devices (CCD)), photo-detectors, etc.) have contributed to the rapid growth of the potential applications in the field of light microscopy [11]. The simple

pictorial visualization of the human eye has been surpassed and today, it's possible to efficiently digitize, quantify and record, for a long period, the dynamic behaviour of light and also, its interactions with the living tissue.

## I.2 Fluorescence, imaging the brain

The development of the first genetically modified green fluorescent protein (GFP) [12; 13], was another major breakthrough in the field of biomedical imaging. Neuroscience was particularly interested by this new protein that allowed the targeting of specific neuronal structures (Figure I.1c-d) within the ensemble of brain cells [14].

The operation of GFP molecules is demonstrated in the Figure I.1a. By illuminating the protein with the proper wavelength of light, it's possible to force transitions from lower, to higher energy levels [15; 16]. The return of the electron to the original orbital (desexcitation) generates light with a longer wavelength and lower energy (Figure I.1a,b). The difference between excitation and emission peaks is described by the *Stokes shift* [17] (Figure I.1b).

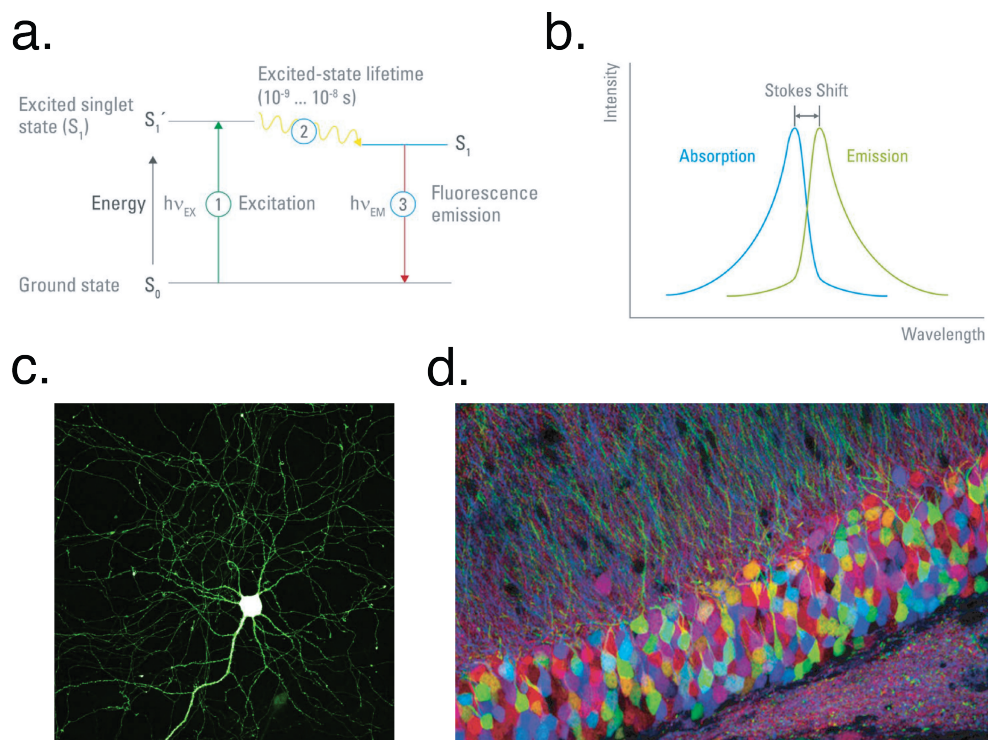


Figure I.1: **Functioning and biological application of the fluorescent proteins.** a. Schematic demonstration of electronic transition and b. corresponding absorption and emission (fluorescence) spectra [15; 16]. c. Fluorescent neuron expressing GFP. d. Color diversity of fluorescent proteins [18].

By using the correct imaging configuration (e.g., epifluorescence, Figure I.3b), it's possible to take advantage of Stokes shift to efficiently monitor neurons. To do so, GFP is inserted

within the neurons by modifying animal's genetics (transgenic mice [19]) or by viral injection [14]. Both methods will force the host brain cells to fabricate the fluorescent protein. Once assembled, the fluorescent protein will brighten the neurons in presence of the proper excitation light (Figure I.1c). The collection, filtering and focusing of the emitted light (Figure I.1a-b) will allow to visualize the target population of neurons (expressing GFP) and to contrast them from the ensemble of brain cells that are invisible in the absence of the fluorescent proteins [13].

Different variants of GFP (e.g., voltage-sensitive [20], pH-sensitive [21], calcium sensitive [22], etc.) have been developed in recent years allowing to investigate the functional characteristics of neurons by spatio-temporal imaging of their intra- and inter-cellular processes. The genetically encoded calcium indicators (GECIs) like GCaMP for instance, have the particularity to activate (by undergoing conformational changes) their fluorescence in the presence of calcium ions ( $Ca^{2+}$ ) [22; 23]. When neurons send information along an axon (to other neurons) the difference of electrical potential across their membrane changes drastically and triggers the opening of various ions channels ( $K^+$ ,  $Na^+$ ,  $Cl^-$ , etc.) [24].  $Ca^{2+}$  is one of the ions that are transported through the membrane of neurons during the activation [25]. Triggered by the presence of calcium, the fluorescence of GCaMP increases (proportionally to the amount of  $Ca^{2+}$  molecules) and allows to monitor ( $\approx 25$ -30fps) the level of activation within the ensemble of the neuronal structure (soma, dendrites, axons, spines) [26].

### I.3 *In vivo*, benchtop systems

The combination of previously mentioned progress in electronics, optics and genetics had a big impact in the fields of neuroscience and biophotonics with a rapid growth of various imaging applications and tools. The development of *in vivo* imaging devices (from latin : "*within the living*") is particularly attractive here, allowing to study the living tissues in their natural environment, in our case, the brain [27; 28].

First *in vivo* systems were based on conventional benchtop (macroscopic) epifluorescence set-ups with adapted mechanical holders to ensure the immobilization of the animal's head (Figure I.2) [29; 30; 31; 32; 33]. These systems were able to image and record the neuronal activity within the living brain at relatively high frame-rates [27]. The use of small magnification objectives [29] allowed to increase the field of view (FOV) giving access to larger imaging zones with a higher density of neurons. Another advantage of benchtop microscopes was their flexibility in terms of the imaging configuration allowing to alter between the regular wide-field [34] and more advanced, high-resolution approaches (e.g., 2-photon [30], confocal [35], etc.) . Thus, these systems were capable to image with cellular [33], and, subcellular [30] resolutions allowing to study the main body of the neurons (soma) and also the small neuronal features (dendrites, axons, process, spines, etc.).

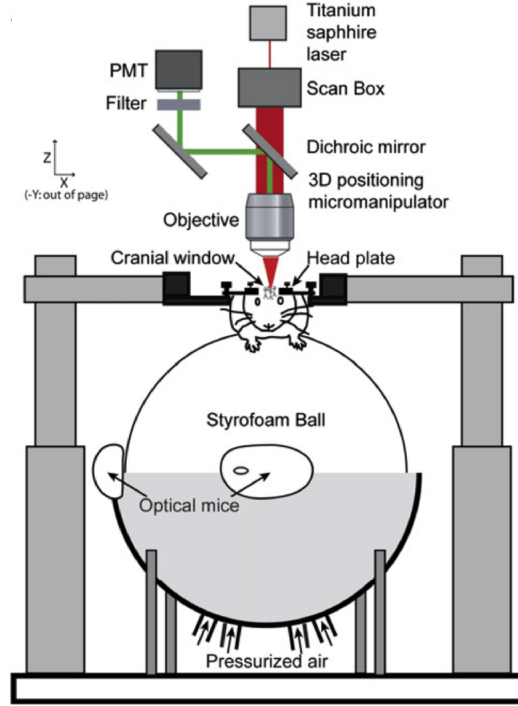


Figure I.2: **Benchtop 2-photon microscope design adapted for *in vivo* imaging** [33].

However, there were limitations from the behavioural perspective; first benchtop systems were adapted for deeply anaesthetized subjects. Even though certain investigations could be addressed here [27], the efficiency and the resemblance with real, awake animal models remained questionable [36; 37; 38]. Moreover, the study of important behaviours (e.g. running, grooming, etc.) was impossible in anesthetized subjects. To solve these issues, researches developed advanced conditioning protocols allowing to habituate animals to the head fixed situation [39]. This was an important step forward allowing to work with consciously awake animals, able of responding to the external simulations (e.g., visual [40], auditory [41], etc.). In recent years, multiple studies emerged proposing advanced variations of benchtop systems for studying more complex situation, such as virtual reality [40; 31] (figure I.2).

**Limitations.** Although promising, benchtop systems are expensive, hardly accessible, complex to build and suffer from major limitations caused by the head fixation of the animal. Even though certain biological questions are studied using this method [27], the absence of the vestibular cues (induced by the rotation of the head) is susceptible to affect the navigation of animals and also impact various decision making choices [42; 43]. The head fixation is also known to cause neck pain, stress and fatigue that affect the behavior and modify the original activation pattern of the neuronal structures [44; 45]. Finally, multiple behaviours (e.g., cognition, foraging, social interaction, mating, fighting etc.) in rodents are naturally expressed through the head movement and require investigation in the freely moving sub-



jects [46].

## I.4 *In vivo*, miniaturized systems

To solve limitations regarding the head restrained model, portable miniaturized microscopes have been developed for neuroscience applications [28; 46]. These systems are usually tiny and lightweight enough to be carried by small animals such as birds, rats and even mice. The first prototype was reported in 2011, demonstrating the ability to image multiple neurons within the brain of a freely behaving mouse [47]. Multiple adaptations of such portable devices have emerged over the last years [46; 48]. Hereafter we chose to separate them in two categories depending on their capacity to distinguish small neuronal features.

### I.4.1 Imaging with cellular resolution

The first category is composed of miniaturized microscopes with *cellular* resolution adapted for the imaging of large structures, such as the soma (neuron's body,  $\approx 15\text{-}50\ \mu\text{m}$  in diameter) [46; 48]. To access more neurons and to have a better representation of the neuronal network, small magnifications ( $\times 4\text{-}\times 10$ ) and large field of views are preferred here. These systems are particularly attractive for the characterization of the functional role of a specific population of cells within a large region of interest (ROI) [28].

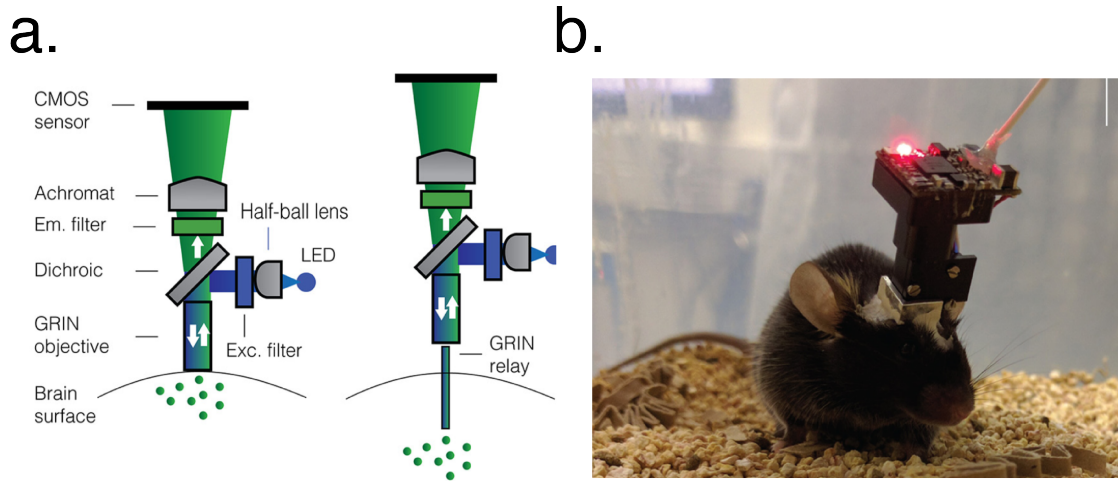


Figure I.3: **Miniaturized 1-photon microscope design.** **a.** Schematic representation of a system adapted for the imaging of brain surface (left). Configuration allowing to image deep regions of the brain (right). **b.** Miniscope system developed at the University of California, Los Angeles (UCLA) [49; 46].

**Short technical description.** This category is mainly composed of wide-field imaging devices [50; 49; 51; 52] with epifluorescence imaging configuration (Figure I.3a). The excitation light sources are standard LEDs [49] (emitting in visible spectrum range) and are placed directly on the miniaturized system or brought to the optical pathway by means of large core

( $\geq 200\mu\text{m}$ ) multi-mode optical fibers [53]. The presence of chromatic filters and dichroic mirror ensures the proper synchronisation with the excitation and emission wavelengths of the neurons marked with GFP (or other fluorescent protein, e.g., GCaMP). Achromatic lenses are usually used to guide and focus the light on the pixelized sensors such as a CMOS or a CCD. As demonstrated in Figure I.3a, the use of GRIN optical probes can enable access to deep regions of the brain (1-6 mm from the surface) [54].

**Limitations.** Although promising, important limitations within this category of imaging devices significantly reduce their efficiency and also limit their application repertory.

First, the lack of depth scanning mechanisms limits these systems to two dimensional (2D) imaging. This drastically reduces the efficiency of surgical procedures and also affects the quality of calcium recordings [55]. Trying to address this issue, some tunable miniaturized systems have been developed by private companies [56; 57]. The system from Doric lens [57], for instance, reports a  $\approx 300\mu\text{m}$  focal shift capability. However, this depth scanning system is heavy and once mounted can weight up to  $\approx 4.5 \pm 0.5\text{ g}$  ( $\approx 3.0\text{ g}$  the miniscope,  $\approx 0.5\text{ g}$  the implant,  $\approx 1\text{ g}$  the screw(s) and dental cement). Latter "load" is significantly higher compared to the conventionally established  $\approx 10\%$  of the animal's weight ( $\approx 2.5\text{ g}$ ) [28; 46]. Thus, the use of such device with small animals, such as mice, is doubtful. Another depth scanning 1-photon system from Inscopix [56] seems to be significantly lighter, but to the best of our knowledge, similar to Doric's system, its depth scanning ability has never been reported *in vivo*. Consequently, the practical effectiveness of existing depth scanning devices isn't obvious.

Second, the development of compact 1-photon devices is challenging in terms of optical and mechanical engineering. Unfortunately, available cellular imaging systems remain heavy, bulky and difficult to carry for small animals [27]. This has a negative impact from multiple perspectives. For instance, it limits the experimental repertory to adult subjects only (usually bigger and stronger) making almost impossible the work with younger (smaller) animals that are particularly interesting for the study of brain development paradigms (e.g., neurogenesis : cellular division, migration of stem cells, integration within the existing network, etc.) [58]. In addition, the exaggerated weight and size (Figure I.3b) of these imaging devices can cause stress, affect the head movement of the animal, modify the natural navigation and decision making choices [45].

Finally, the cellular resolution of available 1-photon systems isn't sufficient to image and record from finer structures of neuronal circuitry such as axons, dendrites, spines [46]. These subcellular compartments are wherein all neuronal processing and the better understanding of their function appears to be the next step toward a better understanding of the brain [59].

### I.4.2 Imaging with subcellular resolution

The second category is composed of miniaturized microscopes with *subcellular* resolution adapted for the imaging of finer neuronal structures [60; 61; 62; 63; 64; 65]. To increase the quality of calcium recording from small neuronal features, high magnification and high pixels/object ratios are required here. These systems are particularly attractive for the characterization of the functioning role of dendrites, processes (e.g., filopodium), axons, spines, etc. within various brain regions of freely behaving animals [59].

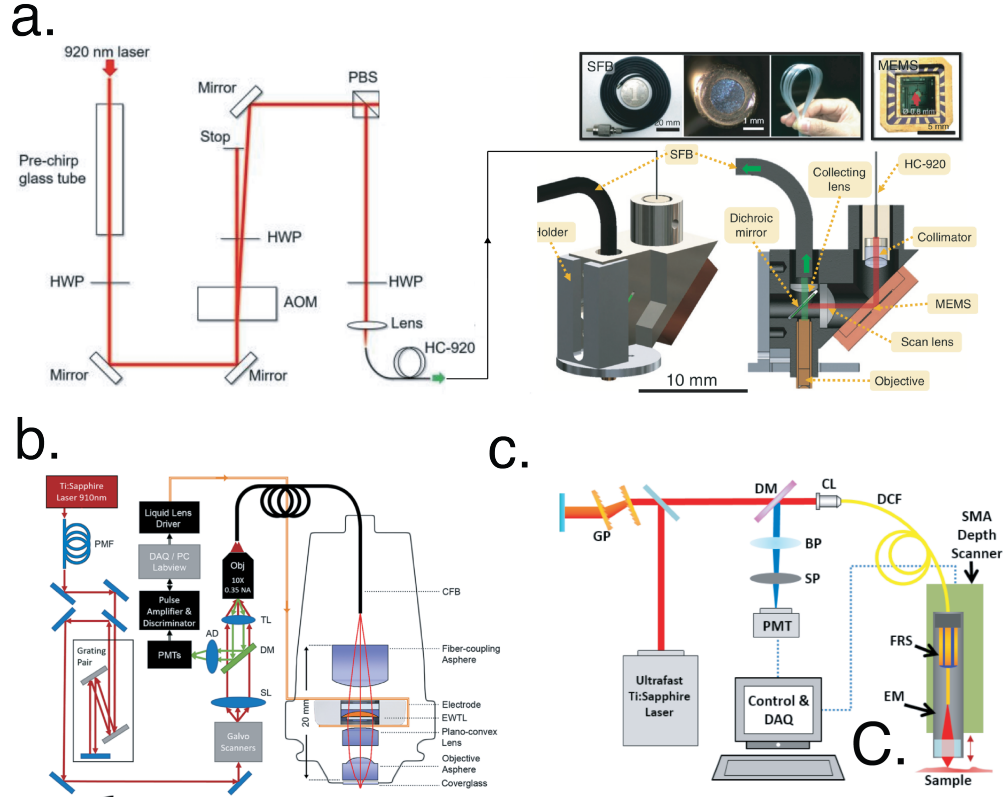


Figure I.4: **Schematic representation of miniaturized multi-photon microscope designs.** **a.** System with internal MEMS placed directly on the miniaturized device. [62]. **b.** System with an external scanning approach. Electrowetting lens (EWL) is placed directly on the miniaturized device. [66]. **c.** Scanning system based on the mechanical displacement (rotation) of the optical fiber [67].

**Short technical description.** In terms of optical configuration, this category is more diversified. It's composed of miniaturized 2-photon [66; 62], confocal [65] and fiber-scanning devices [67; 60; 61] (Figure I.4) with different optical designs and components. The common difference compared to the previous category is the choice of the light source and of the optical detector. In this kind of approach, coherent sources, such as lasers (continue or pulsed) are considered. The use of near-infrared excitation wavelengths (Figure I.4a) enables longer penetration capacity within the living tissues [68]. The optical sensors are standard photo-detectors with a single photosensitive area. To form an image in the absence of pix-

elated light detector, different scanning strategies are considered. Micro-electromechanical systems (MEMS) are usually used and commonly placed outside the miniaturized system due to their noticeable size and weight (figure I.4b) [66]. Recent studies have also reported MEMS that were placed directly on the miniaturized device (Figure I.4a) avoiding the use of multimode fiber bundles [62]. Finally, some scanning technics consider the mechanical displacement of the imaging optical fiber by means of mechanical actuators [67] (figure I.4c).

**Limitations.** Also within this category, there are important limitations that reduce the efficiency and the experimental capability of subcellular imaging devices.

First, the depth scanning isn't obvious here. Even though the use of electrowetting lenses (EWL) was recently reported [66; 65], major drawbacks disadvantage this approach. For instance, currently available EWLs [69] have low optical power, large clear aperture, high operational voltages, big size and weight, etc. A more detailed description of these limitations is presented in the upcoming section.

Second, the available miniaturized subcellular devices are complex to build (mechanically and optically), expensive (pulsed light sources, MEMS, etc.) and hardly accessible. The use of custom components (e.g., dispersion corrected fibers [62], multicore fiber bundles [66; 65], etc.) usually restrains the reported techniques to the original research groups which detain the manufacturing know-how.

Third, devices within this category suffer from excessive weight and size that has negative impact on the animal's behaviour (see the previous section).

Fourth, the optical design of these systems requires the use of large diameter optical probes (more than 1.5 mm) that are invasive and harmful to the animal. The surgical procedure usually requires brain aspiration that can have major undesirable impact on the animal's health and also impact the functioning of the brain [70].

Finally, the use of complex scanning methods and the presence of coherent light sources disables the compatibility with future wireless approaches [51; 46].

## I.5 Summary of existing limitations

There are different drawbacks among the existing portable miniaturized devices. Three of them are common to both categories (cellular and subcellular) and thus are fundamental issues within this application.

**The first major** issue is the lack of an efficient depth scanning element enabling the electrical modulation of the focal distance. This challenge is difficult to address due to the severe physical, electrical and optical criterias : small size, lightweight, low power consumption, low operational voltages and high optical power (in the order of hundreds of dioptries).

To the best of our knowledge, no device reported in the literature is able to satisfy the ensemble of these requirements. The closest candidate is the commercially available EWL from Varioptics (now Corning [69]), but as discussed previously, this alternative fails in different aspects. First, EWLs have low optical powers that range from -5 to 15 dioptres. As will be described in the chapter 1, the direct coupling with GRIN probes (Figure I.3a, right) requires much higher optical powers, in the order of hundreds of diopters. In the absence of GRIN lenses, deep regions (e.g., hippocampus, sub-ventricular zone, etc. [71]) remain inaccessible and EWL systems can only be used to image the surface of the brain. Second, the size of the clear aperture (CA) of EWLs is another limitation. The smallest CA available (1.6 mm) is 3 times larger compared to GRIN's diameter (0.5 mm). This difference drastically reduces the efficiency of the direct optical coupling between the 2 elements (GRIN and EWL). Third, EWLs are quite demanding in terms of the operational voltage (can reach up to 60 Volt). This is a major issue for future wireless approaches that require low power consumption [51]. Finally, the mechanical characteristics (weight and size) of EWLs are borderline acceptable, furthermore complicating the use of this element within the miniaturized devices.

**The second major** limitation within the existing miniaturized cellular and subcellular devices is their weight and size. As mentioned previously, the available tools are big and bulky and usually hardly compatible with small animals such as young or elder mice. Even-though these systems are often used in such subjects, their impact on the animal's condition (health) and behaviour is a problem that must be addressed in the future.

**The third major** limitation is that the imaging of fine neuronal structures has been so far exclusively reserved to the subcellular systems [60; 61; 62; 63; 64; 65]. From the practical perspective this is problematic because of the complexity, price and inaccessibility of the devices within this category. Therefore, the ability to image fine structures with 1-photon imaging system (simple, affordably and accessible) would be a big asset allowing an easier access and imaging of fine neuronal structures within freely behaving animals.

To solve these limitations, we used liquid crystal technology that is well established within the miniaturized application (e.g., cellphone cameras, medical endoscopes, etc.) [72; 73; 74; 75; 76]. To solve the first major limitation within the existing devices, we have developed a custom liquid crystal (LC) lens [77] adapted to the miniaturized microscopes applications [28]. To solve remaining limitations, we have developed a lightweight miniaturized 1-photon system that integrates the LC lens and enables depth imaging of subcellular structures [53].

## I.6 Liquid crystals

### I.6.1 Historical

The discovery of an intermediate state (other than the crystalline solid or the isotropic liquid) emerged in the 19th century, at the time when only three states of matter (solid, liquid, gas) were known. In 1888, while heating cholesterol benzoate, the Austrian botanist Reinitzer was surprised to observe two melting points [78]. Looking for an explanation to this strange phenomena, he contacted the physicists Otto Lehmann writing him the following letter :

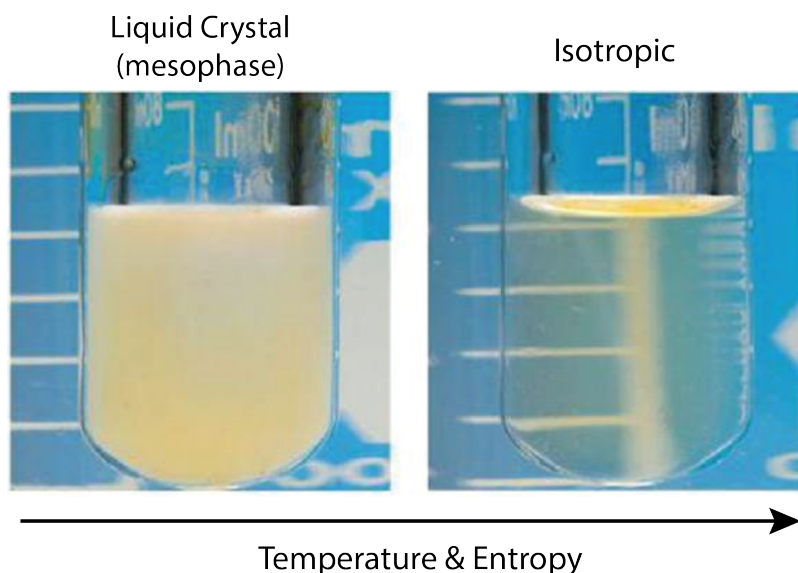


Figure I.5: **Different phases of matter.** At the 2nd melting point, the cloudy liquid (liquid crystals) become isotropic, almost transparent [79].

*« The two substances (cholesterol esters) are the site of such beautiful and strange phenomena that they should, I hope, also interest you in the highest degree. [...] The substance has two melting points, if we can put it that way. Around 145.5°C it melts and forms a cloudy but completely fluid liquid, which around 178.5°C suddenly becomes completely transparent. By cooling it, we see the blue and purple colors appear which fade quickly by having the opaque substance (like milk) but still fluid. Continuing the cooling, the blue and purple colorings reappear and, immediately after, the substance solidifies, forming a white crystalline mass. [...] The cloudiness that appears when heating is due not to the crystals but to the liquid that forms the oily streaks .. »*

Lehmann decided to study this strange phenomenon and using his specialized microscope, he was able to study the LCs under the polarized light at variable temperatures. A year later (1889), Lehmann published an article entitled "Über Fließende Krystalle" which turns out to be the first publication introducing the concept of "liquid crystal" [80]. The publication sparked huge interest at the time, but the low practical potential has quickly drawn away



from the attention from LCs.

In 1962 (73 years later), liquid crystal materials regain a new, this time, commercial interest from RCA Laboratories who focused on the development of flat panel electronic displays [81]. Within 4 years, the company was able to make a mixture of nematic liquid crystals that was stable at room temperature [82]. This was a fundamental advancement that allowed to fabricate the first practical display devices [83]. Since that moment, different LCs (e.g., N-4-Methoxybenzylidene-4-butylaniline, 4-Cyano-4'-pentylbiphenyl, etc.) have been developed, continuing to improve the practical utility and popularity of LCs within commercial applications [84]. Thus, from 1980 to 1990, the liquid crystal technology became widely spread and could be found in displays, watches, large size television screens (LCDs), etc. [76; 85].

### I.6.2 Types of LCs

Liquid crystals can be divided into two groups: thermotropic and lyotropic. The mesophase state (between solids and liquids) of lyotropic LCs [86] occurs upon the addition of a solvent (typically water), whilst the thermotropic LCs [87] are mainly dependent on the temperature. Within our application, we will focus on thermotropic LCs that can be sub-classified into calamitic (C-type) and discotic liquid (D-type) crystals depending on the shape of the molecules [88]. C-type LCs are particularly interesting due to the diversity of their self-assembled configurations that can be either nematic, smectic and cholesteric phases. Each of these phases has different properties such as the anisotropy, ferroelectricity, chirality, etc. [89].

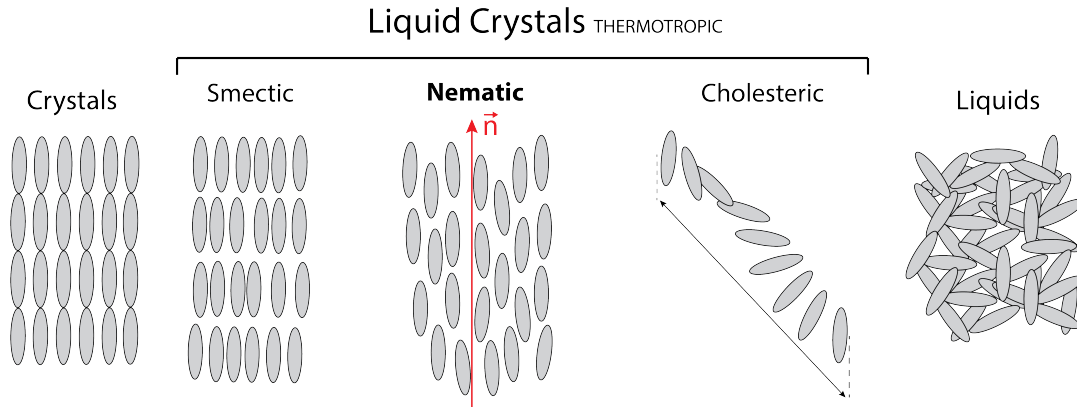


Figure I.6: Different states of matter. In the middle, different types of thermotropic LCs : smectic, nematic, cholesteric.

### I.6.3 Nematic LCs

Nematic LCs are the most simple, the most studied and the most used in different display and imaging applications [85]. As demonstrated in the Figure I.6, the distribution of the

center of mass of nematic LC molecules is random, but the direction of these molecules is common. The average direction of these molecules can be represented by the unitary vector  $\vec{n}$  (Figure I.6), called the **director** [89]. The uniform orientation of molecules within the volume results in the formation of liquid "monocrystals".

However, if external forces are applied to the volume of molecules then, the orientation of the director may vary [89]. This can occur in different situations. For instance, during the manufacturing of the LCs cells, the presence of small impurities can induce variable forces within the cell that will produce undesired domains separated by abrupt changes of director orientations, called disclinations [90]. However, other type of forces (within the volume) can be induced in a desired way, for instance, by applying an external electrical field. This is the case in multiple applications that require orientation gradient of molecules, that is particularly attractive due to the anisotropic properties of LCs [72; 91; 92].

#### I.6.4 Optical anisotropy of LCs

LCs have different properties (e.g., refractive index, conductivity, absorbance, etc.) for different directions of light polarization (anisotropic materials). In our case, we are interested in the optical anisotropy of nematic LCs (NLCs, Figure I.6) [89]. These materials are uni-axial (with positive and negative anisotropy) and the molecule of NLCs with positive anisotropy is often represented by the elongated elliptic model (I.7) :

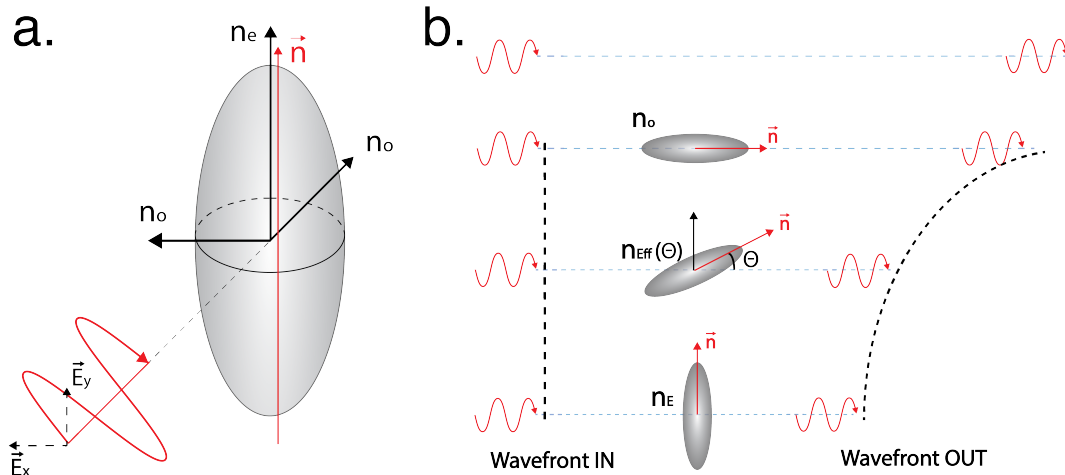


Figure I.7: **Elongated elliptic model of uni-axe LCs.** **a.** Uni-axial calamitic (C-type) LCs. **b.** Temporal delay in function of the orientation of molecules.

As demonstrated in the Figure I.7a, the two perpendicular components ( $\vec{E}_x, \vec{E}_y$ ) of the polarized light beam (entering the NLCs layer) will see 2 different refractive indexes. The component ( $\vec{E}_x$ ) that is perpendicular to the director ( $\vec{n}$ ), will perceive an ordinary refractive index ( $n_{\perp}$ ) while the parallel component ( $\vec{E}_y$ ) will see the extraordinary refractive index component ( $n_{\parallel}$ ) [89]. The speed of light ("v" in matter) being dependent on the refractive



index  $n$  ( $v = c/n$ , "c" is the speed of light in vacuum), a relative phase shift  $\Delta\phi$  will occur between the components  $\vec{E}_x$  and  $\vec{E}_y$ . Consequently, the output polarisation will change to circular, elliptic or linear depending on the value of  $\Delta\phi$  Eq.(1) :

$$\Delta\phi = \frac{2\pi d \Delta n_o}{\lambda} \quad (1)$$

where  $d$  is the thickness of NLC ;  $\lambda$  is the wavelength of the light beam;  $\Delta n_o$  is the difference between the extraordinary and ordinary refractive indexes.

The temporal delay induced by the NLCs can also be used to modify the wavefront of light [93]. For our application, particularly interesting is the orientation of NLCs, demonstrated in the Figure I.7b that can change the shape of incoming wave-front. This occurs due to the variation of the angle  $\theta$  between the wave-vector of light and the director of NLC. This reorientation gradient of NLC molecules changes of the refractive index Eq.(2) [92] :

$$n_e(\theta) = \frac{n_{\perp} \times n_{\parallel}}{\sqrt{n_{\parallel}^2 \times \cos(\theta)^2 + n_{\perp}^2 \times \sin(\theta)^2}} \quad (2)$$

where  $n_{\parallel}$  and  $n_{\perp}$  are the refractive indexes that are parallel and perpendicular to the director  $\vec{n}$ ;  $\theta$  is the angle between the director  $\vec{n}$  and the axis of propagation of light.

As demonstrated in Figures I.8 and I.9, the application of a non-uniform electrical field can generate the desired (e.g., spherical or parabolic, Figure I.10) wave-front (see next section). Thus, the dynamic control of the orientation of NLC molecules is a powerful tool enabling control over the convergence of the light [92; 93].

### I.6.5 Electrical alignment of NLCs

As mentioned previously, the reorientation of NLC molecules can be used to shape the wave-front of the light and, for obvious reasons, this modulation must be electrical.

Apart from the anisotropic optical properties, the NLC molecules have another interesting feature : anisotropic polarisability at lower frequencies (e.g., 1 kHz) [92]. In the presence of an external electric field, the movement and the displacement of electrons (usually stronger in the longitudinal direction of molecules) results in the induction of electric dipoles. The so called "dielectric torque" (Eq.(3)) will now tend to align the molecules in the direction parallel to the field (Figure I.8) [94] :

$$\Gamma = \vec{D} \times \vec{E} \quad (3)$$

where  $\Gamma$  is the dielectric torque;  $\vec{D}$  is the electrical induction;  $\vec{E}$  is the electric field.

If the amplitude of the electric field is higher than the intrinsic elastic forces of the NLCs (that are responsible for the alignment of molecules), re-orientation of molecules will occur [92]. The minimum voltage necessary to initiate rotation of molecules is defined as the threshold voltage [72] and its value depends on the type of NLCs. Thus, the anisotropic mobility (polarisability) of electrons allows to use an external electric field to reorient the NLC molecules and to electrically modulate the extraordinary refractive index.

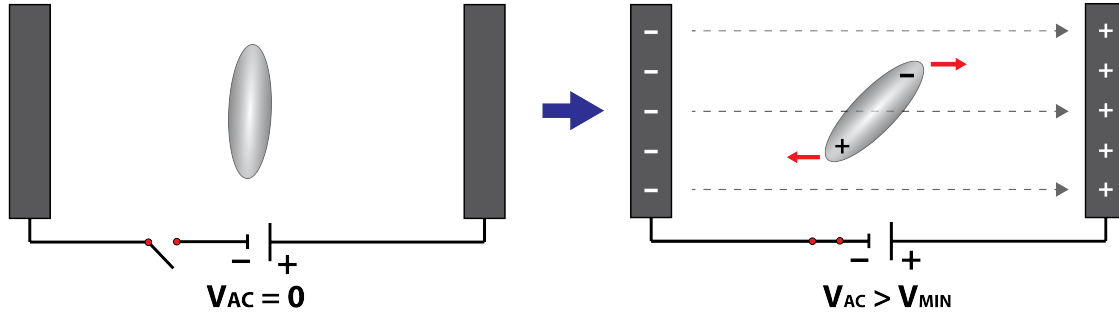


Figure I.8: On the left : LC molecules in absence of external electrical field. On the right : electric induction, formation of LC dipoles and alignment of LC molecules by the electrical field.

To generate a lens, NLC molecules must be reoriented in a quasi-parabolic way to obtain the desired refractive index profile of the GRIN lenses, demonstrated in the Figure I.10 [94]. To achieve this, a custom NLC cell must be assembled with specific parameters (e.g., shape of the electrodes, resistivity of the cell, etc.), adapted for our application [92].

### I.6.6 Tunable LC lens (TLCL)

The LC cells are usually composed of two face-to-face glass substrates with different thin layers (Figure I.9a) [92]. Each of these layers has an important role that will be described hereafter.

Distance between the substrates can be controlled by using microscopic spacers. The presence of electrodes on the internal sides (toward the NLC molecules) of substrates allows to generate an electric field that reorients molecules. The shape of the electrode can differ depending on the application allowing to generate the desired distribution of the electric field within the volume of NLCs [72; 92].

#### Electrode shape and distribution of the electric field

The combination of uniformly distributed electrode on substrate 1 (bottom) and the circular ring-shaped electrode on substrate 2 (top), allows to generate a **spherical** distribution of the electric field (Figure I.9d) [95; 96; 97]. The corresponding spherical reorientation of NLC molecules will occur and will allow to generate a lens like index distribution of the refractive

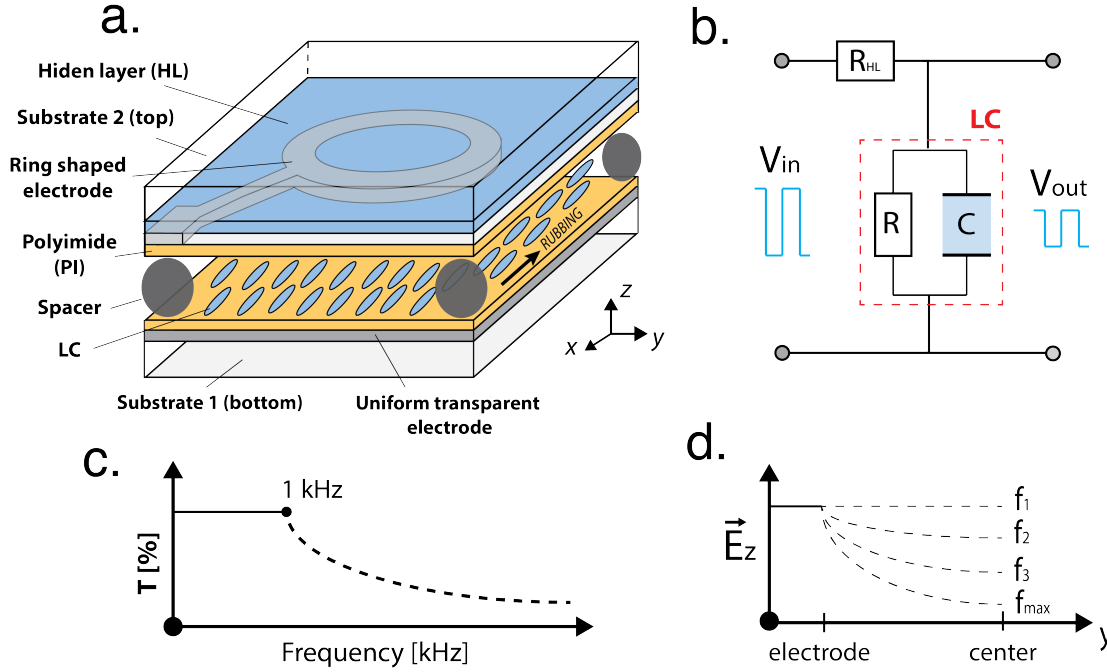


Figure I.9: **Tunable LC cell.** **a.** Schematics of the design. **b.** Electrical circuit (of the TLCL) that acts as a low pass filter. **c.** Frequency dependence of the circuit in **b.** **d.** Distribution of the electrical field within the LC cell.

index (Figure I.10). The optical power (OP) of the generated lens (Eq.(4)) will be inversely proportional to the square of the radius of the electrode ring [92].

$$OP = \frac{2L\Delta n}{r^2} \quad (4)$$

where  $OP$  is the optical power;  $L$  is the thickness of the NLC layer;  $\Delta n$  is the difference between the refractive indexes values in the center and the periphery of the lens.

Another important feature within the design of the NLC cell is the capacity to control the distribution of the electrical field by modulating the input voltage frequency. To better understand the concept, the NLC cell is usually modeled as a distributed electrical RC circuit (Figure I.9b) with a parallelly displaced capacitor and resistance that are in series with the resistance  $R_{hl}$  (described in the upcoming section) [98]. The following circuit design is known to be an electrical low pass filter that discriminates the high frequencies (Figure I.9c). By carefully selecting the correct resistor( $R_{hl}$ )-capacitor( $C$ ) combination, it's possible to precisely control the frequency dependence of attenuation. Within our application, the  $\approx 1$  kHz frequency is usually used as the cut-off frequency (I.9c) with the amplitude of higher frequencies being (gradually) attenuated [92]. This frequency dependent transmission decrease can be used to create a gradient of spatial distribution of the electrical field that will change the orientation of NLC molecules (Figure I.10).

As mentioned previously, to achieve a good spherical distribution of the electric field within the cell, it's important to define the correct combination of capacitor (C) and resistor ( $R_{hl}$ ) (Figure I.9) [98]. The value of the capacitor (C) is established by the type of the NLCs (e.g., E7, ML6080, etc.) while the resistivity ( $R_{hl}$ ) can be controlled by carefully adjusting the thickness and concentration of different partially oxidized metallic layers deposited on the substrate (Figure I.9a) [99].

### Resistivity, hidden layer (HL)

The resistivity  $R_{hl}$  of the NLC cell is a key parameter allowing to optimise the distribution of the electrical field ( $\vec{E}_z$ ) with the cell [99]. If  $R_{hl}$  is too low, the field  $\vec{E}_z$  will be too strong and will never reach the zero amplitude at the center (Figure I.10a, #1) of the lens. In the opposite case, if the  $R_{hl}$  is too high, the field will only be present at the edges of electrodes and will not propagate towards the center of the cell (Figure I.10a, #2) [92]. Therefore, the value of the resistivity must be chosen carefully to obtain the optimal distribution presented on the Figure I.10a, #3.

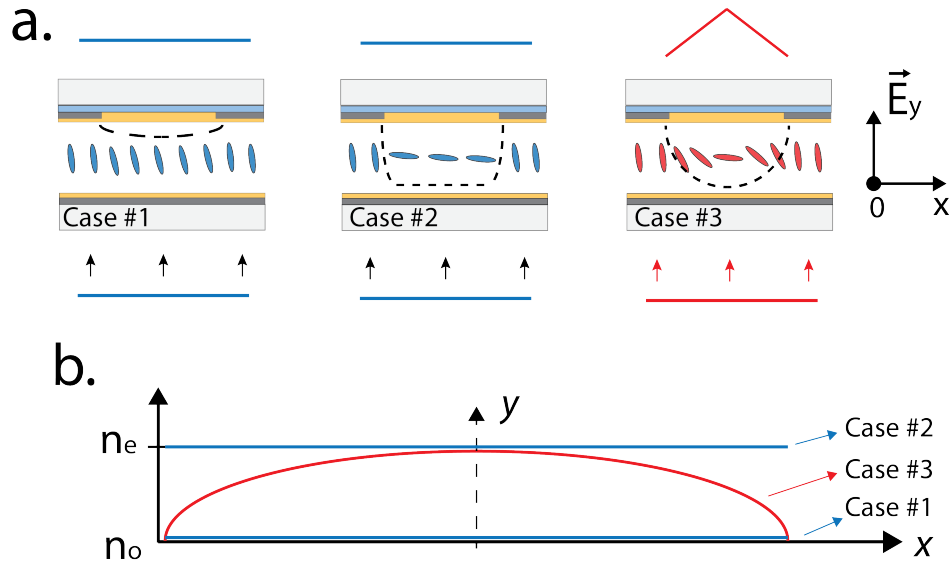


Figure I.10: **Resistivity and the distribution of the electrical field.** **a.** TLCLs with different resistivities. Case 1: too low; Case 2: too high; Case 3: optimal; **b.** Distribution of the refractive index within the LC cells in a.

Even-though several studies have been reported in the literature [99; 100; 101], computational simulations remain complex and to the best of our knowledge, no theoretical model can predict the exact value of the resistivity. Thus, this parameter is often determined empirically (by observation or experience rather than theory).

### Rubbing

To create a stable and reversible reorientation of molecules within the NLC cell, it's useful

to have a rather strong anchoring on the surface of cell substrates. As a general rule, planar anchoring ( $\vec{n}$  parallel to the surface) is obtained by rubbing a thin layer of polyimide (figure I.9a, figure I.11) with NLCs tending to align in the direction of rubbing [102; 103]. Having an anchor point helps to control the alignment within the volume and also to stabilize the molecules at their equilibrium position (in the absence of the field) [92].

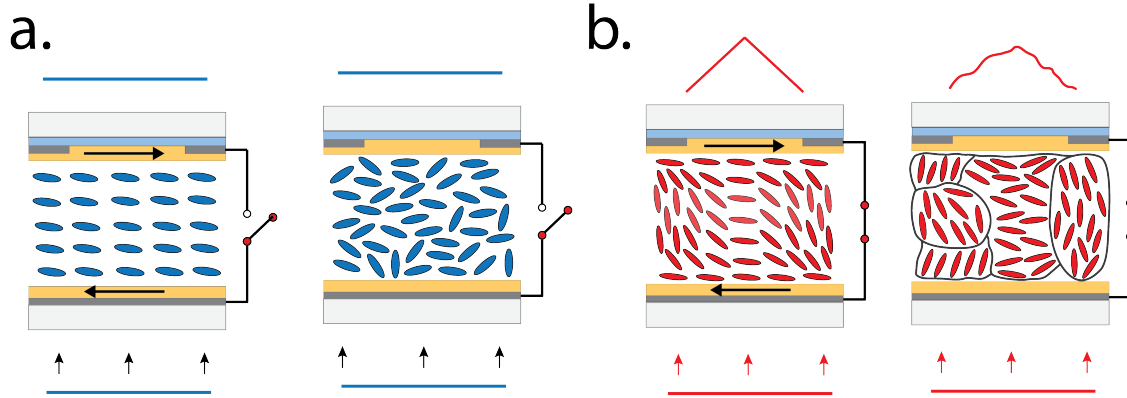


Figure I.11: **Rubbing and the alignment LC molecules.** **a.** No voltage is applied. Rubbing tends to align molecules (director being parallel to the direction of the rubbing). In the absence of rubbing, the orientation of molecules is random (right). **b.** AC square voltage is applied to the cell. Rubbing helps to generate a smooth reorientation gradient of molecules (left). In the absence of rubbing, different LC domains are formed (right). The "disclination" (separations between LC domains) are indicated with black lines.

In the absence of the electric field, anchoring creates a restoring torque that forces the molecules to return to their initial orientation (Figure I.11a). This initial alignment (often parallel to the substrate) enables gradual and uniform re-alignment in the presence of the external electric field [102; 103]. In the opposite scenario (no rubbing) molecules will align arbitrarily (in the energetically favorable direction) on the surface of the substrate and also within the volume (Figure I.11). When an electrical field will be applied, the forced re-alignment of molecules (from random initial positions) can create separate domains, called disclinations (Figure I.11b) [90]. Latter is known to increase optical aberrations and scatter (Figure I.11b) that degrades the focusing capability of the NLC lens.

## I.6.7 Alternative technologies

The optimisation of the NLC cell (e.g., diameter, resistivity, etc.) allowed us to build a custom tunable LC lens (TLCL) adapted for miniaturized microscope application in a freely behaving animals [73; 77]. The detailed description of the parameters can be found in chapters 1, 2, 3 and 4.

Compared to our TLCL (Figure I.12), the conventional mechanical systems are bulky, costly and fragile [92]. The voice coil motors are widely used in mobile devices, but they are com-

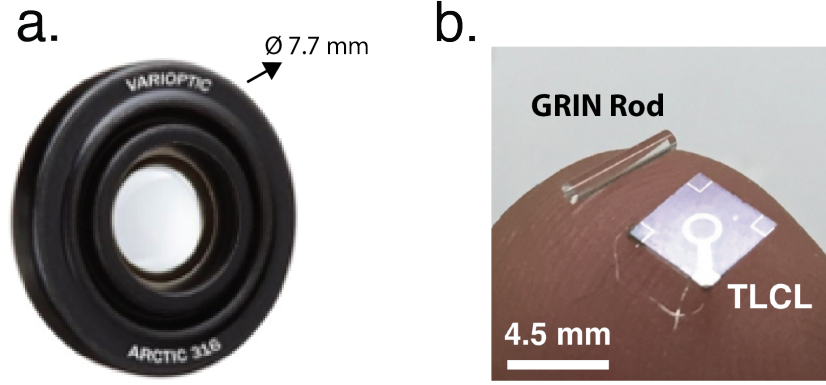


Figure I.12: **Miniaturised depth scanning devices.** a. EWL lens from CORNING [69]. b. Tunable liquid crystal lens developed at Laval University.

posed of more than 100 pieces that must be manually assembled. Their cost (in high volume) is significantly higher (by an order of magnitude). They also have ringing, hysteresis that complicates the autofocus search and they are driven by current and their power consumption is about 100 mW [92].

Relatively small liquid lenses can also be fabricated using the electrowetting approach [104]. The comparison between the TLCL and its closest commercial EWL alternative from CORNING [69] is presented in Table I.1 :

	EWL	TLCL
<b>Optical power (D)</b>	-5 to 15	160
<b>Clear aperture (mm)</b>	1.6	0.5
<b>Weight (g)</b>	1	0.1
<b>Dimensions (mm)</b>	7.7 x 7.7 x 2	5.5 x 5.5 x 0.8
<b>Voltage (V)</b>	60	3 to 5
<b>Delta shift (<math>\mu\text{m}</math>)</b>	10	100

Table I.1: Comparison between the TLCL and the EWL.

The optical power of the TLCL is much higher compared to the EWL. Thus, our lens can reach up to 100  $\mu\text{m}$  focal shift, that is  $\approx \times 10$  times higher compared to EWL. While offering high OP (and focal shift), the TLCL has lower operational voltages compared to EWL. The latter requires up to 60 Volts to reach the maximal optical power value of 15 dpt. The high

operation voltage complicates the transition toward the wireless approach that require modest electrical parameters. The TLCL requires a standard AC source with 3-5 Volts output and the minimal current consumption results in very low power consumption (few microwatts). Thus, our TLCL is better adapted for both alternatives (wired and wireless) compared to the EWL. Finally, the physical performance of the TLCL is also better with a notable 10 times difference in weight. The dimensions of the TLCL are smaller compared to EWL (Figure I.12 and Table I.1) allowing an easier integration within miniaturized imaging system [28; 46] (e.g., U.Laval, UCLA, etc.).

The comparison between the developed custom tunable liquid crystal lens and its closest alternative [69] clearly demonstrates the multiple advantages and the better performance of our device. Thus, we believe that the developed electrical tunable device will allow to solve existing limitations and enable efficient depth scanning within the miniaturized devices adapted for neuroimaging in freely behaving animals.

#### **Short description of the upcoming chapters :**

The first chapter of the thesis will present the development of the TLCL, the optimization and the correction of optical aberrations (e.g., coma and polarization mismatch).

The second chapter will present the development of an optical probe that combines a TLCL and a GRIN lens. The electrical modulation of the working distance of the probe will be demonstrated theoretically and experimentally. The incorporation of the tunable probe within a homemade macroscopic epifluorescence system will allow to image different depth positions in the brain of an anesthetized mouse.

To enable the imaging in freely moving animals, the third chapter will present the development of a miniaturized 1-photon microscope. The new optical (high resolution, high magnification, low aberrations, etc.) and mechanical (size, weight, etc.) features of the device will be described. The imaging capacity of the developed device will be demonstrated by imaging fine neuronal structures in a fixed brain tissue preparation.

The fourth chapter will present the integration of the TLCL within the miniaturized 1-photon microscope. The final miniaturized device will be described and characterized (depth modulation capacity, resolution, magnification, etc.). The biological functionality will be demonstrated by motionless electrical depth imaging ( $\approx 100 \mu\text{m}$ ) of different neuronal structures in the brain of freely moving animals.

# Chapter 1

## Dynamic control of polarisation mismatch and coma aberrations in rod GRIN assemblies

**Arutyun Bagramyan<sup>1</sup> and Tigran Galstian<sup>1,2\*</sup>.**

<sup>1</sup>*Center for Optics, Photonics and Laser, Department of Physics, Engineering Physics and Optics, Université Laval. 2375 Rue de la Terrasse, Québec (Qc), G1V 0A6, Canada*

<sup>2</sup>*TLCL Optical Research Inc. and Lensvector inc. 2375 Rue de la Terrasse, Québec (Qc), G1V 0A6, Canada*

Published in Optics Express Vol. 27, Issue 10, pp. 14144-14151 (2019)

### 1.1 Résumé

Nous décrivons la combinaison de lentilles à cristaux liquides (TLCL) électriquement modulables avec des lentilles à focale fixe (GRIN) pour des applications endoscopiques. La fabrication et le contrôle ont été optimisés pour diminuer les aberrations de l'ensemble du système. Une attention particulière a été attribuée aux aberrations de coma et de polarisation. L'aberration de coma a été réduite en empilant deux TLCL avec des angles de pré-inclinaison "opposés" (toutes les molécules sont dans le même plan), puis deux doublets de ce type ont été utilisés avec des molécules orientées en croisé (dans des plans perpendiculaires) pour réduire la dépendance à la polarisation. La lentille obtenue (GRIN adaptative) permet un balayage focal supérieur à 80  $\mu\text{m}$  (avec des aberrations RMS particulièrement faibles  $\leq 0,16 \mu\text{m}$ ), permettant l'observation en haute résolution de neurones à différentes profondeurs.



## 1.2 Abstract

We describe the use of stacked electrically tunable liquid crystal lenses (TLCLs) along with rod gradient index (GRIN) fixed focus lenses for endoscopic applications. Architectural and driving conditions are found for the optimization of total aberrations of the assembly. Particular attention is devoted to the coma and polarization aberrations. The coma aberration is reduced by stacking two TLCLs with "opposed" pretilt angles (all molecules are in the same plane) and then two such doublets are used with cross oriented molecules (in perpendicular planes) to reduce the polarization dependence. Obtained adaptive rod-GRIN lens enables a focus scan over 80  $\mu\text{m}$  (with exceptionally low RMS aberrations  $\leq 0.16 \mu\text{m}$ ) making possible the high quality observation of neurons at various depths.

## 1.3 Introduction

Electrically tunable liquid crystal (LC) lenses (TLCLs) [105; 91; 93] have been considered for various applications, including aberration control [106; 107; 108], imaging [109] and vision [110; 111; 112; 113; 77; 114; 40]. Thanks to their high sensitivity to electric fields [115; 94], those devices can operate at very low current and voltage values (requiring  $\mu\text{W}$  electrical power consumption) being thus "user friendly" for mobile applications. Namely, one of the growing needs in TLCLs is the focus tuning in miniature endoscopic probes [116; 117; 118] designed to study brain activities in freely behaving small animals (typically mice) [73; 119]. This application imposes very specific additional requirements on the TLCL. First of all, the majority of TLCLs are using nematic LC (NLC) materials, which are inherently polarization sensitive and can focus only one linear (extraordinary) polarization of light in the transmission geometry (we call them "half-lenses"). Neural fluorescence images being recorded in non-polarized light, a combination of at least two TLCLs is needed (with ground state optical axis rotated at  $90^\circ$  with respect to each other) to handle two orthogonal polarizations of light [109; 92]. Thus the mismatch of optical power (OP) values between those TLCLs and the corresponding mismatch of focal points (at the origin of "polarization aberrations") must be reduced to avoid the degradation of images.

In addition, the typical clear aperture (CA) of the optical system in general (and of the TLCL in particular) must be reduced (sometimes down to 0.5mm) to minimize the damage to the brain tissue. In this case, coma aberration become very important [108; 120].

Finally, to reach deep zones of the brain, rather long (several mm long) gradient index (GRIN) rod lenses must be used with huge (fixed) OP values, often at the order of 2000 Diopters (D). This last requirement imposes two additional constraints: increased aberrations of the system because of the low quality of commercially available GRIN lenses and the need to have very high OP variation range (provided by the TLCL) to insure a noticeable shift of the image plane (see hereafter).

One possible solution for the coma problem of the Rod-GRIN/TLCL assembly was already described in [120]. The current work aims addressing differently this problem as well as the polarization aberration problems in above-mentioned assemblies (the GRIN aberrations alone were partially analyzed in [108]). Thus, we shall start by briefly reminding the coma aberration problem and by describing an alternative approach to reduce it. We shall then describe our experimental results in the framework of an imaging system with multiple GRIN/TLCL assembly and will analyze the corresponding polarization aberrations' problem. We shall present both numerical simulations and experimental observations. We shall then discuss the obtained results and conclude.

## 1.4 Coma aberration

For this application we have used the well-known "modal-control" lens design [95; 97]. The basic unit of this TLCL is a single layer of NLC [115] that is sandwiched between two substrates of thickness = 0.1 mm. The optical birefringence of the NLC was  $\Delta n \equiv n_{\parallel} - n_{\perp} \approx 0.18$ , where  $n_{\parallel}$  and  $n_{\perp}$  are ordinary and extraordinary refractive indices. The dielectric anisotropy of the NLC used was  $\Delta\epsilon \equiv \epsilon_{\parallel} - \epsilon_{\perp} \approx 10$ . The electric field profile (inside the cell) was generated with the help of a uniform indium tin oxide (ITO) layer (on the first substrate) and a combination of a hole shaped electrode (with an internal diameter of CA=0.55 mm) and a weakly conductive layer of  $\approx 40\text{M}\Omega/\text{sq}$  sheet resistance (on the second substrate). Both substrates were further covered by planar alignment layers (Polyimide), which were rubbed in "anti-parallel" directions to obtain a mono domain cell with approximately  $\alpha \approx 3^\circ$  of pretilt angle (the angle between the local averaged molecular orientation, the so-called *director* [115], and the cell substrates). The details of cell fabrication can be found elsewhere [120; 121; 109]. The thickness of the NLC layer was maintained at  $L = 40 \mu\text{m}$  by means of spacers (inserted in advance within the peripheral adhesive walls).

The control of the OP of this lens was performed for fixed voltage values (see hereafter) by changing the frequency of the electrical signal (square shaped AC), see, e.g. [121]. The OP and aberration values were detected by means of a Shack-Hartmann wave front sensor. Obtained results are summarized in Fig. 1.1.

Since the TLCL is a flat electrically variable GRIN lens, its OP variation range scales quadratically with the inverse of its radius  $r = \text{CA}/2$  (see, e.g. [120]):

$$OP = \frac{2 * \Delta n * L}{r^2} \quad (1.1)$$

Large  $L$  (40  $\mu\text{m}$ ) and small  $r$  (0.275 mm) values explain the relatively large OPs observed experimentally (Fig. 1.1(a)). Indeed, the corresponding theoretical estimation (using Eq.(1.1)) shows that the maximum possible  $OP_{max} \approx 190\text{D}$ . However, the LC orientation is also non

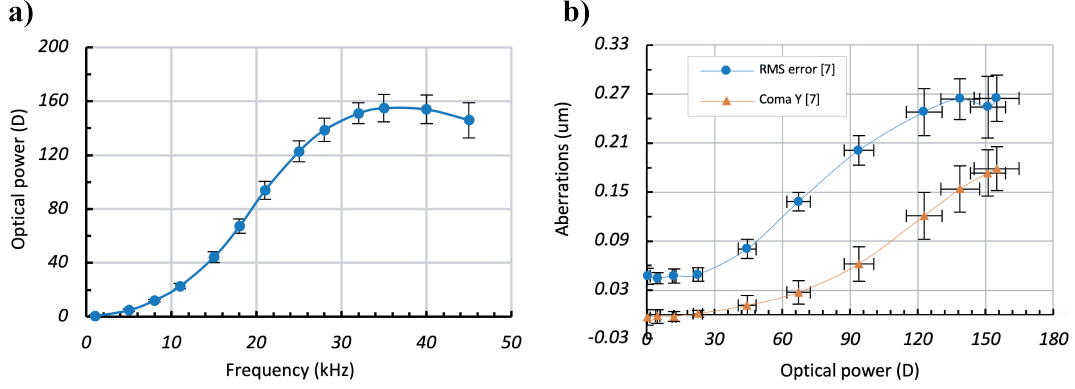


Figure 1.1: **a)** Optical power (in diopters) versus control frequency (in kHz) and **b)** circles - total RMS aberrations (in  $\mu\text{m}$ ) and triangle - separated coma aberrations versus the optical power for the TLCL.

uniform along the light propagation direction (in the non-saturated mode, the LC reorientation could be described by a half sinusoid: zero at boundaries and maximal in the center of the cell since we have strong boundary alignment conditions on cell substrates) that reduces the effective modulation depth of the refractive index. Typically, we can use a factor of  $\approx 0.85$  (for the "efficiency" of use of  $\Delta n$ ) to obtain the experimentally achievable values. This would bring us down to  $\approx 161\text{D}$ , which matches perfectly with our experimental data (Fig. 1.1(a)).

Most importantly, we can see the significant contribution of the systematic coma aberration (triangles, Fig. 1.1(b)) in total RMS aberrations of the TLCL. One possible solution to this problem (based on the stack of NLC layers) was discussed by S. Sato and co-workers [122]. Another solution (based on the segmentation of the hole patterned electrode) was discussed in [120]. The aimed-here endoscopic application would favor the first approach due to the desire to study the calcium activity in the brain [47], which requires relatively fast scans of image planes. The stacked solution may be preferred here since it allows the use of thin NLC layers and the reorientation (and thus focus scanning) time is proportional to  $L^2$ . This will be certainly more expensive approach, but the price is not a critical factor for this application. We shall thus further explore the stacked solution.

Figure 1.2 demonstrates the single and stacked solutions as well as the corresponding experimental results (all experiments were conducted by applying a square shaped AC signal with an amplitude ranging between 3.5 and 4.5 volts). Figure 1.2a demonstrates the observed strong coma in the case of a TLCL with single NLC layer (see the cell schematics, top left column). Traditional polarimetric set-up (Appendix, Fig. 1.5) was used (the TLCL was placed between two crossed polarizers, with the ground state director of NLC along the diagonal) to visualize the coma by fringe spacing (Fig. 1.2(a), the photo at the bottom left column; each bright fringe representing  $2\pi$  shifts on the transmitted phase front, see, e.g.

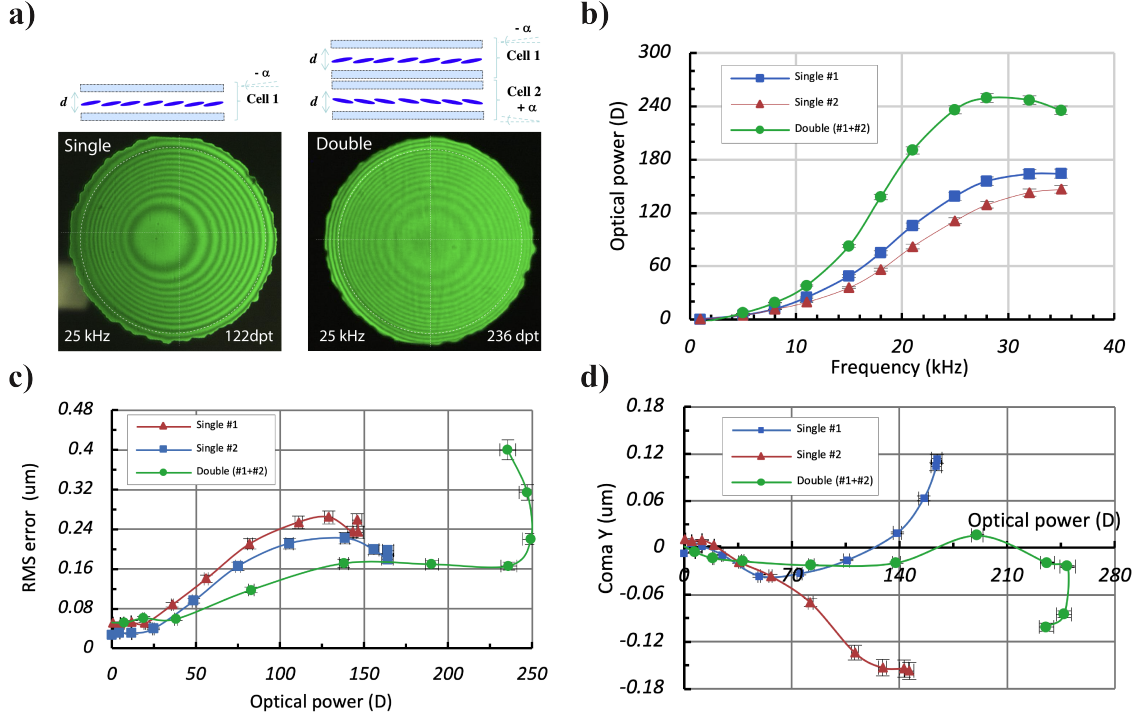


Figure 1.2: **a)** Demonstration of the strong coma in the case of a TLCL with single NLC layer (left column) and its compensation by the combination of two TLCLs with “opposed” pretilt angles (right column). **b)** Optical power (in diopters) versus control frequency (in kHz) for 2 TLCLs with single NLC layers (squares and triangles) and for one combined TLCL (double NLC stack, circles). **c)** Total RMS aberrations, **d)** Coma aberrations.

[120]). The right column of Fig. 1.2(a) shows its compensation by the combination (stack) of two TLCLs with “opposed” pretilt angles (see the cell schematics, top right column). Figure 1.2b shows the OP versus the control frequency for 2 individual TLCLs with single NLC layer (squares and triangles) and for their combination TLCL (double NLC layer with two “antiparallel” pretilt angles, circles, [47]).

As we can see (from Fig. 1.1(a)), the contrast of fringes is slightly degraded for the double cell. We think that this is related to the increased light scattering and to the imperfect alignment of two cells. It is interesting also to notice that the maximum achievable OP (circles, Fig 1.2(b)) for the double cell TLCL is less than the addition of OP values of two individual TLCLs. This might be related to the imperfect alignment of those cells as well as due to the fact that the focusing phenomenon is more efficient (stronger) for collimated beams while the use of the second TLCL becomes less efficient due to the wavefront curvature created by the previous TLCL.

Corresponding RMS and coma aberrations are demonstrated in Fig. 1.2(c) and figure Fig. 1.2(d), respectively.

As we can see, total and coma aberrations of the combined (double) cell are significantly better (lower) than the corresponding aberrations of two TLCLs with single NLC cells. This allows extending significantly the OP's variability range (Fig. 1.2).

## 1.5 Polarization aberration

We have seen that the obtained TLCL (with double NLC layers) can be used to focus (Fig. 1.2(b)) a linearly polarized light with good optical quality (Fig. 1.2(c) and Fig. 1.2(d)). However, as we have mentioned above, the fluorescence light is not polarized. There have been several studies addressing this issue. The use of TLCLs with so called blue-phase materials [123; 124] would not have such "polarization sensitivity" problem, but it would require much higher voltages, which is not compatible with mobile applications targeted here. The use of a specific scanning procedure and image processing algorithm might be another solution [125], but it will delay the scanning process and will complicate the video recording. We could change the imaging arm to use a lens with a single NLC layer in reflection geometry [126], but this would be a rather important design change. Binary (on-off) focus switching [127] also cannot be accepted here since we need a continuous scan. Those are the reasons why we shall further proceed with a straightforward solution [109], where we use two "double" TLCLs (rotated at  $90^\circ$ ) to record images with an unpolarized (fluorescence) light.

In combination with a GRIN lens assembly (a first GRIN of diameter  $\emptyset = 0.5$  mm, pitch = 0.5, NA = 0.2 combined with a second GRIN of  $\emptyset = 0.5$  mm, pitch 0.23, NA = 0.5; from GoFoton) the final stack (with the TLCL having a total of 4 layers) has demonstrated between 80  $\mu\text{m}$  and 90  $\mu\text{m}$  spatial shift. With a typical neuron size of 10  $\mu\text{m}$  - 20  $\mu\text{m}$ , this would be an excellent tool to study their behavior at several depths.

However, there are many ways how different individual TLCLs (with single NLC layers) may be assembled together to form the above-mentioned "polarization independent" stack. For example, if we consider the worst-case scenario where the stronger TLCL #1 (Fig. 1.2(b), squares) is placed (as shown in the Fig. 1.3(a)) before the weaker TLCL #2 (Fig. 1.2(b), triangles), followed by a rod-GRIN (OP = 2174D), and both TLCLs are controlled with the same electrical excitation signal (which is simpler and cost effective), then two orthogonal polarized images will be created at different distances (triangles). At the maximum OP (triangles, Fig. 1.3(b)), this mismatch may be more than 10  $\mu\text{m}$ , which will degrade the image of the neuron.

In contrast, if we invert the positions of those TLCLs, the mismatch will not be completely eliminated, but the situation will be noticeably improved (squares, Fig. 1.3(b)). Obviously, the best scenario would be to drive those lenses individually (circles, Fig. 1.3(b)) if it is acceptable from cost and complexity points of view (in this particular case, it is). Using our

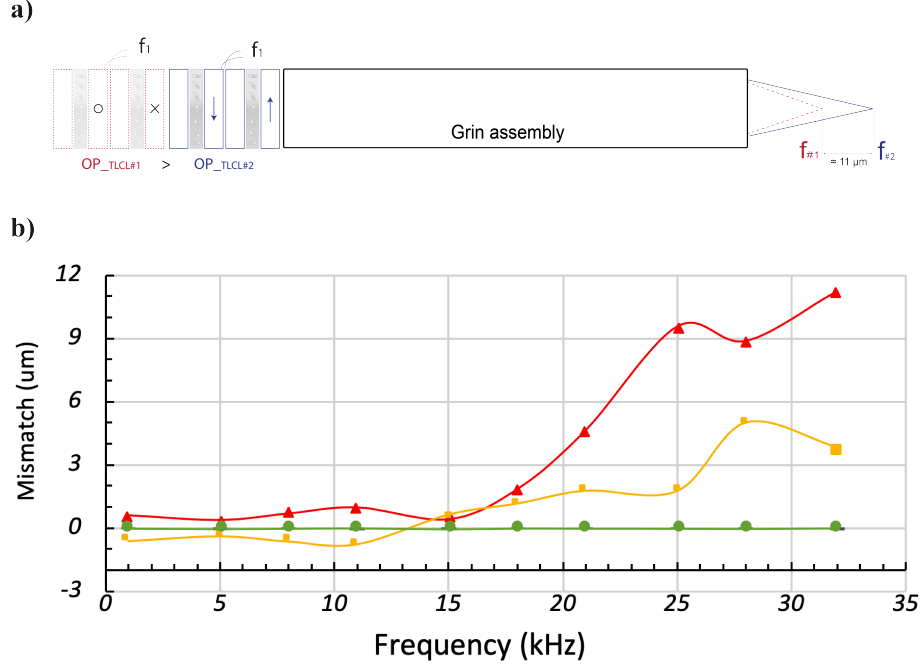


Figure 1.3: **a)** Schematic demonstration of one possible TLCL stacking option (to demonstrate the polarization mismatch problem, triangles). **b)** Mismatch values (in  $\mu\text{m}$ ) versus the control frequency (defining the OP of the lens) for two slightly different TLCLs (with different OP values, *Table 1.1*) and extreme cases: triangles: wrong positioning; squares: the right positioning, circles: individual control (see text for details).

experimental data (OP versus driving frequency  $F$ , Fig. 1.2(b)) and Zemax simulations, we can find the drive parameters (*Table 1.1*) enabling the complete elimination of this polarization mismatch (circles, Fig. 1.3(b)).

Frequency (kHz) TLCL 1	Optical Power (D) TLCL 1	Optical Power (D) TLCL 2	Frequency (kHz) TLCL 2
1	-4.9	-2.5	0.3
5	5.9	7.4	4.1
8	18.9	21.4	7.6
11	34.8	38.1	10.6
15	78.6	78.3	15.2
18	129.6	130.8	18.9
21	184.7	189.7	22.8
25	238.2	251.2	24.4
28	266.0	272.4	24.1
32	273.6	285.8	23.9

Table 1.1: Values of drive parameters used for obtaining minimal polarization mismatch.

To provide a quantitative tool that may be used for TLCLs' stacking strategy, it is impor-

tant to evaluate the impact of the focus mismatch (polarization aberrations) on the recorded image quality. Surprisingly enough, despite the growing popularity of TLCLs, the articles describing this problem are rather rare [128]. We have thus decided to characterize those polarization aberrations by using a simple stack of two TLCLs with cross oriented ground state directors (a total of two NLC layers). Figure 1.4a describes the experimental set-up used for this purpose.

Periodic black and white (10  $\mu\text{m}$  width) colored stripes were used as object 1 to be imaged. The imaging system was composed of an imaging rod-GRIN lens 2 (OP = 2174D,  $\emptyset$  = 0.5 mm, pitch = 0.23, NA = 0.5; from GoFoton), followed by the TLCL 3 and by a relay rod-GRIN lens 4 (OP = 328D,  $\emptyset$  = 0.5mm, pitch = 0.25, NA = 0.2; from GoFoton). Light from GRIN-TLCL-GRIN assembly was when collimated using microscope objective 5 (6.3X Neofluar, Zeiss) and transmitted to infinity-corrected tube lens 6 (ITL200, Thorlabs) specially designed for use with plan visible imaging to minimize chromatic aberrations across the field of view. Images were captured using CMOS camera 7 (DCC1645C, Thorlabs).

To estimate the quality of imaging, we have used the slope of pixel intensity variation  $\sigma = \Delta I / \Delta x$  (where  $\Delta I$  is the difference of pixel intensity and  $\Delta x$  is the difference of positions of pixels) between the black and white zones of obtained images. The reason for this choice is the non-uniform intensity distribution within the white zone of images (Fig. 1.4(a)) that makes difficult the identification of the contrast between black and white zones. At the same time, the degradation of image quality is clearly seen in the slope of transition between those zones when we change the polarization mismatch. To simulate a controllable polarization mismatch, we have started by choosing the driving frequency of 15 kHz for both cross oriented half lenses (in the optimal order, see squares in Fig. 1.3(b), and driven together). In this case, the image recorded had the best quality (middle photography, Fig. 1.4(b)) since two half lenses are providing similar OP values (and they are positioned in the right sequence). Then, one of the half lenses was kept in the same excitation state, while the other one (with perpendicular ground state optical axis) was driven with different frequency (below and above 15 kHz), generating thus different OP values. Images were recorded and the slope of the intensity (pixel value) change along the direction perpendicular to stripes was measured (Fig. 1.4(c)) for transition zones (between the white and black areas).



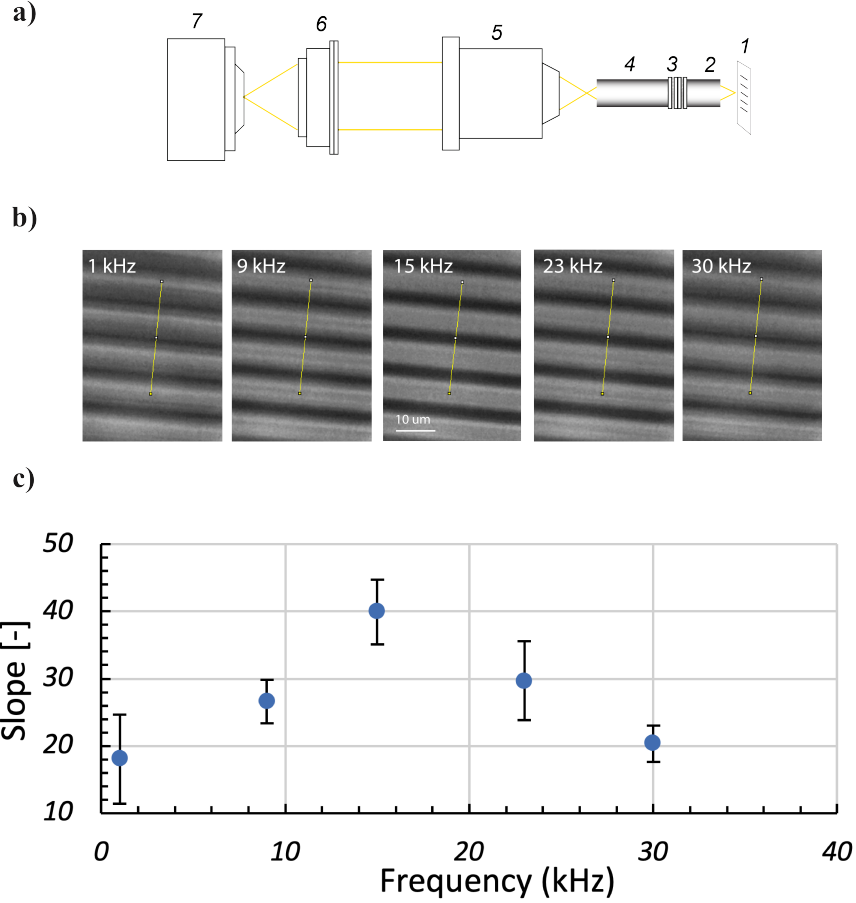


Figure 1.4: **a)** Experimental set-up used to characterize the impact of polarization mismatch on the quality of recorded images. **b)** micro photography of obtained images, **c)** intensity slope versus driving frequency of one TLCL (see the main text for details).

## 1.6 Discussions and conclusions

We have shown that RMS aberrations in general and the coma aberration in particular have been significantly improved by the cell stacking approach (Fig. 1.2(c) and 1.2(d)). However, that has created the problem of polarization aberrations. We have also demonstrated that we can reduce the degradation of image quality because of the polarization mismatch by an appropriate choice of the stacking sequence, TLCL characteristics and the driving technique.

Indeed, we have used this opportunity to study the resulting polarization aberrations of the endoscopic imaging system (TLCL and rod-GRIN assembly). Thus, as we can see from Fig. 1.4(b) and Fig. 1.4(c), the best transition slope (affecting the image quality) is obtained when two TLCLs are well synchronized and focus approximately at the same plane (driven at 15 kHz, corresponding to  $\approx 105\text{D}$  of OP, chosen deliberately to be in the strongest OP variation zone). However, the slope drops ( $\approx$  twice) when the mismatch of OP values for cross oriented TLCLs is  $\Delta\text{OP} \approx 44\text{D}$  (at 30 kHz).



It is important to emphasize that the polarization aberration problem must be considered within the framework of the optical assembly and target application. Thus, in combination with the above mentioned GRIN assembly; with a TLCL #1 driven at 105D (15 kHz) and the TLCL #2 being tuned from 64D (at 11 kHz) to 146D (at 23 kHz), we obtain a spatial mismatch that changes from  $-8.3 \mu\text{m}$  to  $+8.7 \mu\text{m}$  (relatively "limited" thanks to the presence of high power GRIN lens with  $\text{OP} = 2174\text{D}$ ). This mismatch indeed may appear to be limited, but we must keep in mind the typical sizes of neurons and their spines (at the order of  $1 \mu\text{m}$ ) that we are trying to image. In another context, the same driving conditions would generate a focus change ranging from  $-5.8 \text{ mm}$  to  $+2.8 \text{ mm}$  if the TLCLs are considered alone (without the GRIN lens).

In conclusion, we think that the proposed here solution (stacking TLCLs in the same and in perpendicular planes) will enable the construction of high quality miniature endoscopic systems for "mobile" imaging. We are currently building such endoscopes and our preliminary results confirm the above-mentioned statement. Corresponding results will be reported soon elsewhere.

## 1.7 Appendix

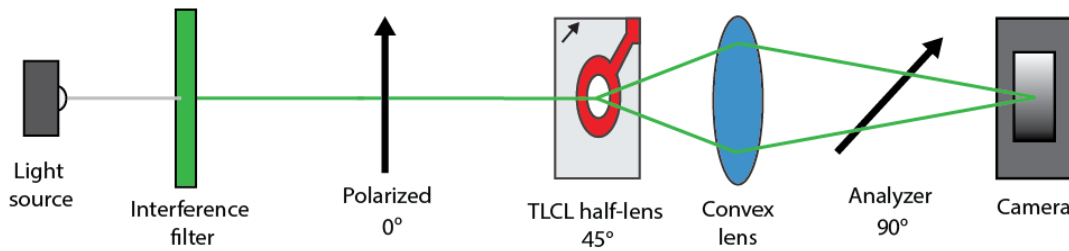


Figure 1.5: Polarimetry set-up that was used to visualize the interference rings (Figure 1.2). The arrow within the TLCL indicate the rubbing direction.

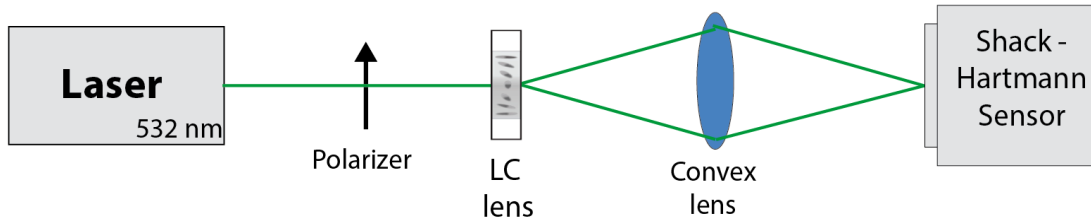


Figure 1.6: Shack-Hartmann set-up that was used to characterize the TLCLs (figure 1.1, 1.2). The reference plane wavefront was recorded in the air. Zernike coefficients (45) were recorded at different frequencies (Figure 1.1, 1.2) at fixed, optimal voltage.

## Acknowledgments

First of all, we would like to thank our collaborators in the field of ophthalmology. We would like also to thank LensVector *inc.* for the material and financial support of this work. We would like to thank FRQNT for the scholarship supporting AB. Finally, we would like to acknowledge the Canada Research Chair in Liquid Crystals and Behavioral Biophotonics (hold by TG) as well as NSERC and FRQNT for their continuous financial support.

## Chapter 2

# Motion-free endoscopic system for brain imaging at variable focal depth using liquid crystal lenses

Arutyun Bagramyan<sup>1,2</sup>, Tigran Galstian<sup>1</sup> and Armen Saghatelyan<sup>2,3</sup>.

<sup>1</sup>*Centre for Optics, Photonics and Lasers, Department of Physics, Engineering Physics and Optics, University Laval, 2375 Rue de la Terrasse, Quebec City, QC, Canada, G1V 0A6*

<sup>2</sup>*Quebec Mental Health Institute, 2601 chemin de la Canardière, Quebec City, QC, Canada, G1J 2G3*

<sup>3</sup>*Department of Psychiatry and Neuroscience, Faculty of Medicine, 1050 avenue de la Médecine, University Laval, Quebec City, QC, Canada, G1V 0A6*

Published in Journal of Biophotonics, Volume 10, Issue 6-7, p.762-774 (2017)

**Keywords:** liquid crystal lenses, gradient index lenses, adaptive 3D imaging, brain.

### 2.1 Résumé

Nous présentons un système sans mouvement mécanique pour l'imagerie microendoscopique de tissus biologiques à des profondeurs focales variables. Des lentilles à indice de gradient fixe et des lentilles à cristaux liquides électriquement modulables (TLCL) ont été utilisées pour construire la sonde optique. Le design de la TLCL permet de travailler avec la lumière non polarisée à des tensions relativement basses, améliorant considérablement l'efficacité énergétique du système. Un décalage focal d'environ  $74 \pm 3 \mu\text{m}$  pourrait être obtenu en contrôlant électriquement la TLCL en variant la fréquence et en maintenant la tension con-

stante. Le potentiel du système a été testé en imageant *in vivo* à des profondeurs différentes des neurones et épines de sections épaisses de cerveau de souris adultes . Nos résultats indiquent que le système développé permet l'imagerie en profondeur des propriétés morpho-fonctionnelles de circuits neuronaux chez des animaux se déplaçant librement et peut également être utilisé pour étudier le fonctionnement de ces circuits en conditions normales et pathologiques.

## 2.2 Abstract

We present a motion-free system for microendoscopic imaging of biological tissues at variable focal depths. Fixed gradient index and electrically tunable liquid crystal lenses (TLCLs) were used to build the imaging optical probe. The design of the TLCLs enables polarization-independent and relatively low-voltage operation, significantly improving the energy efficiency of the system. A focal shift of approximately  $74 \pm 3 \mu\text{m}$  could be achieved by electrically controlling the TLCL using the driving frequency at a constant voltage. The potential of the system was tested by imaging neurons and spines in thick adult mouse brain sections and *in vivo*, in the adult mouse brain at different focal planes. Our results indicate that the developed system may enable depth-variable imaging of morpho-functional properties of neural circuitries in freely moving animals and can be used to investigate the functioning of these circuitries under normal and pathological conditions.

## 2.3 Introduction

Biomedical imaging applications are growing very quickly that call for, among other requirements, the miniaturization of components used [129]. Such miniaturization is particularly important for assessing morpho-functional changes in neuronal populations in the brains of freely moving animals during specific behavioral states [130]. Particularly attractive are adaptive optical imaging systems that operate without mechanical movement or deformation. This is crucial for imaging deep brain regions at different focal planes. Deep brain imaging is currently performed on head-restrained animals where gradient index (GRIN) lenses are coupled to stepper motors to change the imaging plane [119; 131; 132] or on freely moving animals where small microscopes comprising the GRIN lenses are mounted on the head of the animal [119; 132]. In the latter case, the GRIN lenses are implanted in the brain at a fixed depth, limiting cell imaging to a single focal plane [119; 132]. In the former case, the presence of discrete moving parts, size and weight of these opto-mechanical systems are major limitations for studies on freely moving animals. To overpass those limitations recent studies have considered the use of different types of electrically variable lenses that operate without discrete moving parts, for example, based on actuated membranes [133] or electro-wetting effect [134]. However, their electric power consumptions are high, as the membrane

based device consumes  $\approx 1$  watt of electrical power, while the electro-wetting lens' typical power consumption is 15 mW. This raises the issue of their use with battery powered imaging systems for studies in freely behaving animal. In contrast, power consumption of liquid crystal (LC) lenses may be at the order of  $10 \mu\text{W}$  [92]. In addition to electro-wetting lenses, laser-scanning mirror systems were also demonstrated for micro-endoscopic imaging by using microelectromechanical system (MEMS) element [63]. However, this approach still uses discrete moving parts, which is rather complicated and potentially having high electric power consumption compared to LC devices.

Thus, alternative approaches must be considered to build efficient, small-size and low power consuming micro-endoscopes to image neural circuitry in freely behaving animal. Very small, efficient, motion-free adaptive imaging systems have been developed recently that are based on the mobile phone-driven miniaturization of cameras and components [92]. We think that LC materials [89; 94], which have been traditionally used to manufacture LC displays (LCD) [135], are the most promising tools for developing adaptive imaging applications [92; 136]. LCD manufacturing and electro-optic modulation schemes have also been successfully adapted to mass produce electrically tunable LC lenses (TLCL) [92] for autofocus mobile imaging [136] based on the creation and dynamic control of a lens-like gradient in the refractive index [137] by spatially non-uniformly reorienting the LC molecules (filled ellipses, Figure 2.1a,b) [92; 72; 138; 139; 140; 106; 141; 142; 143]. The extremely low power consumption ( $\approx 10 \mu\text{W}$ ), low weight ( $\approx 20 \text{ mg}$ ), and motion-free operation of these LC lenses [136] makes them ideal for mobile biomedical applications. Not surprisingly, recent studies used LC lenses for 3D imaging [144] and axial depth scanning [116].

Both of those works are very promising, however, the first one is discussing a multi-aperture 3D imaging approach that is out of the scope of our work. The second one describes a single aperture TLCL for endoscopic imaging [116], which is closer to the approach presented here, but has several practical limitations in terms of performing motion-free adaptive imaging in freely moving animals. First, it relies on relatively high driving voltages to change the optical power (OP). Indeed, given the large diameter of the hole-patterned electrode ( $\varnothing = 2 \text{ mm}$ ) and the relatively thin LC layer ( $d_{LC} = 50 \mu\text{m}$ ) [116] (Figure 2.1c), the hole-patterned electrode and the uniform indium-tin-oxide (ITO) electrode (cast on the bottom substrate of the LC chamber) must be separated by a rather large distance ( $d_g > 0.7 \text{ mm}$ ) to satisfy the condition  $\varnothing/(d_{LC} + d_g) \approx 2.5$  required to ensure smooth changes in the electric field along the  $z$  axis inside the LC layer to avoid large optical aberrations [72]. This, in turn, requires very high voltages to drive the lens because of the splitting of the electric potential difference applied between the hole-patterned and bottom ITO electrodes [142; 143]. The main decrease in the electric potential is thus applied over the middle  $0.7 \text{ mm}$  thick substrate, with significantly less over the LC layer [116]. Given the geometrical properties of the lens (Figure 2.1c) and the typical values of the dielectric constants of the middle glass substrate ( $\epsilon_g \approx 5$ ) and the

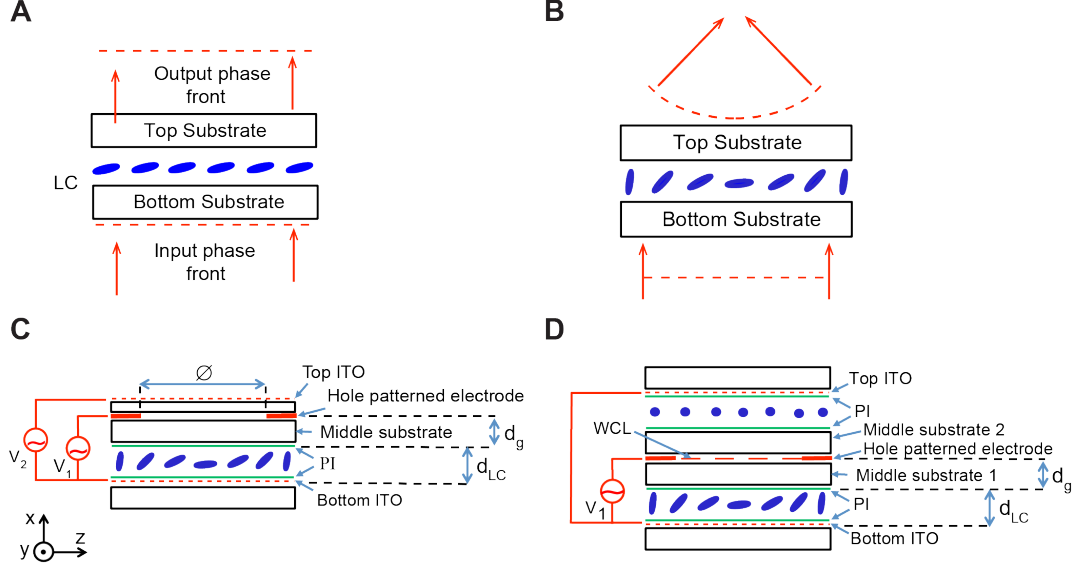


Figure 2.1: Schematic representation of the TLCL. **(A)** Ground state uniformly aligned LC layer (filled ellipsoids representing LC molecules between two substrates forming a chamber) without focusing power. **(B)** Spatially non-uniform (along the  $z$  axis) reorientation of LC molecules and focusing of the incident light (propagating along the  $x$  axis). The dashed lines show the phase fronts. **(C)** Schematic cross-sectional presentation of the polarization-sensitive LC lens focusing the light polarization parallel to the drawing plane. ITO: indium tin oxide transparent electrode, PI: polyimide alignment layer;  $d_g$ : thickness of the middle substrate;  $d_{LC}$ : thickness of the LC layer. **(D)** Schematic cross-sectional presentation of the polarization-insensitive LC lens using a single weakly conductive layer (WCL, dashed line in the middle) to drive two cross-oriented LC layers.

LC ( $\epsilon_{LC} \approx 4$ ), the applied voltage  $V_1$  is split (along the  $x$  axis, [143]) into a large decrease in the electric potential applied to the middle substrate :

$$V_g = \frac{V_1}{1 + \epsilon_g d_{LC} / \epsilon_{LC} d_g} \quad (2.1)$$

and a small decrease in the electric potential applied to the LC layer :

$$V_{LC} = V_1 - V_g \quad (2.2)$$

This results in a  $V_{LC}/V_g$  ratio of  $\approx 0.09$ , indicating that only one-tenth of the  $V_1$  is used to control the LC director (the local average orientation of the long molecular axes of the LC [89]). In addition, in order to electrically induce the reorientation of the LC director, the voltage applied to the LC layer ( $V_{LC}$ ) must be above a certain threshold value ( $V_{th}$ ) [94]

defined as :

$$V_{th} = \pi \left[ \frac{K}{\epsilon_0 |\Delta\epsilon|} \right]^{1/2} \quad (2.3)$$

where  $K$  is the elastic constant of the orientational deformation of the director,  $\epsilon_0$  is the dielectric constant of the vacuum, and  $\Delta\epsilon$  is the dielectric anisotropy of the LC at the frequency of the applied voltage, which is usually in the order of 1 kHz. It is easy thus to calculate, using the values of a typical LC mixture ( $\Delta\epsilon \approx 16.5$ , and  $K \approx 21 \times 10^{-12}$  N), that the value of  $V_{th}$  is approximately 1.2 V. This, in turn, means that the lens geometry requires a voltage that is at least 10 times higher in order to initiate the reorientation of the director, while an even higher voltage is required to operate the lens ( $V_{LC} > V_{th}$ ) [116]. To reduce the voltage required to operate the lens, the electrodes must be brought closer together by reducing the thickness of the middle substrate. However, this results in an abrupt change in the electric field profile inside the LC layer along the  $z$  axis, generating unacceptable optical aberrations. To overcome this problem, the modal lens method can be used [138; 139]. Indeed, another imaging system that uses a lens operating with low driving voltages has been reported recently [144]. However, this system also relies on the use of a polarizer, since the single nematic LC (NCL) layer usually focuses only half of the natural or unpolarized light [92], dramatically decreasing the energy efficiency [134] of the imaging system, particularly when both excitation (illumination) and imaging are performed through the TLCL. These two limitations (the use of a polarizer and high voltages) make such systems unacceptable for the mobile adaptive imaging of freely moving animals.

In the present work, we used a polarization-independent TLCL and relatively low driving voltages to perform endoscopic depth imaging. We characterized the OP and root mean square (RMS) aberrations of the TLCL as well as the resolution of the adaptive endoscopic assembly comprised of the TLCL and the fixed GRIN lenses. We then showed how the device can be used for motion-free imaging of neurons in thick brain sections and *in vivo*, in the adult mouse brain.

## 2.4 Materials and methods/experimental

### 2.4.1 Electrically variable lens design

We used an optimized modal lens approach [134] to design a polarization-insensitive optical probe that requires relatively low driving voltages to perform endoscopic depth imaging (Figure 2.1d). A thin, weakly conductive layer (WCL) of ZnO film ( $\approx 10$  M $\Omega$ /sq. sheet resistance) was cast over the hole-patterned electrode [72; 138] (Figure 2.1d, dashed line in the center of the structure) to form a so-called control layer. This layer was used to generate a gradually varying electric field profile along the  $z$  axis that was applied to the NLC layer.

The WCL made it possible to bring the hole-patterned and the bottom uniform electrodes much closer together and thus to significantly reduce the required driving voltage. However, it is important to remind that two perpendicularly oriented single-layer NLC "half" lenses (Figure 2.1b-c) are traditionally required to focus natural or unpolarized light. The NLC half lenses must be identical and must be positioned very close to each other to focus two orthogonal polarization components of natural light on approximately the same point [92]. The fabrication of identical and reliable WCLs is a very challenging task, which is why we used a recently developed NLC lens with a special geometry [145] (Figure 2.1d). The lens in question uses a single WCL control layer to regulate two NLC layers. Each NLC layer has a director that is oriented in a plane perpendicular to the plane of the second NLC layer (xz for the bottom NLC sandwich and xy for the top NLC sandwich, Figure 2.1d). Top and bottom ITO electrodes (dotted horizontal lines) are placed inside the sandwiches. The middle hole-patterned electrode consists of a thin film of Ag alloy that is biased with respect to the ITO electrodes by a square-wave AC voltage ( $V_1$ ). The thicknesses and dielectric constants of middle glass substrates 1 and 2 and the NLC layers were the same for the two sandwiches. The final assembly was thus polarization-independent (or insensitive). The symmetric design of the lens made its fabrication and operation much simpler since only one WCL and two contacts (single voltage) were used to drive both NLC layers synchronously.

As mentioned above, the WCL made it possible to position the ITO and the hole-patterned electrodes closer together by using much thinner ( $100\ \mu\text{m}$ ) middle substrates. This also resulted in a more efficient use of the electrical voltage ( $U_{th} \approx 3.27\ \text{V}$ ) required to achieve the threshold voltage ( $V_{th} \approx 1.2\ \text{V}$ ) over the NLC layers.

The application of a  $V_1$  of the appropriate frequency generated a non-uniform (lens-like) reorientation of the NLC molecules (Figure 2.1d), that is, there was a greater reorientation of the NLC molecules at the periphery (close to the hole-patterned electrode) than at the center when viewed along the z axis. The corresponding electrically variable OP could then be expressed approximately as [92]:

$$OP = 2 \times \delta n \times d_{LC} / r^2 \quad (2.4)$$

where the OP is measured in diopters ( $D = \text{m}^{-1}$ ),  $\delta n$  is the effective refractive index difference between the center and the periphery of the lens,  $r$  is half the clear aperture diameter of the lens, and  $d_{LC}$  is the thickness of the NLC layer. With a given set of lens parameters (see the Experimental section), Eq.(2.4) allows us to determine a maximum achievable OP of  $\approx 50D$ .

#### 2.4.2 Fabrication of the electrically variable liquid crystal lens

The TLCL was fabricated using  $100\ \mu\text{m}$  thick glass substrates (Figure 2.1d). Thin uniform layers of ITO were deposited on the inner sides of the top and bottom substrates. Uniform



layers of an Ag alloy were deposited on the middle substrates and were etched to create the hole-patterned electrode ( $\emptyset = 1.10$  mm in diameter). The WCL was also deposited on one of the middle substrates. The two ITO layers and the internal (opposite to the WCL) sides of middle substrates were then covered with thin polyimide layers and were rubbed in anti-parallel ( $180^\circ$ ) directions to obtain a monodomain orientation of a custom NLC mixture [92]. The optical birefringence of the NLC was  $\Delta n \approx 0.2$ . UV curable adhesive walls containing  $40\ \mu\text{m}$  diameter spacers (to create uniform gaps) were printed at the peripheries of the top and bottom substrates. The final thickness ( $d_{LC}$ ) of the planar-oriented NLC layer was  $\approx 42\ \mu\text{m}$ . The isotropic phase of the NLC mixture ( $> 95^\circ\text{C}$ ) was injected into each of the two chambers. The final multilayer structure was sealed using a very thin ( $< 5\ \mu\text{m}$ ) transparent adhesive with a refractive index close to the refractive index of the glass. The lens was operated using the frequency-driving technique, as described elsewhere [145; 126].

### 2.4.3 Theoretical analysis of the endoscopic assembly

We used an imaging GRIN lens (0.5-NA, pitch 0.23) and a coupling GRIN lens (0.2-NA, pitch 0.24) (Grintech, Germany) to fabricate the final endoscopic assembly (Figure 2.2a) or optical probe (Figure 2.2b,c). The GRIN lenses were glued on both sides of the TLCL (Figure 2.2c) using an index-matched optical adhesive. The diameters of the GRIN lenses and the TLCL were 1.00 mm and 1.10 mm, respectively, with a total assembly length of  $\approx 8.53$  mm. The high NA end of the assembly determined the resolution of the imaging system, while the coupling GRIN lens with the lower NA (and lower optical aberrations) ensured optimal transmission of the collected light into a plan fluorite objective (see the final experimental set-up, Figure 2.2a). The working distance (WD) of the imaging assembly was electrically controllable from approximately from  $168\ \mu\text{m}$  to  $94\ \mu\text{m}$  (in water) using the TLCL while the WD of the coupling GRIN was fixed at  $140\ \mu\text{m}$  (in air).

### 2.4.4 Experimental set-up

We used ray tracing to predict the behavior of the basic TLCL + GRIN assembly. Since the light path dynamically changed only between the TLCL and the imaging GRIN lens, and remained unchanged elsewhere in the optical path, it was sufficient to take only these two elements into consideration to quantify the electrical shift of the focal point of the assembly (Figure 2.2d). The final ray position (e.g., for the perpendicular, with respect to the drawing plane, polarization) is thus described as:

$$Final_{RAY_{\perp}} = T3 \times R3 \times Grin \times R2 \times T2 \times TL \times T1 \times R1 \times Incident_{RAY_{\perp}}$$

$$\begin{aligned} \begin{bmatrix} y_{2\perp} \\ \alpha_{2\perp} \end{bmatrix} &= \begin{bmatrix} 1 & l_{water} \\ 0 & 1 \end{bmatrix} \times \begin{bmatrix} 1 & 0 \\ 0 & n_{grin}/n_{water} \end{bmatrix} \times \begin{bmatrix} \cos(g \times l_{grin}) & 1/g \times \sin(g \times l_{grin}) \\ -g \times \sin(g \times l_{grin}) & \cos(g \times l_{grin}) \end{bmatrix} \times \\ &\times \begin{bmatrix} 1 & 0 \\ 0 & n_{glass}/n_{grin} \end{bmatrix} \times \begin{bmatrix} 1 & l_{glass} \\ 0 & 1 \end{bmatrix} \times \begin{bmatrix} 1 & 0 \\ -1/f_{TLCL} & 1 \end{bmatrix} \times \begin{bmatrix} 1 & l_{glass} \\ 0 & 1 \end{bmatrix} \times \begin{bmatrix} 1 & 0 \\ 0 & n_{air}/n_{glass} \end{bmatrix} \times \begin{bmatrix} y_{1\perp} \\ \alpha_{1\perp} \end{bmatrix} \end{aligned} \quad (2.5)$$

where the TLCL is approximated as an infinitely thin lens,  $T$  is the translation matrix,  $R$  is the refraction matrix,  $TL$  is the thin lens (TLCL),  $l$  is the length of the element;  $n$  is the refractive index of the element,  $f$  is the focal length,  $g$  is the gradient constant of the lens,  $y$  is the beam height, and  $\alpha$  is the angle with respect to the optical axis. Since the centers of the two half-TLCLs (which formed the full lens) were  $\approx 240 \mu\text{m}$  apart, the approximate shift of focal distances of the half-lenses was  $\approx 2 \mu\text{m}$  at the maximal OP ( $V_{RMS} = 23\text{V}$  at  $F = 17 \text{ kHz}$ ). Since a total focal shift of  $\approx 74 \pm 3 \mu\text{m}$  could be achieved, the contribution of polarization aberrations should be rather small. The parameter values used to obtain these results were as follows:  $n_{grin} = 1.629$  (refractive index at the center of the GRIN lens),  $n_{glass} = 1.517$ ,  $n_{water} = 1.33$ ,  $n_{air} = 1.00$ ,  $l_{glass} = 125 \times 10^{-6} [m]$ ,  $l_{grin} = 2.05 \times 10^{-3} [m]$ ,  $g = 0.697 \times 10^3 [1/m]$ ,  $l_{water} = 168 \times 10^{-6} [m]$  to  $94 \times 10^{-6} [m]$ , and  $f_{TLCL} = -0.26 [m]$  to  $0.02 [m]$ . The same method was used to measure the focal shift in the air, with the only difference that the refractive index of imaging medium was  $n = 1.00$ .

#### 2.4.5 Preparation of brain slices and immunohistochemistry

Fluorescently labeled neurons in  $100 \mu\text{m}$  thick adult mouse brain sections were imaged. Neuronal progenitors of olfactory bulb (OB) interneurons were labeled by stereotaxic injection of viral vectors into the rostral migratory stream of the adult mouse ( $\approx 22\text{-}24 \text{ g}$ ) as described previously [146]. Briefly, the Flex-GFP AAV viral vector ( $100\text{-}300 \text{ nl}$ ;  $1 \times 10^{12} \text{ iu/ml}$ ; University of North Carolina vector core facility) was injected into the rostral migratory stream of adult CalretininCre mice at the following coordinates with respect to the bregma: anterior-posterior:  $2.55 \text{ mm}$ , medial-lateral:  $\pm 0.82 \text{ mm}$ , and dorsal-ventral:  $3.15 \text{ mm}$ . Three weeks later, the mice were given an overdose of pentobarbital and were perfused transcardially with 0.9% NaCl followed by 4% paraformaldehyde (PFA). Three weeks are required for neuronal progenitors to migrate into the OB and to differentiate into granule neurons. The brain was removed and was post-fixed in 4% PFA at  $4^\circ\text{C}$ . Horizontal sections ( $100 \mu\text{m}$  thick) were cut using a vibratome (VT 1000S; Leica, Germany) and were incubated with a primary anti-GFP rabbit antibody (1:1000; Life Technologies, USA) overnight at  $4^\circ\text{C}$  in 0.2% Triton X-100 and 4% BSA. The slices were then washed with PBS and were incubated with a secondary Alexa488 anti-rabbit antibody. The slices were mounted in Dako mounting medium.

#### 2.4.6 *In vivo* motion-free imaging at different focal depth

Adult 3-4 month-old GAD67-GFP and C57Bl/6 mice were used for the *in vivo* motion-free imaging at different focal depth. In GAD67-GFP mice all interneurons are labeled with GFP [147]. Since, however, GFP expression in these mice is not very strong and allows mostly for imaging at level of cell bodies, we have also used animals with virally infected neurons. For this we injected GFP-encoding lentivirus (100-300nl;  $1 \times 10^9$  iu/ml, University of North Carolina vector core facility) into the rostral migratory stream of adult C57Bl/6 mice to label adult-born OB interneurons. The following coordinates were used for 20-22 g mice (from bregma): for rostral migratory stream injection anterior-posterior: 2.55 mm; medial-lateral:  $\pm 0.82$  mm; and dorsal-ventral: 3.15 mm. After injection, mice were returned to their cages and kept for 4-6 weeks. For the imaging session, the animals were anesthetized with 2-3% isoflurane and positioned on the stereotaxic frame. After removing the scalp, we drilled a circular craniotomy centered over OB hemispheres or cortex. We removed the bones protecting the OBs (or cortex) while leaving the dura intact. The surface of the brain was constantly irrigated with oxygenated artificial cerebrospinal fluid (aCSF) containing the following (in mM): 124 NaCl, 3 KCl, 2 CaCl<sub>2</sub>, 1.3 MgCl<sub>2</sub>, 25 NaHCO<sub>3</sub>, 1.25 NaH<sub>2</sub>PO<sub>4</sub>, and 10 glucose. The temperature of the animal was maintained at 37.5°C during the whole procedure using an infrared blanket (Kent Scientific). The imaging system composed of the GRIN and TLCL lenses mounted on the stepper motor was lowered to detect fluorescently labeled OB interneurons at anterior-posterior: 5.0 mm and medial-lateral:  $\pm 1.0$  mm or cortical interneurons at anterior-posterior: -0.5 mm and medial-lateral:  $\pm 1.2$  mm. Tip of the imaging GRIN lens was in aCSF and positioned approximately 130  $\mu$ m above the surface of the brain. The system was then fine focused using the TLCL.

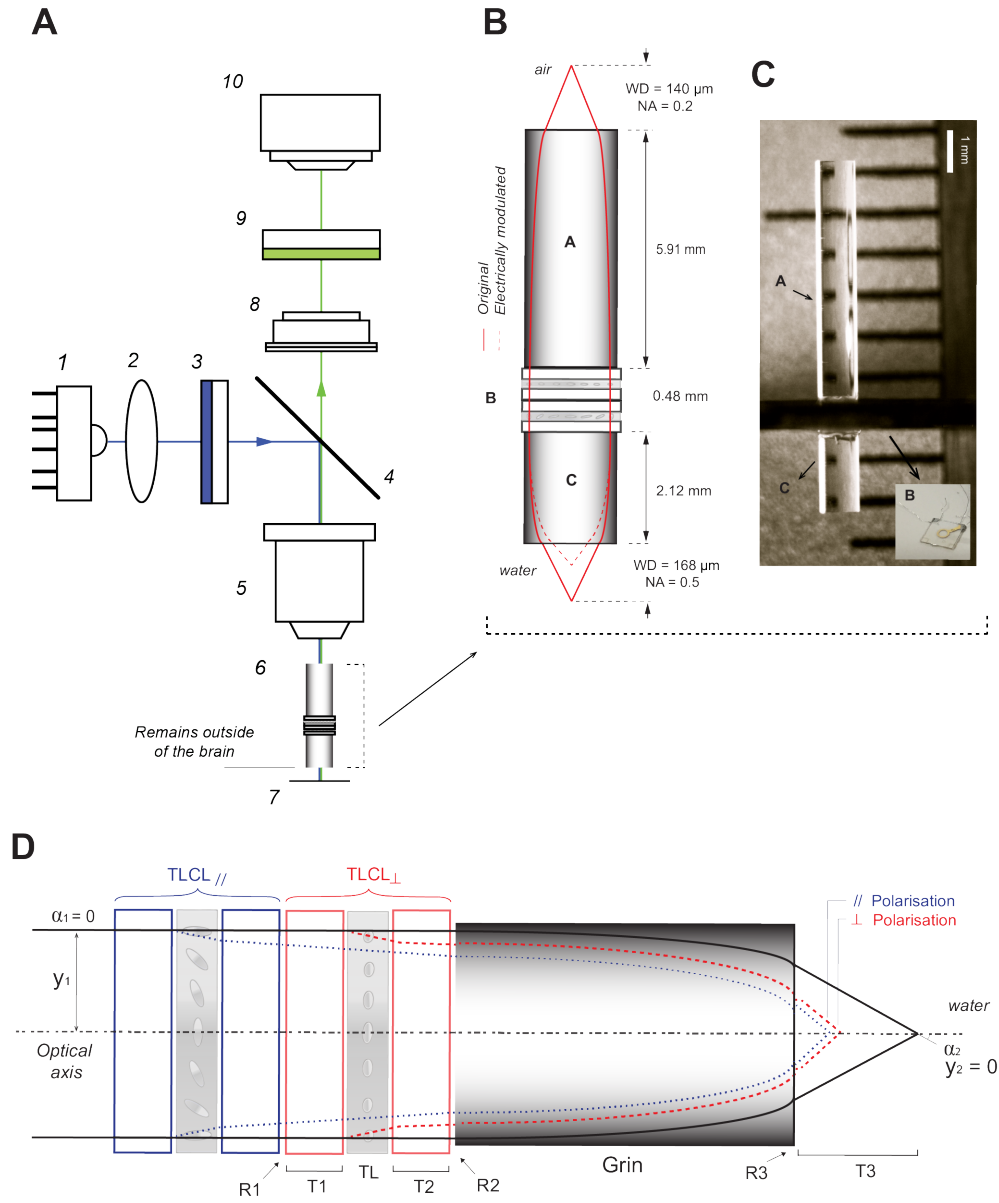


Figure 2.2: The optical probe and experimental set-up. **(A)** Schematic presentation of the final experimental set-up and components: 1. excitation light source, 2. aspheric lens, 3. excitation filter, 4. dichroic mirror, 5. objective lens, 6. GRIN-TLCL-GRIN probe, 7. biological sample, 8. tube lens, 9. emission filter, and 10. camera. **(B-C)** Cross-sectional presentation of the GRIN-TLCL-GRIN assembly as a schematic representation **(B)** and as a photomicrograph of the real sample **(C)**. A, B and C letters refer to coupling GRIN, TLCL and imaging GRIN, respectively. Magnification of assembled electrical probe is constant and is approximately equal to  $2.8 \pm 0.1 \times$ . **(D)** Schematic diagram of a single imaging GRIN lens-based optical probe used to derive the corresponding ABCD ray transfer matrix (Eq.(2.5)). The polarization-independent configuration is shown with the first  $TLCL_{//}$  (blue dotted) focusing the parallel polarization (with respect to the drawing plane) and the second  $TLCL_{\perp}$  (red dashed) focusing the perpendicular polarization.

## 2.5 Results and discussion

We started by characterizing the TLCL alone prior to assembling it with the GRIN lenses. The OP of the TLCL was measured using a Shack-Hartmann Wave Front Sensor (WFS150-7AR; Thorlabs). An AC square-wave electrical signal was applied to the TLCL using a function generator (AV-151b-c; Avtech Electrosystems, Canada). To determine the optimal working voltage of the TLCL, the frequency of the electrical signal was first kept steady at  $F = 15$  kHz and the amplitude ( $V_{RMS}$ ) was increased from 0 V to 27 V in 1 V increments. Some residual OP ( $\approx -3.8D$ ) was observed at 0 V due to the mechanical bending of the external surfaces of the TLCL in the non-activated mode (Figure 2.3a). Once the effective reorientation threshold ( $U_{th}$ ) was reached, the TLCL generated a weak but detectable OP. The experimentally measured value of this threshold was  $U_{th} \geq 3$  V, which was in good agreement with the theoretical value (3.27 V) calculated from the voltage division and threshold voltage equations (Eq.(2.2) and (2.3)). A monotonic increase in the OP was observed with the increase in voltage, with some saturation at  $V_{RMS} \approx 23$  V. No substantial OP was generated at higher voltages.

We then studied the OP of the TLCL at fixed amplitude while changing the frequency of the driving voltage (Figure 2.3b). The amplitude of the voltage was kept constant at a working voltage of  $V_{RMS} = 23$  V, while the driving frequency of the signal ranged from 1 kHz to 17 kHz. This experiment was performed first with one linear polarization of incident light and then with another linear polarization that was rotated  $90^\circ$  with respect to the previous one. The dynamic variation of the OP was measured by gradually varying the driving frequency until a saturation value of  $46 \pm 2D$  at 17 kHz was reached. The corresponding RMS aberrations are shown in Figure 2.3c. A very small decrease in the RMS error was observed when the frequency was increased from 1 kHz to 5 kHz, followed by an increase from 5 kHz to 13 kHz and then a decrease from 13 kHz to 17 kHz (see Discussion section). As can be seen in Figure 2.3b, there was no significant polarization mismatch, indicating that the device was polarization-independent.

We then experimentally measured the focal shift of the endoscopic assembly and compared it with the expected value (Figure 2.3d). We performed these measurements under conditions when imaging GRIN was positioned either in the air or in the water. The later case is particularly important for calculation of the focal shift in *in vivo* experiments since the refractive index of grey matter is close to the one of water [148]. The expected focal shift was calculated using the method described above (Eq.(2.5)). The experimental focal shift was determined using fluorescent beads that were mechanically defocused using a motorized actuator and were brought back into focus by tuning the frequency of the AC signal applied to the TLCL. The amplitude of the signal was kept steady at  $V_{RMS} = 23$  V. The precisely known mechanically out-of-focus distance was put in correspondence with the optical compensatory shift generated by the TLCL. The shift values presented in Figure 2.3d were

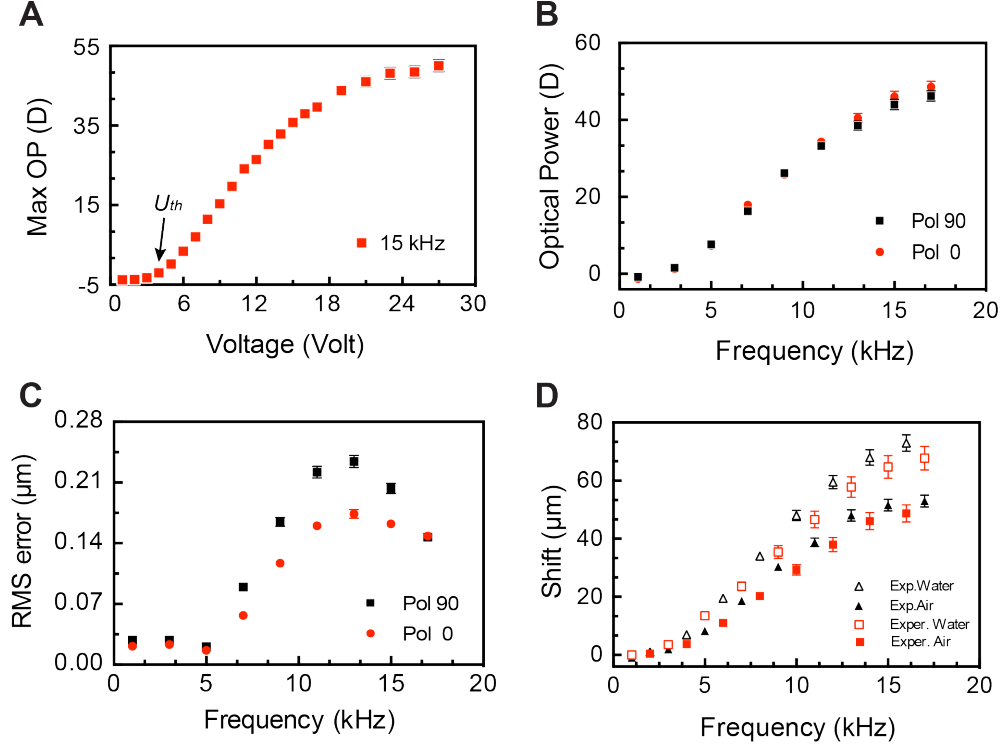


Figure 2.3: Characterization of the TLCL. (A) Optical power (in diopters, D) versus the applied AC voltage ( $V_1$ ) at 15 kHz. The effective threshold ( $U_{th}$ ) of the LC reorientation is shown by the vertical arrow. (B-C) TLCL OP at various driving frequencies at  $V_{RMS} = 23$  V. (B) OP dependence on the frequency of the driving voltage for two orthogonal polarizations of incident light. (C) Corresponding RMS aberrations as a function of the driving frequency for two orthogonal polarizations. Error bars (A-C) represent maximal fluctuations ( $\approx 3\%$ ) of the indicated measure during the acquisition period. ((D) Expected (theoretically estimated from TLCL OP measurements Eq.(2.5), open triangles) and experimentally measured (squares) focal shift values (in water and air) versus the driving frequency at a fixed voltage ( $V_{RMS} = 23$  V). Error bars (open triangles) represent the uncertainty on experimentally considered perfect focus position of microspheres. Error bars (open squares) are directly proportional to OP's error presented at (B).

directly proportional to the OP variation presented in Figure 2.3b. The initial shift of  $-1.5 \pm 0.1 \mu\text{m}$  at 1 kHz was increased by gradually varying the frequency until the saturation value of  $74 \pm 3 \mu\text{m}$  in water and  $53 \pm 2 \mu\text{m}$  in air at 17 kHz was reached. These experiments indicated that the electrical tuning of TLCL's OP allows for motion-free focal shift and that the focal shift is larger in the water as compared to the air.

Fluorescent polystyrene divinylbenzenemicrospheres  $\approx 1 \mu\text{m}$  in diameter were used to evaluate the resolution of the final imaging system composed of the optical probe, objective, camera, etc. (Figure 2.4). Microspheres were uniformly distributed on microscope slide using spin coating technic and covered with  $4 \mu\text{m}$  thick cover glass. Imaging GRIN lens was placed approximately at  $130 \mu\text{m}$  in the water or  $95 \mu\text{m}$  in the air, above the sample. Fif-

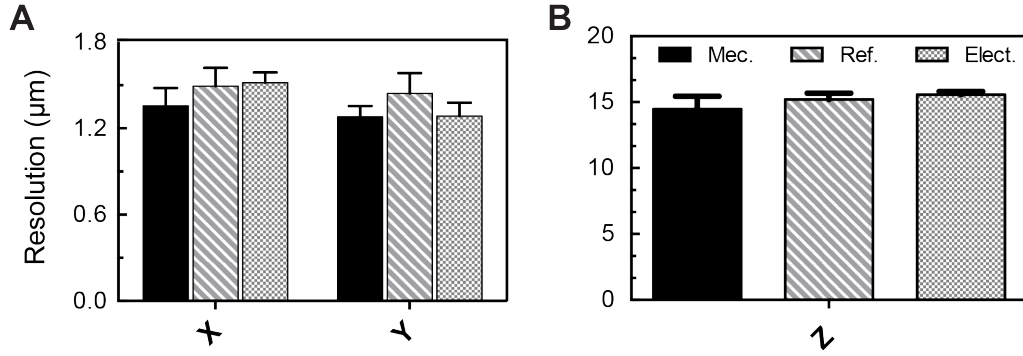


Figure 2.4: Characterization of the optical resolution of the assembly in the water. Driving the TLCL with frequencies ranging from 1 to 17 kHz performed the electrical scan. The fluorescent micro-spheres were perfectly focused at 9 kHz. Lateral (A) and axial (B) resolutions are shown. Error bars are standard deviation values ( $n = 4$ ).

teen images were captured, with a  $3 \mu\text{m}$  space between consecutive images (for a total of  $45 \mu\text{m}$  in depth). The scan was performed with at least four different microspheres. The point spread function (PSF) [149] was analyzed using ImageJ software. Three different measurement modes were used: the *Referencemode* consisted of a mechanical scan performed using a motorized actuator axially moving the entire set-up to generate the 3D PSF stack. The TLCL in this imaging configuration was replaced by a simple cover glass of equivalent thickness ( $500 \mu\text{m}$ ). The *Mechanicalmode* consisted of the same imaging mode as in the Reference mode but was performed using a TLCL with no noticeable OP. The *Electrical* mode consisted of electrically shifting the focal plane (with no mechanical intervention) by tuning the TLCL OP by increasing the frequency of the drive signal from 1 kHz to 15 kHz at a fixed voltage ( $V_{RMS} = 23 \text{ V}$ ), with the microspheres located in a focal plane at 9 kHz. The experimental data in Table 2.1 show that the electrical focal shift technique provided equivalent lateral (x,y) and axial (z) resolutions compared to the Reference and Mechanical modes.

Having confirmed that our imaging system performed well for adaptive electrical tuning in depth, we imaged OB interneurons (granule cells) at different focal planes in  $100 \mu\text{m}$  thick brain sections in the reflectance fluorescence configuration as shown on Figure 2.2a, with the excitation light set at 488 nm and the emission peak at 514 nm. Imaging GRIN lens was positioned in air and an electrical scan was performed by increasing the TLCL drive frequency from 3 kHz to 13 kHz at a fixed voltage ( $V_{RMS} = 23 \text{ V}$ ). At 5 kHz (Figure 2.5, top left), all the neurons in the field of view were out of focus. At 7 kHz (Figure 2.5, top right), the image contained one in-focus neuron in the center (indicated with a red arrow) while all the other neurons remained out of focus. Increasing the frequency to 10 kHz brought the other neurons into focus (Figure 2.5, bottom left) while the neuron that was in focus at 7 kHz was out of focus. Lastly, at 13 kHz, all the neurons were out of focus (Figure 2.5, bottom right).



We then assessed the ability of our system to image even smaller neuronal structures such as dendritic spines of OB granule cells. As can be seen in Figure 2.6b-e, the spines (in the yellow square) were clearly visible at 5 kHz, were distinguishable from the background at 7 kHz, and were completely out of focus at 3 kHz and 10 kHz. We measured the intensity profiles of the spines at different driving frequencies. The spines were clearly represented by the intensity spikes (Figure 2.6e) when the image was perfectly focused at 5 kHz (Figure 2.6b, c). At 7 kHz, the intensity contrast dropped and returned to baseline background levels at 3 kHz and 10 kHz.

	Mechanical ( $\mu\text{m}$ )	Reference ( $\mu\text{m}$ )	Electrical ( $\mu\text{m}$ )
<b>X</b>	$1.35 \pm 0.12$	$1.49 \pm 0.13$	$1.52 \pm 0.14$
<b>Y</b>	$1.28 \pm 0.08$	$1.44 \pm 0.14$	$1.29 \pm 0.19$
<b>Z</b>	$14.4 \pm 0.9$	$15.2 \pm 0.5$	$15.6 \pm 0.5$

Table 2.1: Resolution table with mean and standard deviation values for four fluorescent microspheres with three different imaging configurations.

Having shown that our system can be used for motion-free adaptive imaging at variable focal planes in brain sections, we performed *in vivo* imaging in the cortex of GAD67-GFP mice. Electrically tuning the TLCL using a fixed voltage ( $V_{RMS} = 23 \text{ V}$ ) and a variable driving frequency (from 3 kHz to 15 kHz) made it possible to perform motion-free imaging of interneurons at different focal planes. At 3kHz, the image (Figure 2.7, top left) contained some interneurons that were in focus (red arrows). At 8 kHz (Figure 2.7, top right), the other interneurons were brought into focus (red arrows). Increasing the frequency to 12 kHz brought other neurons into focus, but the neurons that were in focus at 8 kHz went out of focus (Figure 2.7, bottom left). At 15 kHz, the image contained other interneurons that were in focus (Figure 2.7, bottom right) while the neurons that were in focus at 12 kHz were out of focus.

Since GFP expression in GAD67-GFP mice is not very strong and does not allow to image neuronal dendrites, we also performed *in vivo* imaging in animals with virally-labeled cells. To this end, we imaged virally labeled periglomerular cells in the OB. The endoscopic imaging system was positioned at the surface of the OB and electrical tuning of TLCL from 1 kHz to 15 kHz allowed imaging of soma and dendrites of OB interneurons at different focal planes. At 1 kHz, the image contained OB interneuron had out-focused dendrites (Figure 2.8a-b, left). Increasing the frequency to 8 kHz brought the dendrites of these cells into focus (Figure 2.8a, middle and Figure 2.8b, right). At 15 kHz, the dendrites went again out of focus (Figure 2.8, right). These results confirmed that adaptive motion-free imaging combined with the electrical tuning of TLCL scan can be used *in vivo* to monitor cells at different



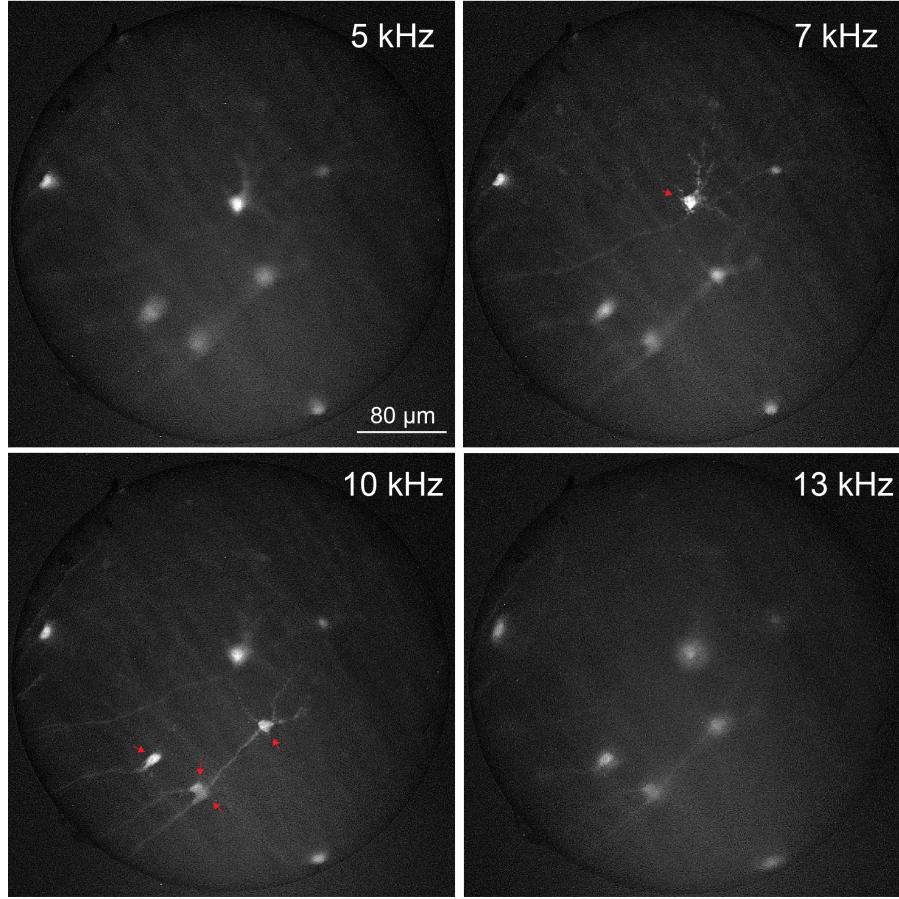


Figure 2.5: Imaging granule neurons in the adult olfactory bulb in thick brain sections. The red arrows indicate focused neurons. Using 5 kHz as the starting position, the shifts for 7 kHz, 10 kHz, and 13 kHz were  $10.0 \pm 0.6 \mu\text{m}$ ,  $23 \pm 1 \mu\text{m}$ , and  $37 \pm 2 \mu\text{m}$ , respectively.

focal planes.

We designed an adaptive imaging system that uses polarizer-free, motion-free electrical tuning of the focal plane to perform in depth imaging. The OP variation, polarization insensitivity, and dynamic aberrations of the system were very good. As expected, the OP of the system increased with the increase in the driving voltage and the frequency. We used 23 V as the operating voltage. However, it must be noted that the TLCL can be further optimized. For example, the same OP may be achieved with different voltage and frequency combinations that correspond to different types of aberrations of the TLCL. As such, this approach can be used to optimize the total aberrations of the endoscopic assembly.

The performance of our imaging system can also be further optimized by using thinner middle substrates that would decrease (Eq.(2.2) and (2.3)) the effective voltage threshold ( $U_{th} \approx 3.27 \text{ V}$ ) and operational voltage ( $\approx 23 \text{ V}$ ). Large  $30 \mu\text{m}$  thick glass panels are becoming commercially available and could be used to decrease the threshold value to  $U_{th} \approx 1.8 \text{ V}$ ,

which is very close to the “natural” threshold ( $V_{th} \approx 1.2$  V) of the NLC. This would lower the driving voltages ( $\leq 5$  V) required to operate the lens, which could then be battery powered.

Decreasing the thickness of the middle substrate would also further reduce polarizational aberrations. It should be mentioned, however, that the z resolution ( $15.6 \pm 0.5 \mu\text{m}$ ) of the current imaging assembly is not limited by this type of aberration.

We performed imaging in thick adult mouse brain sections and *in-vivo* in the adult mouse brain to show that our imaging system (incorporating a TLCL between two GRIN lenses) can be used for motion-free depth imaging that can allow a better understanding of the morpho-functional properties of neural networks *in vivo* under normal and pathological conditions. The GRIN and TLCL assembly can be easily incorporated into miniature head-mounted microscopes, which would make it possible to image the morpho-functional properties of neural networks at variable depth in freely moving animals. Our proof-of-principle experiments showed that our assembly can focus on neurons located at different depths by maintaining the GRIN lens in a static position and electrically tuning the TLCL lenses. Not only does TLCL tuning allow a  $74 \pm 3 \mu\text{m}$  focal shift to image neurons located at different depths, it also makes it possible to image dendrites at different focal plan and visualize spines. It should be noted that while spines were clearly visualized *in vitro*, in the acute OB slices, *in vivo* imaging was performed on neurons that do not have spines. Since, however the axial resolution of GRIN and TLCL assembly remains low, not all spines can be reliably identified and imaged. Altogether, the described imaging system offers great promise for implementation in miniature head-mounted microscopes to perform 3D imaging in freely behaving animals.

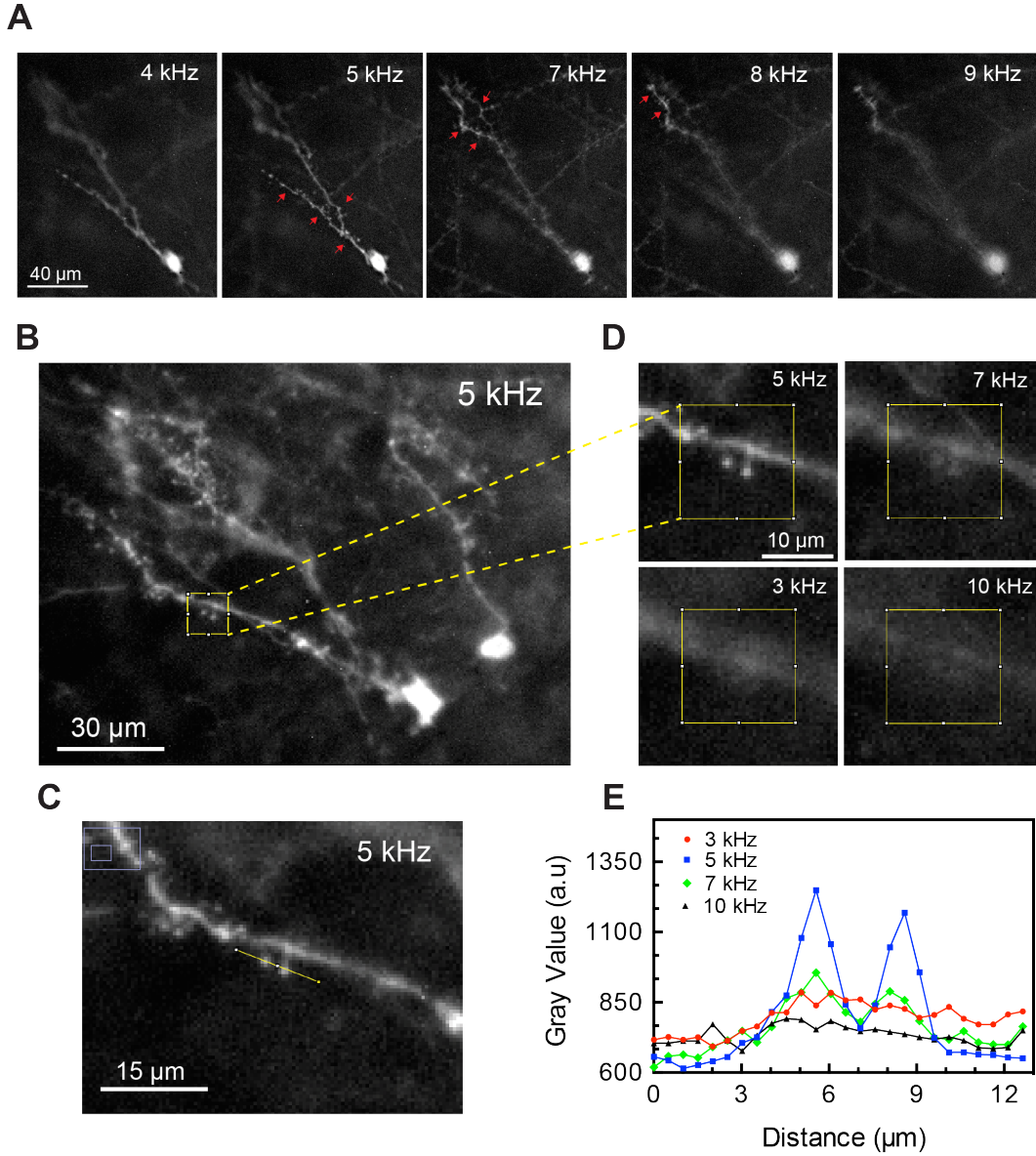


Figure 2.6: Imaging dendrites and spines with the optical probe assembly. **(A)** Imaging different dendritic segments of the same neuron by tuning the focal plane from 4kHz to 9kHz. The red arrows indicate focused dendritic segments. Defining 4 kHz as the starting position, the spatial shifts for 5 kHz, 7 kHz, 8 kHz, and 9 kHz were  $5.0 \pm 0.3 \mu\text{m}$ ,  $15 \pm 0.6 \mu\text{m}$ ,  $21 \pm 0.7 \mu\text{m}$  and  $27 \pm 0.8 \mu\text{m}$ , respectively. **(B)** Grayscale image of focused spines. **(C)** Two-time zoomed images of the spines in (B). **(D)** Images of spines at different depths during the electrical scan. Defining 3 kHz as the starting position, the shifts for 5 kHz, 7 kHz, and 10 kHz were  $7.0 \pm 0.3 \mu\text{m}$ ,  $17.0 \pm 0.6 \mu\text{m}$  and  $33 \pm 1 \mu\text{m}$ , respectively. **(E)** Intensity profile along the yellow line in the center of (C).

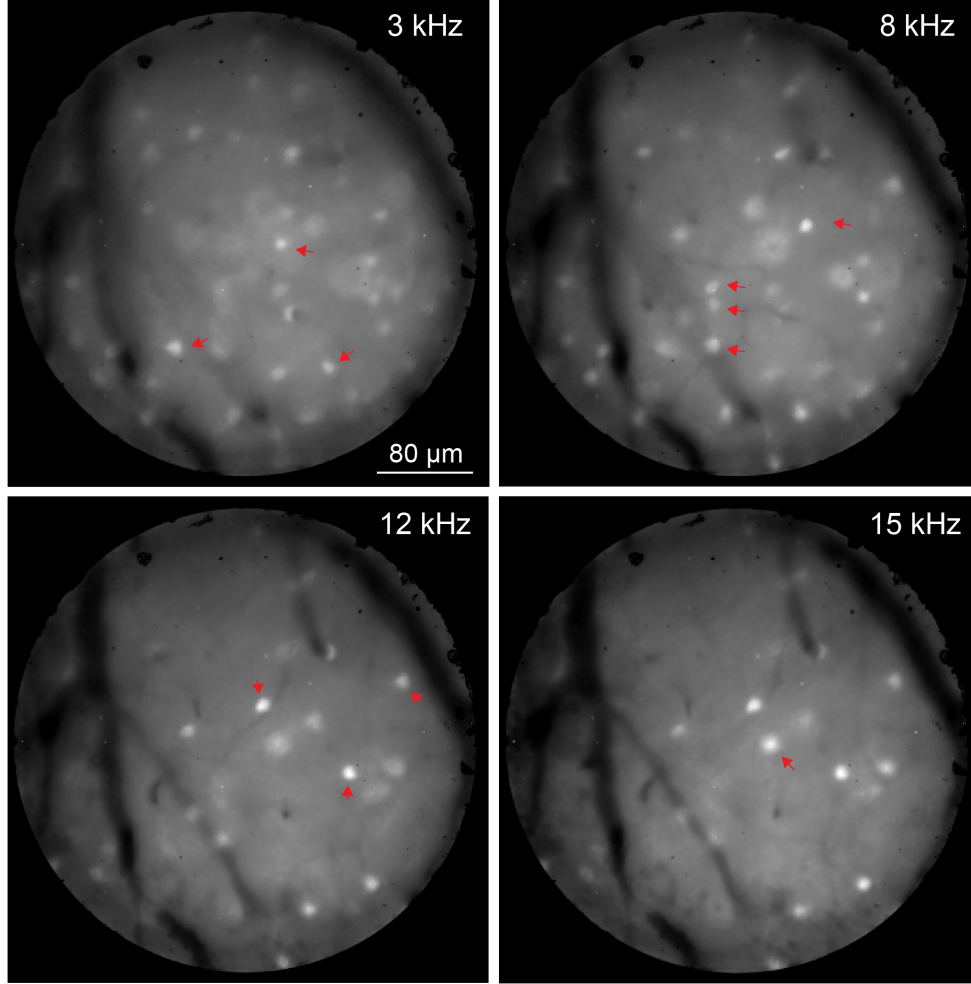


Figure 2.7: Motion-free variable-depth *in vivo* imaging of interneurons in the adult mouse cortex. Imaging of interneurons at different focal planes in the cortex of GAD67-GFP mice. The red arrows indicate focused neurons. Defining 3 kHz as the starting position, the spatial shifts for 8 kHz, 12 kHz, and 15 kHz were  $31 \pm 1 \mu\text{m}$ ,  $56 \pm 2 \mu\text{m}$ , and  $69 \pm 3 \mu\text{m}$ , respectively.

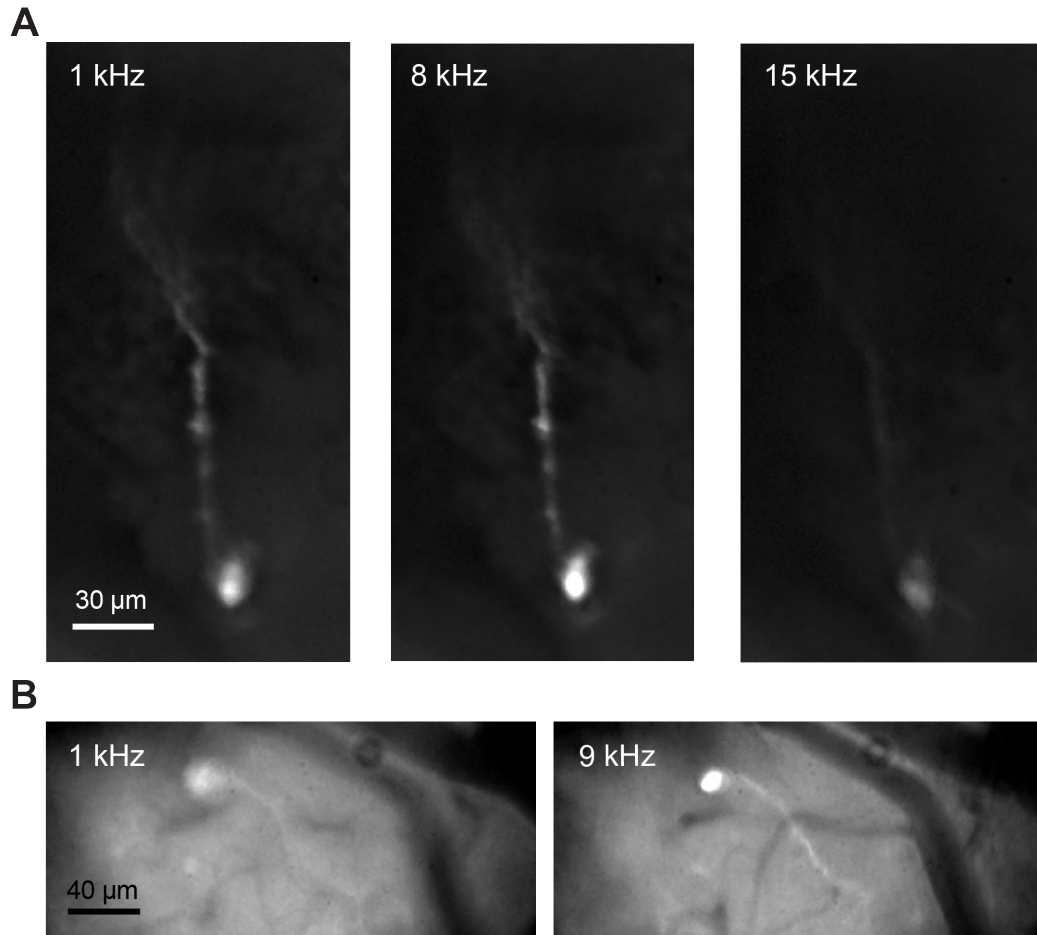


Figure 2.8: Motion-free variable-depth *in vivo* imaging of interneurons in the adult OB. **A.** Defining 1 kHz as the starting position, the spatial shifts for 8 kHz and 15 kHz were  $34 \pm 1 \mu\text{m}$  and  $720 \pm 3 \mu\text{m}$ , respectively. **B.** Defining 1 kHz as the starting position, the spatial shifts for 9 kHz was  $43 \pm 2 \mu\text{m}$ .

## 2.6 Conclusion

We designed an adaptive imaging system that offers several key advantages. The electrically variable LC lens geometry (the symmetry) and the driving mode allow for easy fabrication, simple control, relatively low voltages, and polarizer-free operation. The lens also makes it possible to dynamically control the depth of focus with a lower driving voltage and to eliminate the polarizer, significantly increasing the energy efficiency of the system (both for excitation and imaging) which enhances its potential for use in freely moving animals. The imaging system may enable time-resolved variable-depth imaging of the neural circuitry in freely moving animals, giving unprecedented access to the intricate details of the functioning of the brain in health and disease.

## Acknowledgements

This work was made possible by a grant from the Natural Sciences and Engineering Research Council of Canada (NSERC) to T.G. and A.S. and a grant from the Canadian Institutes of Health Research (CIHR) to A.S. A.B. was partially supported a CIHR training grant in neurophotonics. A.S. holds a Canada Research Chair in postnatal neurogenesis. T.G. holds a Canada Research Chair in liquid crystals and behavioral biophotonics and received the Manning Innovation Award 2014. We are grateful to Lensvector Inc. and TLCL Optical Research Inc. for their help and valuable advice.



## Chapter 3

# Lightweight 1-photon miniscope for imaging in freely behaving animals at subcellular resolution

**Arutyun Bagramyan**

*Center for Optics, Photonics and Laser, Department of Physics, Engineering Physics and Optics, Université Laval. 2375 Rue de la Terrasse, Québec (Qc), G1V 0A6, Canada*

Published in IEEE Photonics Technology Letters, Volume: 32, Issue 15 (2020)

### 3.1 Résumé

La miniaturisation des systèmes d'imagerie est devenue un critère important pour l'étude du cerveau de petits animaux se déplaçant librement (souris, oiseaux, etc.). L'auteur présente un miniscope à 1 photon avec des avantages mécaniques (poids: 1.3 g, petite taille: 10 mm x 17 mm x 12 mm) et optiques (résolution latérale: 1  $\mu\text{m}$ , grossissement:  $\approx 12.5$ , etc.) par rapport aux systèmes existants. Cet appareil peut être utilisé pour imager et étudier les structures cérébrales fines. Son design facilite l'intégration d'approches tel que le balayage en profondeur, la correction d'aberrations, l'éclairage structuré et le sans fil.

### 3.2 Abstract

Miniaturization of imaging systems has become an important requirement for studying the brains of small freely behaving animals (mice, birds, etc.). The author presents a 1-photon miniscope device with significant mechanical (weight: 1.3 g, small size: 10mm x 17mm x 12mm) and optical (lateral resolution: 1  $\mu\text{m}$ , magnification:  $\approx 12.5$ , etc.) advantages compared to existing systems. This device can be used to image and study fine brain structures

and its design is well-suited for the incorporation of future generations of depth scanning, aberration correction, structured illumination and wireless approaches.

### 3.3 Introduction

The development of miniature tools for studying the brain is one of the most important research topics in the field of neuroscience. *In vivo* imaging of different fluorescent structures in small animals is a rapidly growing area [27; 150]. Among the available technologies, 2-photon imaging platforms [151; 31] are able to image the brain of awake animals at sub-cellular resolutions with a relatively large penetration depth ( $\approx 800 \mu\text{m}$  from the surface of the brain) [152; 41]. Even though these systems have been improved over the last decade [29], they still restrain animal's movement, inducing stress and fatigue, as well as limiting the behavioral test repertory [48].

To overcome the above mentioned limitation, more studies consider imaging in a freely behaving animals using different types of miniaturized epifluorescence head-mounted imaging systems [153; 50; 49; 51; 47; 52; 130; 154]. These systems have the capacity to image at high frame-rates and are compatible with the future generation of wireless devices. Although several commercial (Inscopix, Doric) and open-source (UCLA's miniscope) versions of miniaturized 1-photon systems (M1Ss) are already available [49; 47; 154], they still have important limitations regarding their mechanical, optical and practical aspects. Namely, the currently available M1Ss are rather heavy, have low magnification ( $\approx 3\text{-}6$ ) and are limited to cellular resolutions [46]. This limits their application range to the imaging of large neuronal structures (soma) in the brain of adult animals. The present work addresses differently the use of M1Ss by proposing a new lightweight device for the imaging of fine brain structures in younger (smaller) animals. To describe this system, the author will begin by presenting the optical simulation and the ensemble of mechanical/electrical components necessary for the operation of the device. The author will then present experimental characterization of the optical (magnification, resolution, field of view (FOV), etc.), imaging (pixel resolution, frame-rate, etc.) and mechanical (weight, size, etc.) parameters of the M1S and demonstrate its ability to image various fine neuronal structures (e.g. dendrites, axons and spines).

### 3.4 Design and fabrication

#### 3.4.1 A. Optical design

Zemax Studio software was used to design and analyze the imaging characteristics of the developed M1S. Optical simulations were coordinated with mechanical requirements targeting the smallest size and weight possible. The main optical arms (excitation and imaging) of the device are schematically presented in Fig. 3.1(a) and described below.



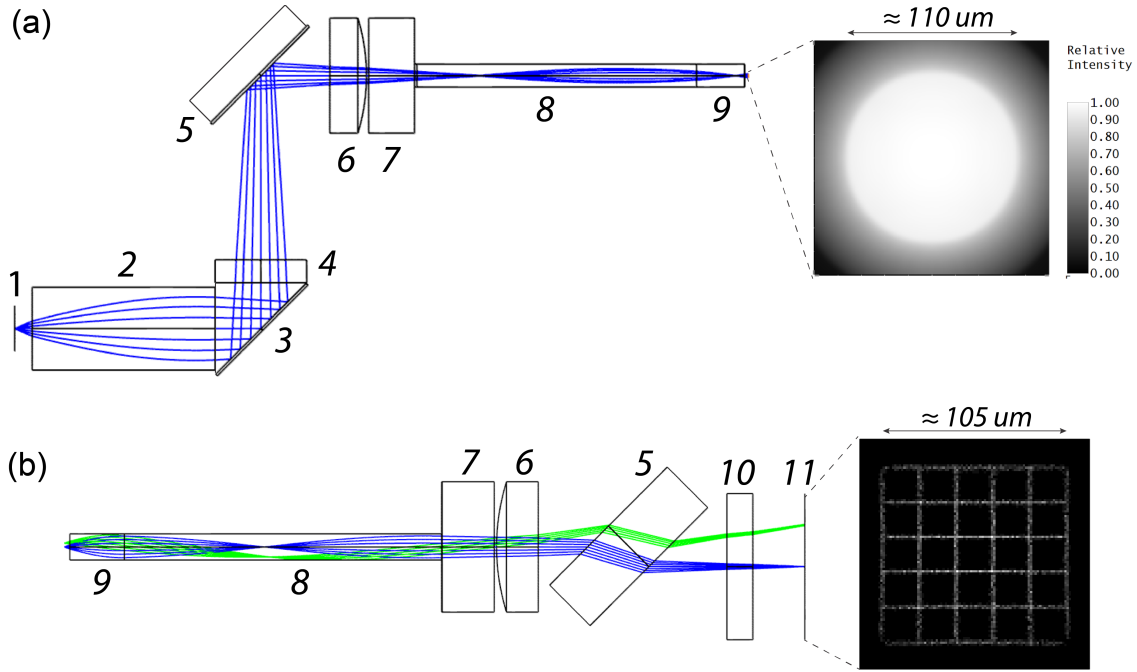


Figure 3.1: Design of the proposed M1S. **(a)** Excitation light pathway (left) with illumination field's photo with a diameter  $\approx 110 \mu\text{m}$  (right). **(b)** Imaging light pathway (left) with a photo demonstrating a FOV  $\approx 105 \mu\text{m}$  (right) which matches the dimensions of the excitation field (a).

**Excitation pathways:** Excitation light 1 (M470F3, Thorlabs) was collimated using a 1.8mm diameter rod-type gradient index GRIN lens 2 (#64-520, Edmund). Light was then reflected by a  $45^\circ$  prism 3 (#66-771, Edmund) with a pre-glued fluorophore matching excitation filter 4 (AT480/30, Chroma). The collimated light was then inserted (by a dichroic mirror 5, T510spxrxt, Chroma) into the common (with imaging arm, see below) segment, composed of a plano-convex lens 6 (#65-288, Edmund), a square cut glass 7 (22037246, Fisher Scientific) (used to fill the air-gap between 6 and 8) and the 0.5mm diameter GRIN lens assembly 8, 9 (custom). The final excitation beam had a  $110 \mu\text{m}$  diameter (Fig. 3.1(a)), which matched the size of the imaging FOV  $105 \mu\text{m}$  (Fig. 3.1(b)). **Imaging pathways:** Fluorescence light was collected using the imaging section 9 (numerical aperture  $\text{NA} = 0.55$ ) of the GRIN lens assembly (Fig. 3.2). Light was then transmitted by the low NA (0.2) segment 8 up to the square cut glass 7. A planoconvex lens 6 was used to focalize the emission light on complementary metal–oxide–semiconductor (CMOS) detector 11 (LI-OV7251M-FF-105H, Leopard Imaging) by passing through the dichroic mirror 5 and an emission filter 10 (AT535/40m, Chroma).

### 3.4.2 B. Optical probe design

To build the imaging GRIN assembly, 2 different GRIN lenses were used with an external diameter of 0.5 mm. Fluorescent light collection was maximized by the imaging GRIN ob-

jective with high NA ( $NA = 0.55$ ) and a length of 1 mm (0.23 pitch). Light from the imaging GRIN was transmitted to the rest of the system by using a 6 mm long (0.5 pitch) relay GRIN with  $NA = 0.2$ .

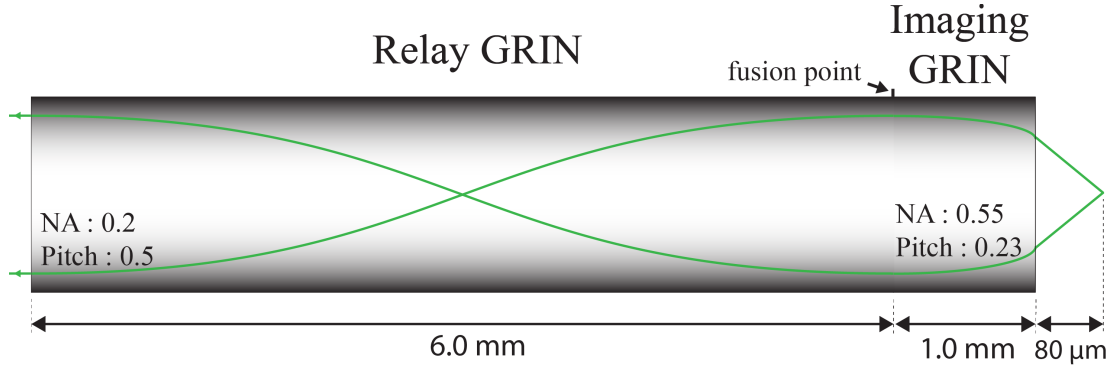


Figure 3.2: The imaging section of the probe is composed of a 0.23 pitch GRIN lens with NA 0.55 while the relay section is composed of a longer, ( $\approx 6$  mm long) GRIN lens with a pitch of 0.5 and  $NA = 0.2$

The final optical probe (Fig. 3.2) had a penetration depth of  $\approx 4$  mm (3 mm being lost in the mechanical holder, Fig. 3.3(b)), which is sufficient to reach some of the most important regions of the brain (hippocampus, various layers of the cortex, subventricular zone SVZ, etc.) [71]. To reach deeper regions, one can simply double the pitch number of the relay lens (Fig. 3.2) adding  $\approx 6$  mm length to the probe. The possible use of metallic tubing is not desirable here since it can increase the diameter by up to 40% (causing additional damage). The use of optical adhesives was also ruled out to reduce the risk of contamination of the imaging medium. Thus, the GRIN components (Fig. 3.1 (8 and 9)) have been fused (LZM-100, LazerMaster) to ensure the solidity of the final assembly while preserving the original diameter of 0.5mm. The final diameter of the probe remains small enough to be implemented without the practice of brain aspiration, which has been reported as a brain injury model [155; 156].

### 3.4.3 C. Mechanical/electrical parameters of the system

The raw data output from the monochrome CMOS camera (Fig. 3.3(a)) and the excitation light input of our M1S were transmitted by means of a custom made  $\approx 1$  m long extension cable 1 (homemade) and a 200  $\mu$ m core multimode optical fiber 2 (M89L01, Thorlabs), respectively. Both cablings (1, 2) were connected to the internal side of the rotary joint (RJ) system 3 (homemade) with an integrated light source 4 (M470F3, Thorlabs) and data acquisition controller 5 (LI-USB30-OV7251, Leopard Imaging). The RJ approach was used to compensate for the movement of the animal and to avoid the over-winding of the extension cable and the optical fiber. The illumination intensity of the source was regulated by using T-cube LED driver 6 (LEDD1B, Thorlabs) triggered by the DAQ #2, 7 (USB-6501, Na-

tional Instrument). Both components (6, 7) were connected to the computer using a standard USB2.0 cable. The same type of cable (2) was used to transmit the image data from our M1S and also the video recording from a second camera 8 (C922, Logitech) (used to monitor the behaviour of the animal during the imaging session) to the computer 9:

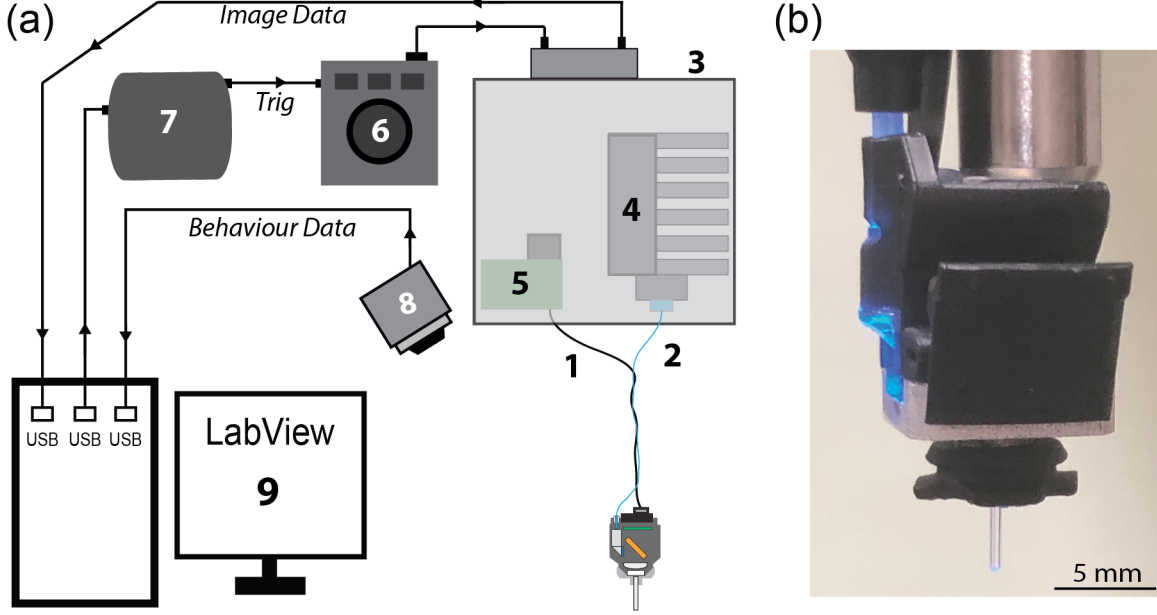


Figure 3.3: Schematics of the developed system. **(a)** M1S's input (1) and output (2) were connected to a homemade RJ assembly (3) with integrated light source (4) and camera DAQ (5). An homemade LabView software (9) controlled and synchronized the ensemble of system's components (1-8). **(b)** Picture of developed M1S with the excitation light (blue) switched ON.

The final miniaturized device presented in Fig. 3.3(b) had a total weight of  $1.3 \pm 0.1$  grams and dimensions of 10mm x 17mm x 12mm. The mechanical parts were printed using a Form 2 laser printer filled with black resin (RS-F2-GPBK-04). The maximal image acquisition rate is 50 fps at a 640x480 pixel resolution. The experimental system has a  $FOV = 105 \pm 5 \mu\text{m}$  (Fig. 3.5(a)), magnification =  $12.5 \pm 0.2$  ( $FOV_{IMAGE} / FOV_{OBJECT}$ ) and  $4.2 \pm 0.1$  pixel/ $\mu\text{m}$  ( $N_{PIXELS} / FOV_{OBJECT}$ ) object ratio. To visualize neuronal structures, the M1S can be attached to the implementable aluminum base containing the imaging objective probe (Fig. 3.2). The GRIN probe must be fixed on the animal's head in the targeted region of interest. Detailed installation/surgery protocols can be found elsewhere [55; 157]. Finally, the imaging parameters (frame-rate, gain, etc.) and time-lapse scanning options (pause, sequences, etc.) may be selected before recording the data (.tiff or .avi) using a home-made LabView software.

### 3.5 Results and discussion

The resolution of our optical system was characterized by measuring the full width at half maximums (FWHMs) of the simulated point spread function, PSFs (Fig. 3.4(a)). The obtained results (Fig. 3.4(c), dark grey) were slightly ( $\approx 26\%$ ) higher compared to diffraction limited values (Fig. 3.4(c), grey) and the difference can be explained by the aberrations of the optical components (Fig. 3.1 (6, 8 and 9)) used in the simulated system. To experimentally measure the PSF (Fig. 4(b)), the author imaged  $0.5\mu\text{m}$  diameter fluorescent microspheres (FSDG003, Bands Laboratories, Inc.) immersed in water (similar refractive index as the white and grey matter regions of the brain [148]).

Axial projection of microspheres was generated by mechanical displacements ( $2\mu\text{m}/\text{step}$ ) of the M1S system along the depth axis.

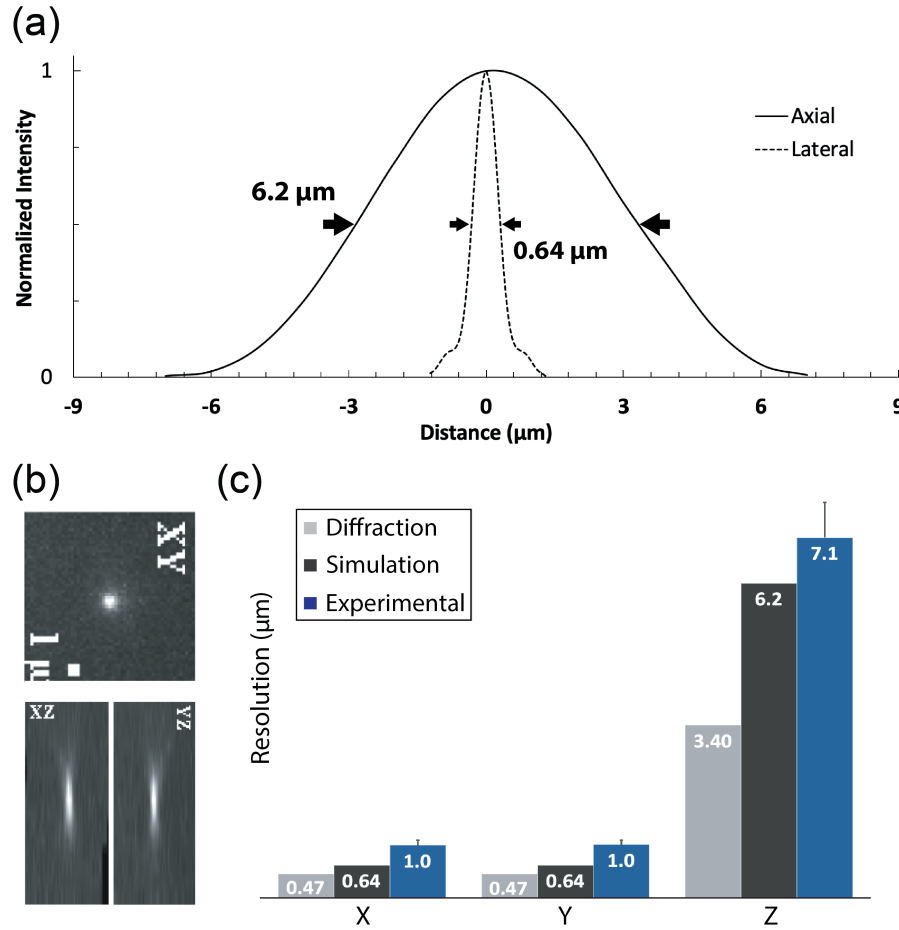


Figure 3.4: Resolution characterization (in water). (a) Example of lateral PSF generated by optical simulations (Fig. 1). (b) Example of experimental PSF generated by imaging fluorescence emission of a  $0.5\mu\text{m}$  diameter microsphere. (c) Summary of obtained theoretical, simulated and experimental results. MetroloJ (ImageJ plug-in) was used to analyze the data.

Experimentally obtained lateral (average of X, Y) and axial resolutions (Fig. 3.4(c), dark

blue) were equal to  $1.0 \pm 0.1 \mu\text{m}$  and  $7.1 \pm 0.7 \mu\text{m}$ , respectively. The difference with the theoretical simulations (Fig. 3.4(c), dark gray) can be explained by the imperfections within the experimental optical components and the quality of the assembling of the device.

The capacity to detect fine neuronal structures was demonstrated by imaging fixed brain tissue slices (Fig. 3.5). The presence of dendrites and spines was confirmed by visual and quantitative analysis presented in Fig. 3.5(b-d). Miniaturized 1-photon imaging is one of the most established methods for studying the brains of freely behaving animals. Despite the recent rise of miniaturized multi-photon or fiber scanning systems [55; 157], M1Ss remain useful due to their accessibility, price and compatibility with a future wireless approach [46]. To broaden the application repertoire of M1Ss, the author presents a lightweight miniaturized 1-photon microscope with novel mechanical and optical characteristics allowing to image fine neuronal structures in the brain of small, freely behaving animals. From an imaging perspective, the new optical design (Fig. 3.1) achieves a higher magnification ( $12.5 \pm 0.2$ ) and a higher pixel/object ratio ( $4.2 \pm 0.1$ ) compared to commonly used M1Ss [49; 47; 154] and can, therefore, be used to pinpoint the finest structures of neuronal circuitry. Naturally, the high magnification of this device and the use of a small diameter GRIN (0.5 mm) objective (Fig. 3.2) resulted in a reduction of the FOV  $\approx 105 \pm 5 \mu\text{m}$ , that is significantly lower compared to existing M1Ss (FOV  $\approx 350 \mu\text{m}$ ). To increase the FOV, one can consider imaging with larger diameter ( $\varnothing 1.0\text{-}1.8 \text{ mm}$ ) GRIN lens objectives, which are directly compatible with our device. However, this will cause additional damage to the brain, which may degrade the health and behaviour of the animal and so the author recommends the use of less invasive, small diameter GRIN objectives [158].

From the mechanical perspective, the proposed M1S is one of the smallest reported (10mm x 17mm x 12mm). The compact size of the optical design (Fig. 3.1) and the choice of mechanical frame material were the key factors allowing to achieve this result. The total weight of the M1S is  $\approx 1.0 \pm 0.1 \text{ g}$ , which is by  $\approx 40\%$  lighter than the closest alternatives [51; 47]. The proposed device will therefore significantly benefit the animal, improve the read-out of neuronal recordings under more natural behavioural conditions, permit longer periods of imaging and also enable investigations with younger subjects.

The ability to distinguish small neuronal features was demonstrated by imaging a thick brain tissue preparation with high level of scattering (similar to *in vivo*). Conventional signal enhancement protocols (e.g., immunocytochemistry) were avoided to preserve the same level of brightness compared to the real experiment. Even under more challenging imaging conditions (*in vivo* alike), multiple subcellular structures were clearly detected (Fig 3.5 (b,c)) and quantified (Fig. 3.5(d)). The author therefore expects the miniscope to be suitable for the *in vivo* imaging of very fine structures of the neuronal circuitry, such as axons, dendrites and even spines.

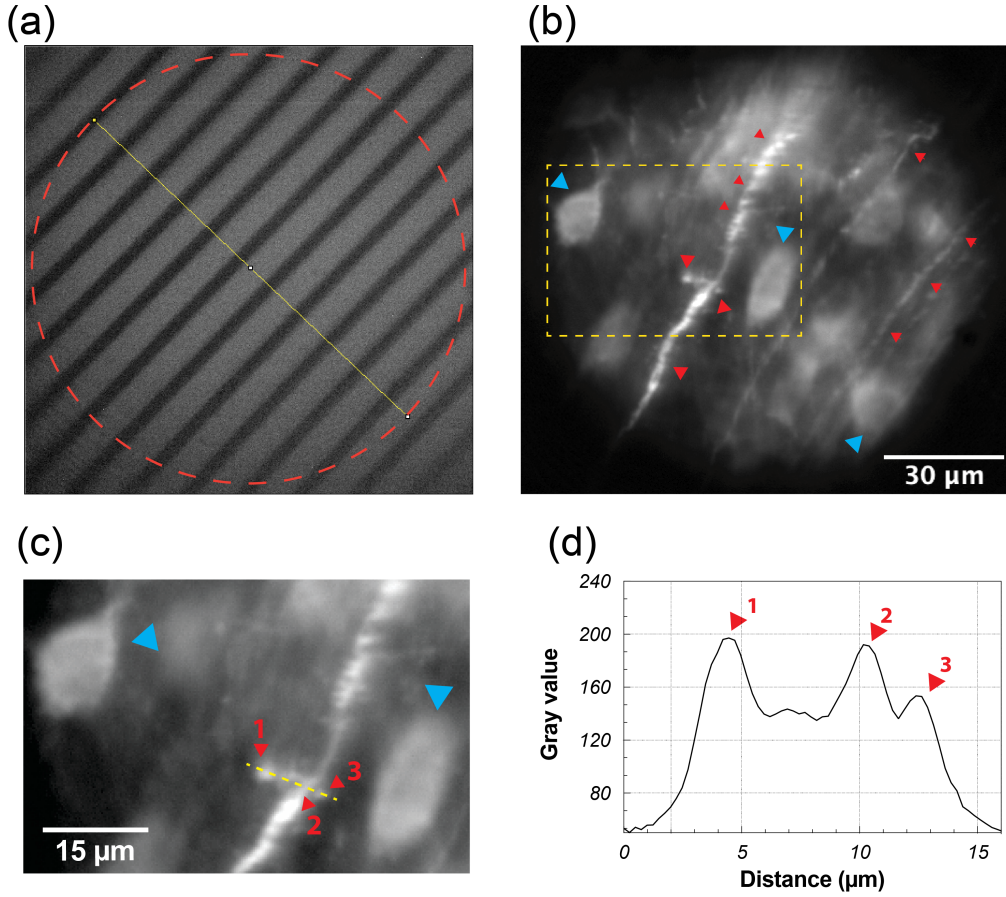


Figure 3.5: Imaging with the developed M1S system. **(a)** Scale target with 10  $\mu\text{m}$  spacings. Boundaries of the FOV ( $\approx 105 \mu\text{m}$ ) are indicated by the dotted line (in red). **(b)** *In vitro* images of a thick (100-150  $\mu\text{m}$ ) brain tissue expressing the fluorescent protein GCaMP6. The fine structures of neuronal circuitry and the multiple neurons (soma) are indicated with red and blue arrows, respectively. **(c)** Zoom on the dotted ROI in (b). **(d)** Pixel intensity profile through the yellow line in (c). Three peakes can be clearly distinguished from the background. ImageJ was used to process the data.

With an acquisition rate of 50 frames-per-second, this M1S is suitable for both structural and also functional [46] monitoring of subcellular structures over long periods of time. For example, the proposed M1S could be used to study the dynamics of fine structures in variant pathological, neurodegenerative conditions (Alzheimer's disease, Parkinson's, etc.) [159; 160] or for chronic observations in a group of aging animals where changes in spine densities have been reported [161; 162]. Moreover, because this M1S is significantly lighter than existing alternatives, it can be used to study the dynamics [163] of fine neuronal structures in younger animals.

### 3.6 Conclusion

Currently available M1Ss are commonly used to record  $\text{Ca}^{+}$  activity from a large pool of neuronal cell bodies in the brain of adult mouse. Here the author reported, to his knowledge, the first lightweight miniaturized 1-photon microscope with high magnification and subcellular resolution allowing to image fine neuronal structures in the brain of younger (smaller) animals. Promising *in vitro* results demonstrate the capacity to image dendrites, spines and suggest that this device can be used in freely moving animals, to address various physiological questions related to the synaptic plasticity, cognition, spatial navigation, etc. As a future perspective, the proposed M1S could easily be modified to add different options. The author is currently working on a depth scanning version of the device based on liquid crystal focus-tuning technology and also considering the development of lightweight 2-colour, and wireless M1Ss.

### Acknowledgement

The author would like to thank Prof. T. Galstian and Prof. F. Bretzner for their kind support. He would like also to thank LensVector inc. for the material and financial support of this work.

## Chapter 4

# Focus tunable microscope for subcellular imaging in freely behaving animals

Arutyun Bagramyan<sup>1,2</sup>, Loïc Tabourin<sup>1,2</sup>, Ali Rastqar<sup>2</sup>, Frédéric Bretzner<sup>2</sup> and Tigran Galstian<sup>1</sup>.

<sup>1</sup>*Center for Optics, Photonics and Lasers (COPL), Faculty of Science and Engineering, Department of Physics, Engineering Physics and Optics, Université Laval, Quebec City. 2375 rue de la Terrasse, Québec, QC G1V0A6, Canada.*

<sup>2</sup>*Centre de Recherche du CHU de Québec, CHUL-Neurosciences, 2705 boul. Laurier, Québec, QC G1V 4G2, Canada.*

Submitted to Nature Methods (2020).

### 4.1 Résumé

Nous présentons un nouveau microscope 1-photon miniaturisé qui utilise une lentille à cristaux liquides (TLCL) électriquement modulables pour réaliser un balayage en profondeur sans mouvement dans le cerveau de petits animaux se déplaçant librement. La TLCL fonctionne avec une basse tension de  $3.6 V_{RMS}$  et une consommation électrique  $\approx 1 \mu W$  et permet une modulation continue du plan d'imagerie sur toute la distance de travail de la sonde optique ( $\approx 100 \mu m$ ). Le microscope final est compact (10mm x 17mm x 12mm), léger (1.2 g) et permet une imagerie rapide (30-50 images/seconde) avec un grossissement élevé (8.7x) et une résolution de  $1.4 \mu m$  dans un champ de vue de  $150 \mu m$ . Le potentiel extraordinaire de l'appareil est démontré par l'imagerie adaptative de la fluorescence de GCaMP6s des dendrites et des épines du cortex moteur lors de différents comportements des animaux se



déplaçant librement.

## 4.2 Abstract

We present a novel miniaturized 1-photon fluorescence microscope that uses an electrically tunable liquid crystal lens (TLCL) to achieve a motion-free depth scan in deep brain zones ( $\approx 3$  mm) of small freely behaving animals. The TLCL enables continuous shift of the imaging plane across the entire working distance ( $\approx 100$   $\mu\text{m}$ ) of the optical probe using low voltage ( $3.6 V_{RMS}$ ) and low electrical power consumption ( $\approx 1$   $\mu\text{W}$ ). The final microscope assembly is compact (10mm x 17mm x 12mm), lightweight (1.4 g), provides fast imaging (30-50 frames/second), high magnification (8.7x) and a 1.4  $\mu\text{m}$  resolution within a 150  $\mu\text{m}$  field of view. The extraordinary potential of the device is demonstrated by adaptive imaging of GCaMP6s fluorescence from cortical dendrites and spines during a range of behavioural tasks in freely behaving mice.

## 4.3 Introduction

Over the last decade, the development of miniature microscopy has been instrumental in studying neural circuits of deep brain regions in freely behaving animals (FBA) [150; 46; 27; 28]. Whereas we have a rather good knowledge of how neuronal assemblies contribute to specific behaviors, less is known about their fine neuronal processes including dendrites and dendritic spines, wherein all neuronal communication occurs. Therefore, imaging small neuronal processes in FBA using genetically encoded calcium indicators or voltage-sensitive dyes [164; 165; 166] is the next step toward the understanding of brain functions in normal and neuropathological conditions. Benchtop 2-photon microscopy has been the first approach to record calcium transients from spines, dendrites and fine processes in the brain of head-restrained animals [29; 152; 41]. Although promising, head-restrained models cannot address normal behaviors such as grooming, locomotor gaits, or spatial navigation, nor can they address social interactions that require free movements of animals. Moreover, the absence of vestibular cues (induced by rotation of the head) can decrease the selectivity of space-coding neurons [42] and the activation of place-cell populations that may affect hippocampal coding [43]. Head fixation can also cause aberrant sensory feedback on the neck or the head, leading to stress, fatigue, and consequently abnormal neuronal processing, conditions that are no longer representative of normal functioning. To overcome this limitation, portable miniaturized high-resolution devices have been developed [66; 64; 61; 60; 67; 63; 62; 65]. Among these, a variety of fiber scanning techniques have demonstrated the capacity to record different small neuronal structures [66; 64; 61; 60; 67]. Although promising, these systems have multiple drawbacks regarding their size, weight, complexity of movement correction algorithms, and the sampling rate ( $\leq 5$  frames/second

(fps)) that limit experiments primarily to structural imaging [167]. A recently reported 2-photon system uses microelectromechanical systems (MEMS) to enable a higher acquisition rate ( $\approx 40$ fps for  $256 \times 256$  pixels<sup>2</sup>) for calcium imaging of small dendritic trees and spines [62]. Although suitable for functional studies, this system is rather complex to build (mechanically and optically) and requires the use of custom (hardly accessible) dispersion-adapted optical fibers. Miniaturized systems with external MEMS are less complex [66; 65] but require thick fiber bundles that significantly decrease optical resolution and degrade the quality of images. Finally, miniaturised multiphoton systems use lasers that are bulky, expensive, and barely compatible with the development of wireless devices. The use of large-diameter optical probes ( $\varnothing 1.4$  mm) here is also problematic, as it requires tissue ablation above the region of interest prior the implantation of probes in the brain. This can damage the brain, alter neuronal activity, and require multiple series of control experiments [70]. Consequently, there is a lack of minimally invasive, accessible, and miniaturized systems adapted for the functional imaging of fine neuronal processes at different depths in the brain of FBA. To address this issue, we have developed a lightweight miniaturized 1-photon system (mDS1s) with an electrically tunable liquid crystal lens (TLCL) that enables imaging with depth scanning. The optical design of our mDS1s allowed us to identify and image different fine processes in the brain of small animals such as the mouse using minimally invasive ( $\varnothing = 0.5$  mm) optical probes.

## 4.4 Results

### 4.4.1 Key features of mDS1s

During the development of our mDS1s, several key criteria were considered. To design the most accessible and wireless-friendly system possible, we privileged the 1-photon approach over the 2-photon. This method also uses CMOS/CCD sensors that allow functional imaging of neurons at high sampling rates (30-50 fps). To image and to record video from small neuronal structures, we built a high-magnification system (Fig. 4.1) inspired from a recently reported miniaturized 1-photon microscope [168]. The resulting pixel/object ratio ( $\approx 2.9$ ) allowed us to differentiate objects in the order of  $\approx 1$   $\mu$ m (small dendrites, average-size spines [169]) in a  $150 \pm 10$   $\mu$ m field of view (FOV). To further facilitate the imaging of small structures, we built a special gradient index (GRIN) probe assembly with low optical aberrations compared with those of conventional singlet probe (Fig. 4.1) [170]. To image neuronal activity in three dimensions, we developed and integrated a TLCL allowing motionless electrical scan over  $\approx 98$   $\mu$ m depth distance. To reduce tissue damage, our tunable device was coupled (optically) to a minimally invasive, small-diameter ( $\varnothing = 0.5$ mm) GRIN probe assembly (Fig. 4.2d). From a mechanical perspective, we have developed a very compact optical design (Fig. 4.2d) that is integrated into a lightweight mechanical frame, made of solid plastic material. Finally, the epifluorescence design of our system allows us to image and record

calcium activity from fluorescent proteins and calcium indicators such as GCaMPs.

#### 4.4.2 Design of the tunable lens (TLCL)

There are three mechanisms enabling depth scanning: mechanical movements (e.g., by using a step motor), mechanical deformations (e.g., bending an interface between two liquids), and motionless changes of the focal distance  $F$  of the lens by changing the refractive index of a material [92]. Mechanical movements are a well-known approach, but are bulky, heavy, and fragile [133]. Interface bending requires high voltages, provides less focus tuning and is limited in the choice of aperture for the lens. Indeed, the smallest available electrowetting lens (EWL) has a diameter of 1.6 mm. Alternatively, the refractive index change in liquid crystal (LC) materials has none of these limitations (see below for details). These materials are well mastered in the display industry. They exhibit anisotropic properties: light can propagate with different phase delays depending upon the angle between its wave vector  $\mathbf{k}$  and the average molecular orientation (the optical axis) of the LC, often represented by a unit vector  $\mathbf{n}$  (Fig. 4.1a) [89]. Most importantly, we can easily reorient the optical axis  $\mathbf{n}$  by applying very small electric voltages. Hence, we can align LC molecules in a non-uniform way (Fig. 4.1c) to generate a spherical delay in the phase of transmitted light. This will result in electrically variable focusing [121; 109]. The gradual recovery of uniform alignment (Fig. 4.1b) will gradually reduce this focusing effect. The detailed description of fabrication of the TLCL can be found in Method Online and elsewhere [121; 109]. This approach has been successfully introduced previously in a variety of consumer electronic products (e.g., DVD readers, webcams, mobile phones) and some specialized applications [73]. Such lenses have numerous advantages, including low power consumption (micro Watts, thanks to the low driving voltages,  $\approx 3 V_{RMS}$ ), tiny size (0.5 mm thick), light weight (15 mg), and the ability to work with very small clear apertures (CA) and to control the focal distance  $F$  (Fig. 4.1e) by using the voltage or/and frequency of the electrical excitation [109]. A particularly important feature of these lenses is their almost-constant magnification during the electrical scan of depth.

#### 4.4.3 Optical probe

The assembled probe was composed of three optical elements presented in Fig. 4.2e. The first element was a  $45^\circ$  prism (size = 0.5 mm) that facilitated insertion of the probe in the brain and allowed imaging from the side, rather than below where the tissue is usually compressed. The second component of the probe (imaging GRIN) had a high numerical aperture (NA = 0.42, length = 0.6mm) that could maximise the collection of fluorescence. Finally, the third element (GRIN rod lens, NA = 0.2, length = 6.0 mm) could transmit the collected light to the rest of the optical system while maintaining low optical aberrations [170]. This lens is thus well suited for imaging deep brain regions.

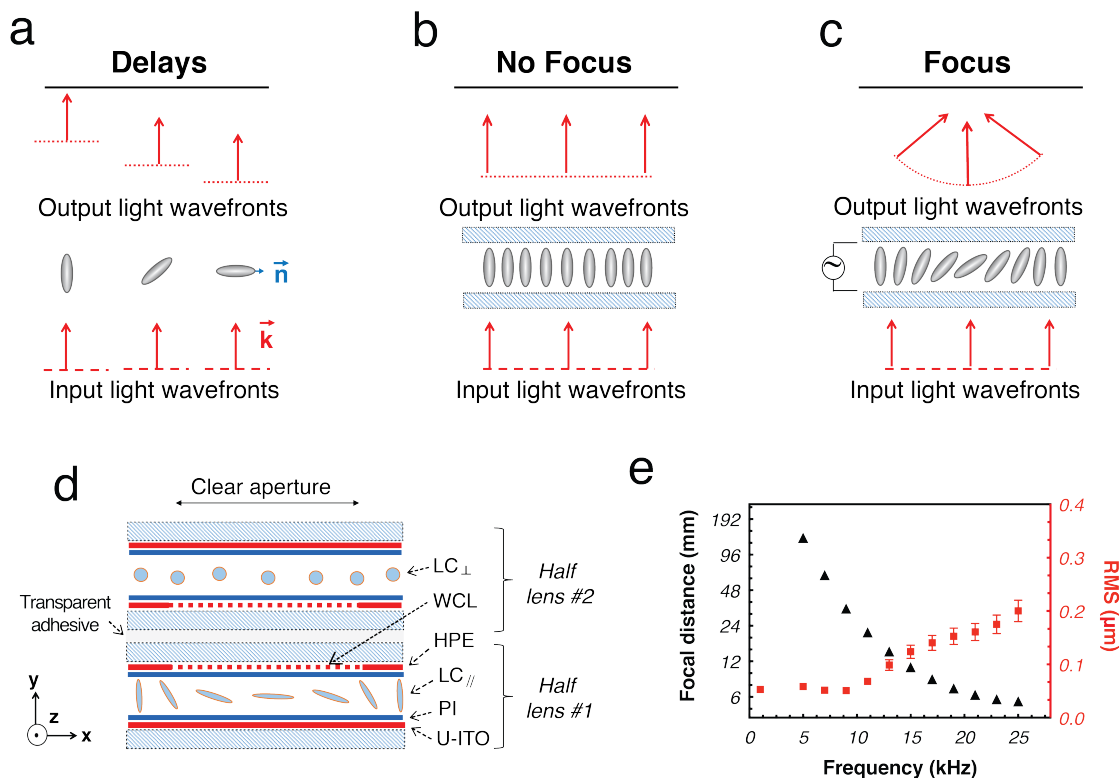
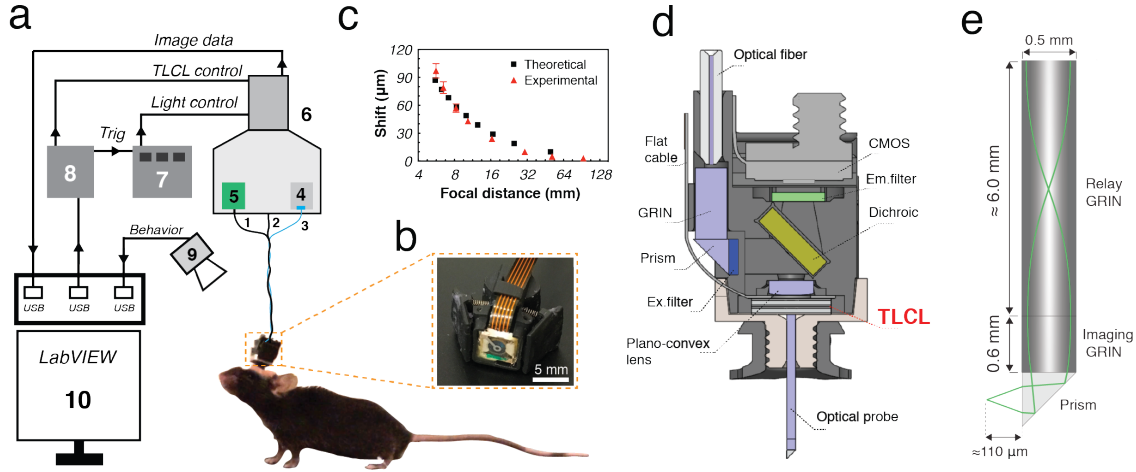


Figure 4.1: **(a-b)** Schematic demonstration of motionless focusing by the reorientation of LC molecules (filled ellipses), **(a)** different phase delays for different angles between the light wavevector  $\mathbf{k}$  and the LC's optical axis  $\mathbf{n}$ , **(b)** uniform molecular orientation generates uniform phase delay; **(c)** non-uniform molecular orientation can generate spherical phase delay and light focusing. **(d)** Schematic demonstration of the structure of the TLCL used (see the main text for details); WCL: weakly conductive layer, PI: polyimide alignment layer, HPE: hole patterned electrode, U-ITO: uniform ITO electrode; **(e)** Control of the focal distance of the TLCL by the frequency of the excitation electrical signal (AC square shaped, at 3  $V_{RMS}$ ) and corresponding RMS aberrations.

#### 4.4.4 Schematics of the system

The integration of the TLCL required specific modifications of mechanical and electrical hardware of the originally developed micro-endoscope system [168], (Fig. 4.2a). First, to drive the TLCL, two additional wires (Fig. 4.2a, 2) were conducted from the microendoscope to the custom rotary joint system (Fig. 4.2a, 6). Second, to generate a reliable AC signal in working frequency range (1-30 kHz), a data acquisition system (Fig. 4.2a, 8) with high sampling rate (up to 900 kS/s) was chosen. Finally, LabView software was adapted for dynamic control of the TLCL and triggering of 4,5,9 (Fig. 4.2a) for time-lapse imaging over long periods of time.



**Figure 4.2: Schematic presentation of the ensemble of the imaging system.** (a) Schematic of the system: 1. Extension cable for the CMOS; 2. TLCL's wires; 3. Optical fiber; 4. Light source; 5. DAQ<sub>CMOS</sub>; 6. Rotary joint system; 7. LED driver; 8. DAQ<sub>LabVIEW</sub>; 9. Camera for behavior; 10. LabView user interface. (b) Photo of the mDS1s exposing the TLCL. (c) Electrical focal shift of the mDS1s simulated using Zemax optical software. 1 μm fluorescent beads (immersed in water,  $n \approx 1.33$ ) were used for the experimental measurements. Error bars correspond to the standard deviation. (d) Schematic representation of optical components. Light from the optical fiber is first collimated by a large-diameter GRIN lens and then reflected by the 45° prism. The excitation filter is used to preserve the desired wavelengths and the dichroic mirror to reflect light into the plano-convex lens, towards the TLCL. Excitation light is then guided within the optical probe assembly to finally reach the object/structure of interest. The emission (fluorescent) light passes back through the probe to reach first the TLCL, then the plano-convex lens. The latter focalizes the image on the CMOS sensor passing beforehand through the dichroic mirror and the emission filter. (e) Schematic side view of the optical probe with 3 components: 45° prism, imaging (NA = 0.42) and rod GRIN (NA = 0.2) lenses.

#### 4.4.5 Optical characterisation of the assembly.

Before assembling the micro-endoscope, we characterized the optical performance of TLCL. A low voltage square-shaped AC signal was used to change the focal distance (online Methods) (Fig. 4.2c). At the maximal operational capacity of the TLCL (Fig. 4.2c), a minimal focal distance of 5.6 mm was reached along with a very low (0.2 μm) level of root mean square (RMS) aberrations (Fig. 4.2c). The experimentally obtained characteristics of the TLCL (Fig. 4.2c) were used in Zemax optical studio software to simulate the focal adjustment capability of final mDS1s. The experimental focal shift of the assembly was measured (online Methods) using fluorescence microspheres ( $\phi \approx 1.0 \mu\text{m}$ ) mounted with a thin ( $\approx 4 \mu\text{m}$ ) cover glass that provided the ability to scan through the entire working distance of the probe ( $\approx 110 \mu\text{m}$ ). The experimental results agreed with the theoretical predictions (Fig. 4.2c). We then characterized the changes in optical resolution during electrical modulation of the working distance of the final assembly (Fig. 4.2d). The experimental results show (Fig. 4.3a) a slight

change of resolution (lateral: from 1.2  $\mu\text{m}$  to 1.5  $\mu\text{m}$ ; axial: from 13  $\mu\text{m}$  to 18  $\mu\text{m}$ ) due to an increase in optical aberrations (Fig. 4.1e) and light scattering by the TLCL. Average values of lateral and axial resolutions are, respectively,  $1.4 \pm 0.1 \mu\text{m}$  and  $15 \pm 2 \mu\text{m}$ . Intensity profiles (Fig. 4.3e) show that the same structures could be clearly identified through the entire range of the focal shift. Similarly, we found minimal changes in magnification that varied from 8.9 to 8.6 (the average magnification is  $8.7 \pm 0.2$ , Fig. 4.3b).

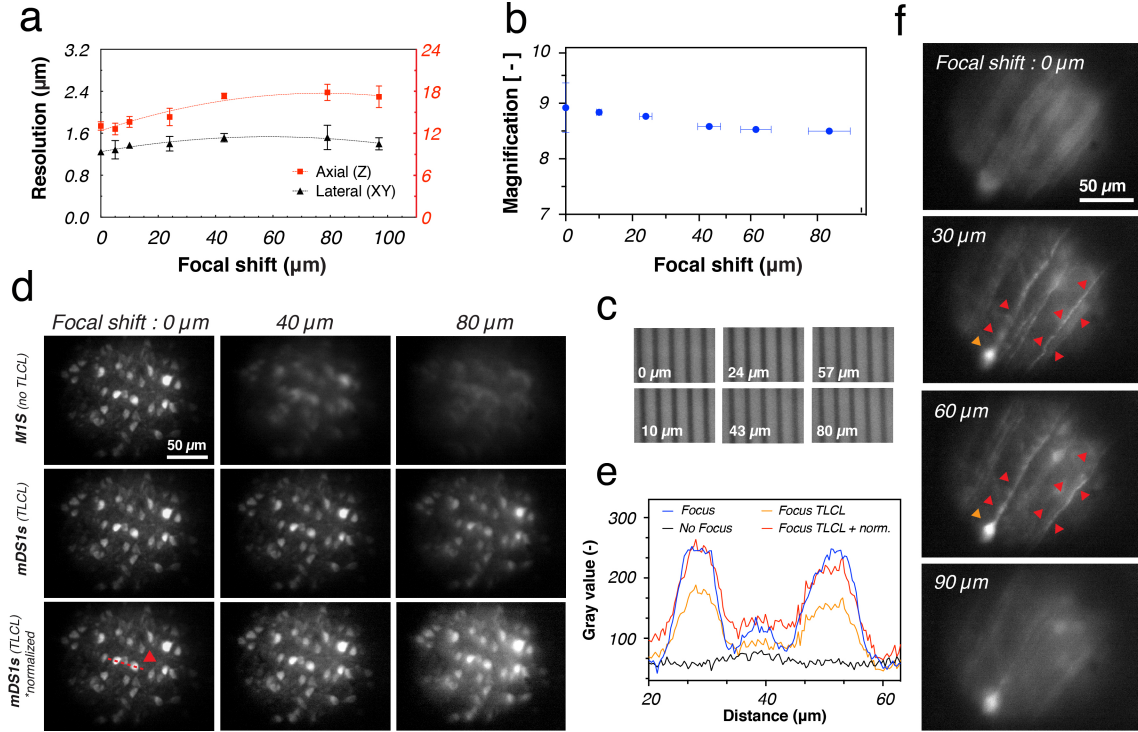


**Figure 4.3: Electrical focal shift and characterisation of optical parameters of the mDS1s.** (a) Resolution and (b) magnification during electrical focal shift. Error bars correspond to the standard deviation. (c) Focused images of a scale bar sample at different shift values of the TLCL (spacing between the lines = 10  $\mu\text{m}$ ). (d) *In vitro* depth imaging of neurons (soma and dendrites) from the motor cortex of C57B16 animal expressing GCaMP6s (viral injection). The thickness of slice is  $100 \pm 10 \mu\text{m}$ . The out-focused position was simulated by the mechanical displacements: 0  $\mu\text{m}$ , 40  $\mu\text{m}$  and 80  $\mu\text{m}$  (indicated on the top of each image). The 1<sup>st</sup> row presents mechanically out-focused images taken with a fixed focal plane while in the 2<sup>nd</sup> row images were taken with the mDS1s that enabled electrical compensation of the mechanical displacement. The 3<sup>rd</sup> row presents intensity normalization (of the 2<sup>nd</sup> row) based on the fluorescence level of the central neuron (indicated with red arrow). (e) Intensity profile through the dotted line of interest in d (3<sup>rd</sup> row, low-left corner) for the 80  $\mu\text{m}$  focal shift. (f) The electrical scan shows various neuronal structures at different depths (indicated in the top left) within the *in vitro* slices presented in a.

Having confirmed that our mDS1s is suitable for adaptive (electrical) focus tuning, we then imaged different brain structures *in vitro*. As demonstrated in Fig. 4.3f, the electrical scan made with the TLCL allowed us to image through different layers of fixed tissue prepara-



tions. The blurry sections within the first (shift = 0  $\mu\text{m}$ ) and last (shift = 90  $\mu\text{m}$ ) images were brought back into focus (shift = 30  $\mu\text{m}$  and 60  $\mu\text{m}$ ) to clearly show the presence of various dendritic structures (Fig. 4.3f).

#### 4.4.6 Imaging of dendrite and spine activity in FBA.

Furthermore, we also show that our system can be used for *in vivo* time-lapse imaging of calcium transients in small neuronal processes. Using the TLCL, we adjusted the position of the focal plane at the optimal imaging depth ( $\approx 30 \mu\text{m}$  focal shift) where multiple fine neuronal processes are in focus. We then recorded calcium activity (Supplementary Video 1) while the animal was exploring the new cage area (Fig. 4.4a,b). Data were then analyzed to investigate the link between the activation patterns of different neuronal structures (Fig. 4.4b). The  $\text{Ca}^{2+}$  traces of a few neurons (Fig. 4.4b, ROIs: 12, 23, 31) showed a very low correlation (Fig. 4.4d) with the rest of the structures, suggesting that these might be a specific population of cells with different activation patterns. Imaging of finer structures (Fig. 4.4c) revealed high correlation between the activities of dendritic branches **B2** and **B1** (Fig. 4.4d), suggesting that they belong to the same neuron (Fig. 4.4d, ROI: 1). However, the activity of near-passing branch **B3** (morphologically similarity to **B2**) had a higher correlation with **B4** rather than **B1**. Thus, the analyses of calcium traces (Fig. 4.4c) allowed us to link the activation patterns of different fine neuronal structures (Fig. 4.4d), in addition to documenting their structural profiles (Fig. 4.4e).

We then correlated the calcium dynamics of various neuronal structures to the behavioural activity of the animal (Fig. 4.4f). As shown in Fig. 4.4f-h, the level of calcium activity within the entire FOV was constant and equal to the baseline in the animal at rest (Fig. 4.4h). However, the level of calcium activity was modulated in different neurons and their respective fine processes according to the motor activity while the animal was walking or grooming (Fig. 4.4g).

Having confirmed that our system can be used for imaging and characterizing fine neuronal processes during different behavioural tasks, we proceeded to the demonstration of the critical advantages enabled by electrical depth scanning (Fig. 4.5). As shown in Fig. 4.5a, electrical adjustment (55  $\mu\text{m}$ ) of the depth position revealed new neuronal features, undetectable at the original working distance of the probe (Fig. 4.5a, top). For instance, within ROI #21 we have discovered a fine dendritic branch (Fig. 4.5a-b, red arrows) that was connected to the pair of newly revealed neurons (orange arrows). A continuation of neuronal prolongation within ROI #2 was also identified (Fig. 4.5c) and quantified (Fig. 4.5d). Thus, the electrical shift allowed a better visualization of the neuronal network by enabling the detection of new structures and connections.

Finally, we have also demonstrated the capacity of our mDS1s to electrically focus on even

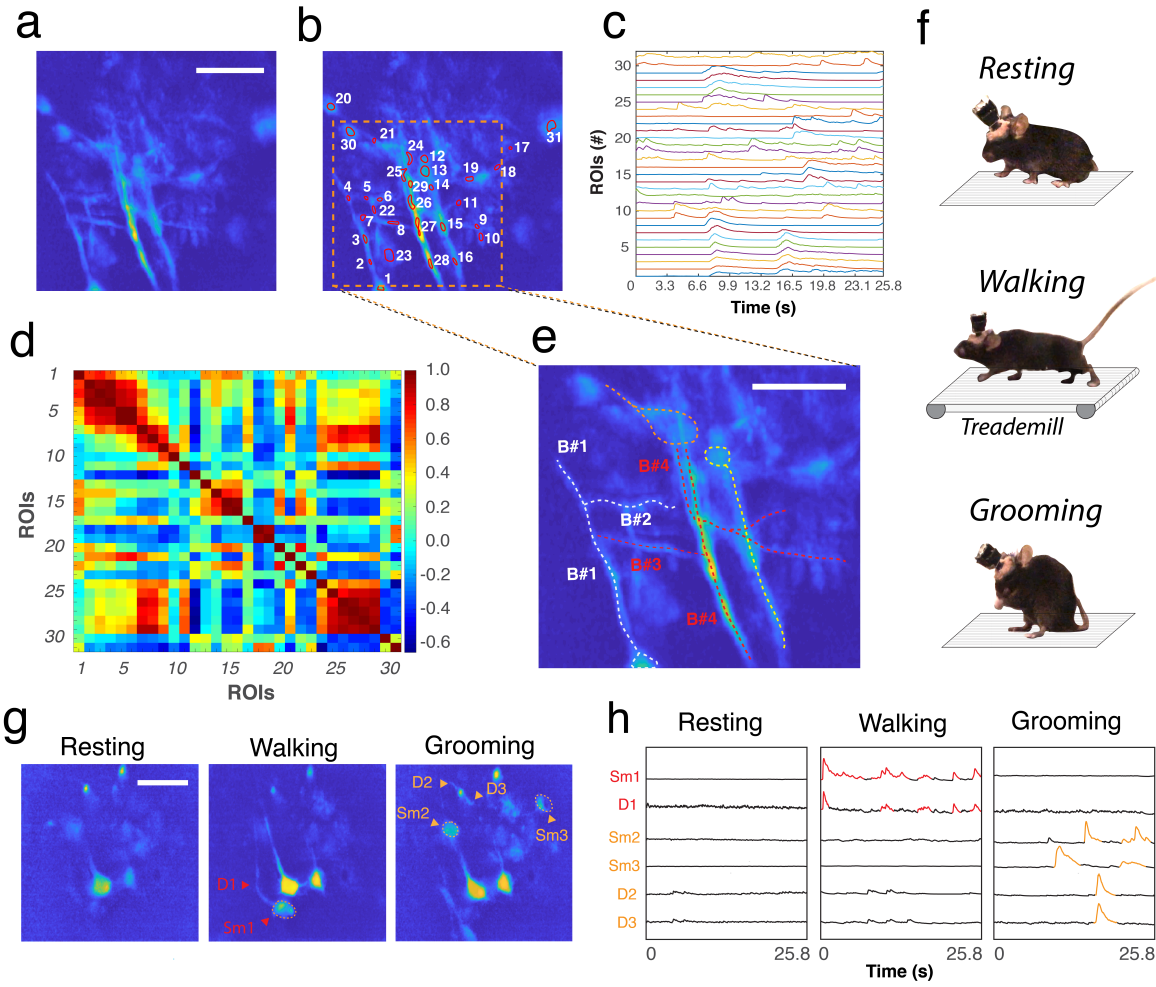


**Figure 4.4: Time-lapse imaging of  $\text{Ca}^{2+}$  activity from GCaMP6s-labeled neurons of the motor cortex.** (a-d) Neuronal enhanced calcium activation image (a), manually selected ROIs (b), calcium traces (c) and correlation map (d) from the recorded neuronal activity (**Supplementary Video 1**). Red and dark-blue colors stand for the maximal (1) and minimal correlation values (-0.6). (e) Structural reconstruction based on d. Each dendritic branch (B) corresponds to multiple ROIs in b; B1: 2,3,4; B2: 5,6; B3: 7,8; B4: 24-29. (f) Neuronal activity was imaged and analysed during three behaviours of the animal: resting, walking and grooming. The treadmill was used to encourage the walking comportment while for the remaining conditions, the natural behaviour of the animal was recorded. (g,h) Neuronal enhanced calcium activation image (g) and  $\text{Ca}^{2+}$  traces (h) from somas (Sm) and dendrites (D) during the behaviour in (f). Scale bars = 50  $\mu\text{m}$ . Miniscope 1-photon-based calcium imaging extraction signal pipeline (MINIPIPE) and MATLAB were used to analyze the data.

smaller neuronal processes, such as dendritic spines, while examining rhythmic head movements (Fig. 4.5j). The images obtained at the original working distance of the GRIN probe contained only blurry neuronal structures (Fig. 4.5e); electrical adjustment of the working distance ( $\approx 60 \mu\text{m}$ ) made it possible to clearly identify the soma, dendritic processes, and (Fig. 4.5f) suggesting dendritic spines [171]. Furthermore, time-lapse imaging (Fig. 4.5h)



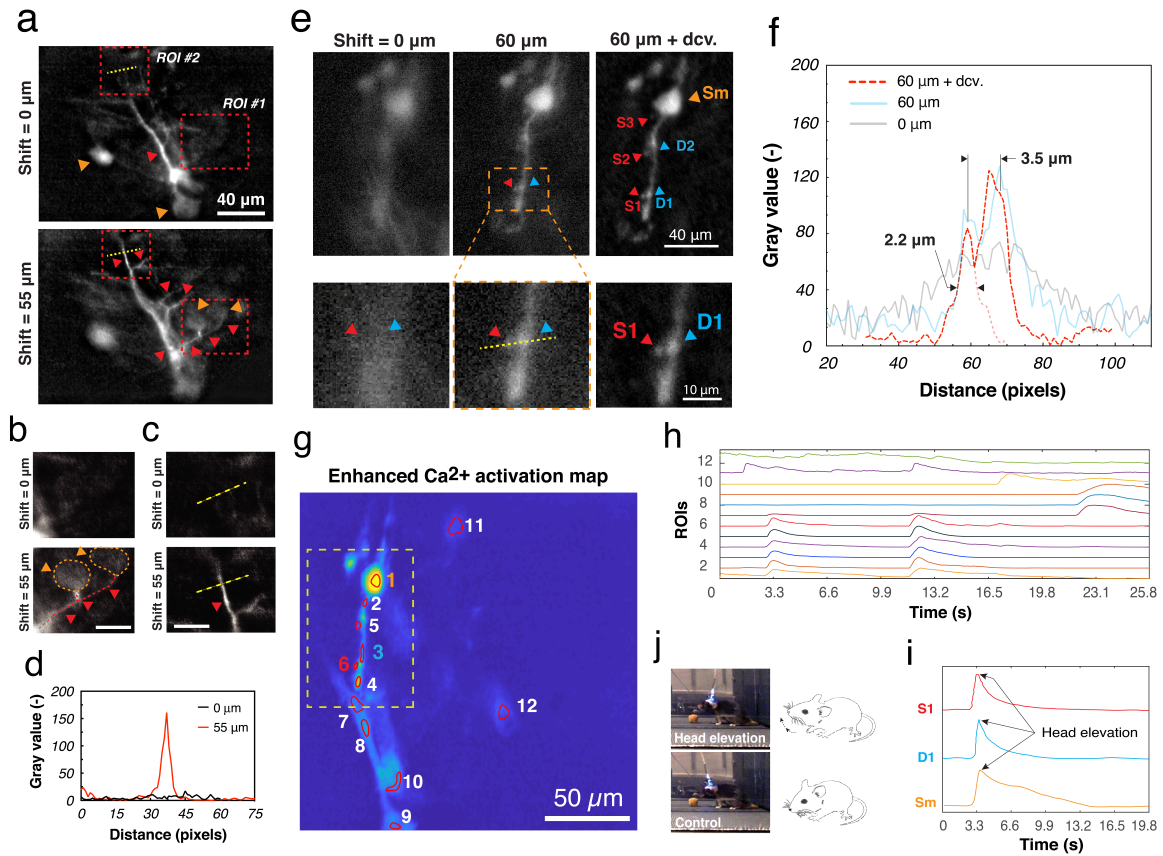


**Figure 4.5: Electrical focus adjustment and time-lapse imaging of  $\text{Ca}^{2+}$  activity from GCaMP6s-labeled neuronal structures in the motor cortex of a freely behaving animal.** (a) Images of neuronal activation at different, electrically adjusted focal depths. Focused structures are indicated with arrows (orange: soma, red: processes). (b-d) Cropped images (b,c) of ROIs #1, #2 and intensity profile (d) through the dotted yellow line in c. Scale bars = 15  $\mu\text{m}$ . (e) Calcium activation images of the soma (Sm), dendrites (D) and spines (S) at two different depths : 0  $\mu\text{m}$  and 60  $\mu\text{m}$  (indicated on the top). Last column image was processed with the Lucy-Richardson deconvolution algorithm (iteration = 15) using Deconvolution-Lab2 plug-in (ImageJ). (f) Intensity profile through the yellow line in e. The diameter of S1 is  $\approx 2.2 \mu\text{m}$  and the distance between S1 and D1 is  $\approx 3.5 \mu\text{m}$ . (g,h) Enhanced calcium activation image (MIN1PIPE) with manually selected ROIs (g) and the corresponding  $\text{Ca}^{2+}$  traces (h). Image plane was focalized using the TLCL (60  $\mu\text{m}$ ). (i,j) The head movement (j) of the animal was correlated (i) to the activity of electrically focused neuronal structures in g.

showed the capacity of our system to differentiate  $\text{Ca}^{2+}$  dynamics in presumably dendritic spines from their parental dendritic branches and soma (Fig. 4.5g), which were highly correlated with head movements (Fig. 4.5j, I).

## 4.5 Discussion

In this study, we have presented a depth scanning 1-photon miniature microscope system (mD1S) that allows multi-plane imaging of neurons and their fine processes, including dendrites and dendritic spines, in freely moving animals. Three fundamental limitations have been successfully addressed. First, we have developed and incorporated a novel tunable lens (the TLCL) that enabled  $\approx 100\ \mu\text{m}$  electrical modulation of the imaging plane within our mD1S. The utility of this novel feature was shown by imaging neurons (Fig. 4.3e) and fine processes (Fig. 4.5) that were undetectable in unfocused positions (Fig. 4.5). Electrical modulation also improved the efficiency of surgical procedures by drastically reducing the rate of animal sacrifice due to an incorrect installation depth of the probe. Compared with commonly used EWL [66; 65], our tunable lens (TLCL) has a 9-times higher optical power (180 diopters) that enables direct optical coupling with small-diameter GRIN probe assemblies (Fig. 4.2d). This makes it possible to achieve a compact optical design (Fig. 4.2) and adaptive imaging with constant magnification ( $8.7 \pm 0.2$ ) during the entire tunability range. TLCL also has  $\approx 20$  times lower operation voltages ( $3\ \text{V}_{\text{RMS}}$ ) and  $\approx 100$ -times lower power consumption ( $\approx \mu\text{W}$ ) compared with EWL and is, therefore, better suited for its integration within future wireless devices. From a mechanical perspective, the small size ( $5\text{mm} \times 5\text{mm} \times 0.8\text{mm}$ ) and the low weight ( $\approx 0.1\text{g}$ ) of the TLCL are an excellent fit for many miniaturized applications in neuroimaging.

Second, our device shows a high spatial resolution within a 1-photon system capable of imaging fine neuronal processes. To achieve this result, we have designed our device with high magnification [168] along with low optical aberrations (online Methods). Using our mD1S, we have been able to image, record, and correlate the ( $\text{Ca}^{2+}$ ) activity of fine neuronal features (e.g., dendrites and dendritic spines) with different behaviors (e.g., grooming, walking, head movements) in freely behaving animals. We think that our *in vivo* results will broaden the experimental repertoire of miniaturized 1-photon systems (so far limited to the imaging of large neuronal structures [52; 51; 49; 47], e.g., soma) to the imaging of fine neuronal processes (e.g., dendrites, dendritic spines), wherein all neuronal communication occurs. Third, the developed mD1S is also addressing the size and weight limitations of existing depth-scanning devices [66; 62; 65] that can affect the animal's head movement, navigation and multiple decision-making choices. Indeed, to improve animals' condition and to preserve their natural behavior, we have developed one of the lightest ( $\approx 1.4\ \text{g}$ ) and smallest ( $10\text{mm} \times 17\text{mm} \times 12\text{mm}$ ) mD1S systems reported so far [47]. The compact optical design (Fig. 4.2d) and the choice of mechanical frame materials were the key parameters allowing us to achieve this result (online Methods). We think that our mD1S will provide benefits to the animal and improve the quality of behavioral data in many investigations (e.g., memory, cognition, etc.) based on the natural movement (head and body) of animals.

To summarize, we think that the advantageous mechanical and optical characteristics of our

mD1S can enable new investigations of fine neuronal structures in physically limited subjects (e.g., younger, older, injured, etc.) that cannot carry currently available heavier devices. Among these subjects are smaller (younger) subjects that are usually used to study neurogenesis. For instance, our device can be used to study the formation of dendritic branches and spines within adult-born neuroblasts that have finished their migration and are actively integrating the existing neuronal networks [58]. Older mice that are physically weaker can also benefit from our lightweight device, as one could study the changes in spine density occurring during normal aging [161] and neurodegenerative pathologies [159; 160]. Finally, our mD1S might allow us to assess functional and structural changes in animal models of neurotraumatic injury [172], such as spinal cord injury or stroke.

In the near future, certain improvements could optimize the functionality of our mD1S. First, a 4-layer stacked [77] design of TLCL can be considered for reducing optical aberrations and light scattering (Fig. 4.1) during adaptive imaging (Fig. 4.3). Increasing the NA of the probe will improve the lateral and axial resolution of the system, allowing better imaging of fine neuronal processes. The FOV can be further increased by modifying the design of the mD1S or by using larger diameter GRIN probes. Finally, the development of 2-color, optogenetics-synchronized and wireless of our mD1S should be considered. The low voltage and power requirements of the TLCL will significantly facilitate the engineering of such devices.

## 4.6 Appendix

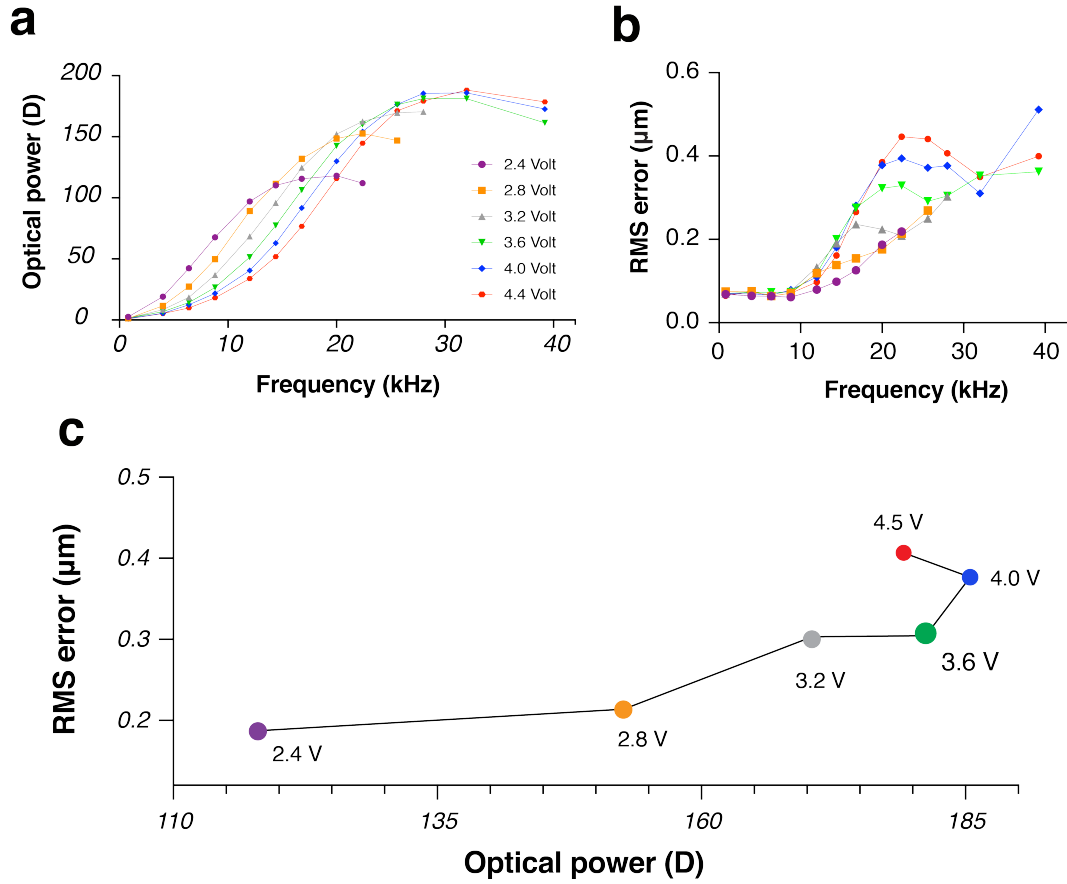


Figure 4.6: **Characterization of the TLCL.** (a,b) Optical power (a) and aberrations (b) increase proportionally to the driven frequency of the AC square signal applied to the TLCL. The amplitude of the voltage varied from 2.4 V to 4.4 V. (c) RMS aberrations at the maximal optical powers for each of the driven voltages. The optimal voltage: 3.6 V. Voltages below that value generated lower optical powers while the higher voltages, had higher RMS error.

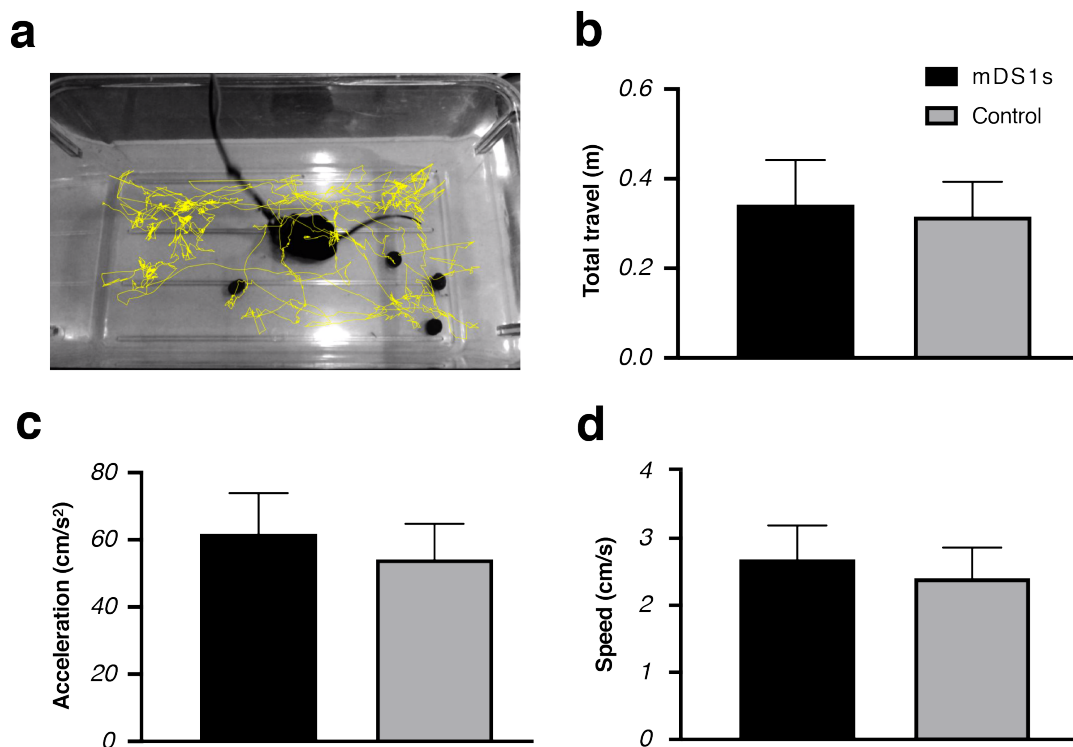


Figure 4.7: **Portability test of the mDS1s.** (a) Displacement path of the animal during portability test ( $\approx 4$  min). AnimalTracker plug-in (ImageJ) was used to track and analyze animal's movement. (b-d) The total travel (b), the average moving speed (c) and acceleration (d) of the animal with and without mDS1s. Error bars correspond to the standard deviation.

## Online Methods

**Design of the TLCL.** We start by building what is called a “half lens 1” sandwich (presented in the bottom of Fig. 4.1d), by using two glass substrates ( $100\ \mu\text{m}$  thick). One of the substrates contains a weakly conductive layer (WCL) and a hole patterned electrode (HPE), the combination of both being used to shape in space the electric field and the corresponding alignment of LC molecules. The second substrate is covered by a uniform transparent electrode (indium tin oxide), U-ITO. Homemade nematic LC (NLC) material (presented as filled ellipses) is then filled into the sandwich and aligned (in the plane  $x,y$ ) almost parallel to substrates by using thin rubbed films of polyimide (PI) on both substrates. This sandwich can be used to focus light with polarization in the  $x$  and  $y$  plane. Given the non-polarized nature of fluorescence light, a second similar sandwich is then fabricated (see “half lens 2”, top of Fig.1d) and attached to the first one via a transparent adhesive after rotating it on 90 degrees around the  $y$  axis. NLC molecules of the half lens 2 are thus in the  $y$  and  $z$  plane and this final assembly can now focus un-polarised light.

**Characterisation of the TLCL.** We used a commercial wave-front sensor (WFS150-7AR;

Thorlabs) to measure the focal distance and the optical aberrations of the TLCL (Fig.4.1e). An electrical square-shaped AC signal was used to activate and drive the lens. Voltage was fixed at optimized value of  $V_{RMS} = 3.6$  V while the frequency of the AC signal was tuned from 1 kHz up to 25 kHz to electrically adjust the optical power (inversely proportional to the focal distance  $F$ ) of the lens.

**Focal shift measurements.** Fluorescent beads (FSEG004; Bangs Laboratories, Inc.) were immersed into water and mounted between a standard microscope slide and a thin (4  $\mu$ m) cover glass. Beads were first mechanically defocused using a motorized actuator and then electrically brought back into the focus using the TLCL. The precisely known mechanically out-of-focused distance corresponded to the compensatory electrical shift produced by the TLCL.

**Resolution and PSF measurements.** TLCL was used to electrically modulate the working distance of the probe. For each shift value, fluorescent beads were mechanically scanned by steps of 3  $\mu$ m to generate a 3D point spread function (PSF) stack. The resolution of the system (for each shift value) was determined by using the MetroloJ plug-in (ImageJ) that measured the full width at half maximum (FWHM) of the experimental PSF.

**Animals.** All animal experiments were approved by the Animal Welfare Committee of CHU de Québec and Université Laval in accordance with the Canadian Council on Animal Care policy. We used 2-month old male or female VGluT2-IRES-Cre transgenic mice (The Jackson Laboratory, RRID: IMSR JAX:016963). All mice were either housed alone or with a single sibling after the surgery.

**Surgery.** Aseptic surgery was performed under isoflurane anesthesia (1-2 %). All pressure points and incision sites were injected subcutaneously with lidocaine-bupivacaine (7.5 mg/kg) for local analgesia. Slow-released buprenorphin (1 mg/kg) was administered subcutaneously for post-surgical analgesia. The skull was exposed to do a craniotomy (about 1 mm in diameter) above the motor cortex. The dura mater was removed prior to viral injection. A glass micropipette (ID 0.53 mm, OD, 1.19 mm, WPI) mounted on a nano-injector (Nanoliter 2010 injector with SMARTouch controller, WPI) was filled with AAV2.9/em-CAG-Flex-GCaMP6s (titer  $1.2 \times 10^{13}$  GC/mL) and inserted into the motor cortex to deliver 70 to 100 nL in 2-4 locations within the following stereotaxic coordinates: anteroposterior -0.3 to 0.3 mm from Bregma, lateral 0.8 to 1 mm, depth 0.8 mm. The flow rate was 30 nL/min and after completion, the micropipette was held in place for at least 2 min to prevent leakage. The craniotomy was filled with a hemostat (Bonewax) and the skin above the skull sutured. After a waiting time of at least 3 weeks was allowed a robust expression of the GCaMP6s, mice were instrumented with a GRIN lens during a second aseptic surgery. The implant was secured with self-tapping bone screws (cat 19010-10, FST), crazy glue (exact type) and dental cement (cat 525000, A-M Systems). Mice were allowed to recover for a least a week before

chronic experiments.

**Portability test.** To carefully connect the miniscope, animals were anesthetized with isoflurane (2 %). Mice were first habituated to the headpiece fixation for 3 days, 30 min per day. Portability test consisted of 4 imaging session spread over two weeks period.

**Data acquisition.** At the beginning of each imaging session, headpiece fixation was followed by a resting period of 5 minutes. During each imaging session, the movement of the animal was recorded for 42 minutes at 30 frames-per-second. Imaging session was initiated from software. Mice were allowed to roam free in an open field during imaging without direct contact with the experimenter. Calcium activity in the motor cortex neurons was monitored while recovering from anesthesia, during spontaneous activity such as grooming and during treadmill locomotion.

**Data analysis.** Images were analysed using MATLAB and ImageJ. In MATLAB, we used Miniscope 1-Photon Based Calcium Imaging Signal Extraction Pipeline (Min1pipe). The image processing with MIN1PIPE involved motion correction (if required), manual ROI selection and calcium signal extraction. Correlation matrixes were done in MATLAB. ImageJ was used for background subtraction and brightness adjustment. DeconvolutionLab2 plugin was used for the deconvolution based on the experimental PSF stacks.

## Supplementary Materials

Supplementary materials are available in the online version of the paper.

## Acknowledgement

We would like to thank LensVector inc. for its material and financial support of this work and Dr. Maxime Lemieux for his scientific advice. A.B. and L.T. are supported by Fonds de recherche du Québec - Nature et technologies (FRQNT) and Natural Sciences and Engineering Research Council of Canada (NSERC) fellowships. T.G. is supported by the Canada Research Chair in Liquid Crystals and Behavioral Biophotonics and F.B. by a Fonds de Recherche du Québec en Santé (FRQS) scholarship. The research was supported by FRQNT and NSERC (#05888) grants to T.G. and an NSERC (#06218) grant to F.B.

## Author Contributions

A.B. conceived, designed, built and characterized the system under the supervision of T.G.; A.B., L.T., A.R., and N.K. performed surgery, experiments, and kinematic analysis under the supervision of F.B.; A.B. analyzed the data; A.B., T.G., and F.B. wrote the paper. All authors participated in discussion and data interpretation.



# Conclusion

## 5.1 Summary

When we have started this work, it was clear for us that the field of neuroscience needs miniature optical systems allowing to image the brain of freely behaving animals. The major requirement for these tools is their capability to record and to synchronize the activity of different brain structures (neurons, glial cells, dendrites, etc.) to the behavior of animals.

The first miniature device for neuroscience applications was based on the 1-photon imaging approach [47]. Although several commercial (Inscopix, Doric [57; 56]) and open-source (UCLA's miniscope [49]) versions of such systems have been developed, they still have important limitations regarding their mechanical, electrical and optical aspects. A major issue is the lack of depth scanning ability that drastically reduces the efficiency of the surgical procedures (decreases chances of finding structures of interest due to the non optimal insertion depth) and also impacts the quality of neuronal recordings that are usually taken in the out-of-focused positions [55]. Unfortunately, the obvious mechanical solution (conventional actuators) is hardly possible due to the severe weight criteria imposed by the physical capacity of small animals (unable to carry more than 2-2.5 g) [28; 46]. Thus, there is a lack of electrically tunable device enabling depth scanning.

Because of these optical limitations, some researchers have even changed animal models preferring the rat (much larger and psychically stronger) to the mice [173]. This change has supported the engineering efforts allowing the development of larger tools with more optical options [174; 175]. However, on a biological level, the imaging of mice is more appealing for many reasons [176]. Mice are the most studied and most documented rodents. The variety of the genetically modified subjects is also greater in mice compared to rats. Also, from a practical perspective, mice require less infrastructure/space (to keep animals) and are less expensive and easier to maintain. For all these reasons, the mouse model remains the most popular choice for the study of the brain [176]. Thus, an efficient lightweight imaging approach for small animals, such as mice, is required.

Miniaturized 1-photon microscopes were often reported as cellular imaging devices adapted for the study of large structures [50; 49; 51; 52]. The necessity to image more cells has further



pushed the development (optimization) of these systems in the direction of a large field of views and small magnifications. With such optical parameters, miniature 1-photon devices have solidly anchored/centred their application area to the imaging of large cell bodies (e.g., neurons,  $\approx 10\text{-}50\text{ }\mu\text{m}$  in diameter) [46; 48].

However, as it is well known, brain also has multiple fine structures [177; 178]. In fact, each neuron perceives and communicates the information by means of numerous fine extensions, called dendrites and axons ( $\approx 1\text{-}3\text{ }\mu\text{m}$  in diameter). It's possible to compare these extensions to electrical cables that transmit electro-chemical signals over long distances. Additionally, brain contains even smaller structures, the spines ( $\approx 0.2\text{-}1\text{ }\mu\text{m}$ ) [179]. Latter are located on dendrites ("input" cables) and serve as connectors to the "out-put" cables (axons) of other neurons. To give an idea, each neuron (from 80-100 billion in the brain) can have up to 10 thousand communicating neurons and up to 20,000 spines [177; 178]. It's important to mention that the imaging of such fine structures is also very important for the understanding of the brain.

As mentioned previously, the optical design of original (existing before our work) miniature 1-photon devices didn't allow adequate imaging of these fine structures. Thus, in the last decade, miniature laser scanning systems (adapted for the subcellular imaging) have been developed [60; 61; 62; 63; 64; 65]. Even-though these systems have demonstrated the capacity to image dendrites, axons, etc., they have also demonstrated numerous limitations concerning their weight, complexity (optical and engineering), accessibility, etc. that were worse, compared to the 1-photon approach. Furthermore, the depth imaging issue also persists in this category of high-resolution miniaturized devices.

In the framework of this thesis, we have developed a 1-photon miniature device with an LC lens that allows to solve this fundamental depth scanning limitation. In addition, the choice of low aberrations optical GRIN probes [170; 54] and the high magnifications of our system allowed to visualize fine neuronal structures [53]. The presence of the LC lens has an added value here as these small/fine neuronal features (dendrites, axons, etc.) are particularly hard to detect in the absence of the perfect focus. **Chapter 1** presents the development of our small diameter (0.5-0.55 mm) LC lens [77]. Physical characteristics (weight  $\approx 0.1\text{ g}$ , size  $\approx 5\text{ mm} \times 5\text{ mm}$ ) of the developed lens allowed an easy integration within a miniaturized imaging device. From the optical perspective, our lens demonstrates high optical power ( $\approx 180\text{-}360\text{ dpt}$ ) and allows direct coupling with standard GRIN rods lenses (commonly used in neuroimaging applications [54]). The design, assembling and characterisation of a single and also double LC was done in our work. We also have shown how to control and to reduce RMS aberrations (in general and the coma aberration in particular) by the cell stacking approach [77]. Finally, we have improved the image quality by reducing the polarization mismatch and by choosing the appropriate stacking sequence and driving parameters of the LC lens [77; 92].

**Chapter 2** presents our macroscopic imaging system with the first generation of our tunable LC assembly [73]. Latter is composed of two standard GRIN rod lenses (imaging and transmitting [54]) and a TLCL that allows to electrically modulate the focus. In this study, we first presented the design, assembling and characterisation of the TLCL. The proposed custom stacked design enabled polarisation independent imaging [77; 92] that maximised light collection and decreased excitation light intensity. The performance of the final imaging system (with TLCL) was then demonstrated by scanning a  $74 \pm 3 \mu\text{m}$  depth distance in the brain of anaesthetized subjects. The *in vivo* utility of the device was confirmed by unveiling multiple neurons at various (electrically adjustable) depths of the cortex. With the same experiment, we have also confirmed that the standard optical RMS aberrations ( $\approx 0.2 \mu\text{m}$ ) of the TLCLs (in general) are sufficiently low to maintain a good image quality during the entire range of the focal shift.

**Chapter 3** presents the development of fixed-focal-plane 2D miniaturized imaging device that has numerous advantages compared to the previously existing systems [49; 56; 57]. From a mechanical perspective, the proposed device has small dimensions (10 mm x 17 mm x 12 mm) and weighs only 1.3 g ( $\approx 30\%$  improvement). From the optical point of view, the high magnification design allows to observe fine structures of the neuronal circuitry [178; 179]. To more-over accentuate the ability to image small features (e.g., dendrites, axons and even spines) we have used a low aberration GRIN rod design that allows to obtain the high image quality [54]. We have performed all stages of the development : design, assembling and characterisation of the miniaturized microscope. The resolution of the device was then characterized by imaging water immersed micro-spheres (diameter  $\approx 1 \mu\text{m}$ ). Finally, we have used fixed brain tissue preparations (marked with the calcium indicator GCaMP6s [23]) to show the recording of *in vitro* proof-of-concept images (and quantification) of dendrites and spines.

**Chapter 4** presents the final miniaturized imaging device with an integrated TLCL [submitted]. We first started by presenting the design, assembling of the tunable element. Then, by using a Shack-Hartmann wave-front analyser we have characterised the optical performance (optical power and aberrations) of the lens and have theoretically calculated it's tunability potential within the future miniaturised assembly. We have then integrated the TLCL into the miniaturized device developed in the chapter 3. The size of the resulting depth scanning device remained identical to the 2D variant while the weight has only increased by 0.2 g. The optical performance was characterized by measuring the resolution and the focal shift ( $\approx 98 \mu\text{m}$ ) capacity by using water immersed micro-spheres (diameter =  $1 \mu\text{m}$ ). Then we have shown our first *in vivo* results by recording the calcium activity from fine neuronal structures during different behaviours (resting, walking, grooming) of the animal. The utility of the TLCL was demonstrated by comparing calcium activity recording from an electrically adjusted image plane versus a standard, fixed-focal-plane images. Our results have shown

that the electrical adjustment allows to detect and to record from dendrites and spines that were imperceptible in the absence of focal adjustment. **Thus, we have confirmed the target novel optical features (electrical scan with TLCL, visualization of fine structure) in the developed miniaturized 1-photon device.**

## 5.2 Conclusions

The developed device can be used to study multiple biological problems in the brain of freely moving subjects [28; 46]. The ability to image fine neuronal structures and the capability of electrical adjustment of the focal plane are major advantages when it comes to the study of dendrites, axons and spines in the brain small animals [62; 66].

The low weight and size of our device will allow to conduct studies related to the neurogenesis, in younger (smaller) animals. For instance, the formation of fine structures in the developing brain of younger subjects can be studied [163]. This kind of investigation is hardly possible using the existing devices that are too heavy to be carried by these animals. The study of neuronal migration is another good example [180]. Indeed, it's well known that adolescent mice are a better model for this kind of studies due to the high levels of cell migration compared to adult mice [181]. Within the same young subjects, many investigations related to the neurogenesis (cell division, migration, integration within the existing neuronal network) can be considered [58]. Our device can also be used in older mice that, similar to previous subjects, can't carry heavy loads (existing devices). Thus, different questions related to the aging (e.g., cellular death, lose of spines) can be addressed here [161; 162]. Finally, our device is also well suited for the study of multiple pathologies such as Parkinson [159], Alzheimer [160], multiple sclerosis [182], etc .

## 5.3 Future developments

- The resolution and the optical sectioning of our 1-photon miniaturized device can be further improved. The most direct way is by the increase of the numerical aperture of the imaging GRIN lenses [54]. For instance, imaging with a lens of  $NA = 0.8$  (instead of 0.5) will increase the theoretical lateral (XY) ( $0.61 \times \lambda / NA$ ) and axial (Z) ( $2 \times \lambda / NA^2$ ) resolutions by 38% and 61%, respectively [27]. This change will significantly improve the image quality and will also improve the quality of calcium recordings from small neuronal structures.

- Alternatively, the field of view (FOV) of our 1-photon miniaturized devices can be increased to image more neurons [46]. Different methods can be considered here, such as using a larger diameter imaging optical probes (1 mm, 1.8 mm, etc.) [54]. However, the insertion of larger probes may require brain aspiration and cause more damage to the animal [70]. Thus, this approach may be possible, but must be confirmed with biological experts. To obtain a larger

FOV with the original, small diameter (0.5 mm) imaging GRIN probes, the optical design of the miniaturised system must be reconsidered to obtain smaller magnifications [54]. The change of certain optical components (e.g., optical probe) may be inevitable here. Also it's important to mention that the smaller magnification will be less efficient for the visualisation of small neuronal features, what will be lost due to the decrease of pixels/object ratio [53].

- The optical aberrations induced by the TLCL can be further improved. Stacked design (4 TLCLs) with opposite rubbing directions (described in chapter 1) can be used to decrease the coma aberrations and the ensemble of optical aberrations [77]. In this case, individual control of TLCLs must be considered. To improve the scattering, a smaller thickness of the TLCL can be considered [183].

- Brain has plenty of different cell types (populations of neurons) that work in proximity to each other [177; 178]. A good example can be the immune cells (e.g., astrocytes) that are closely present around the neurons and that ensure the correct functioning of the neuronal circuit and to regulate the activation patterns of neurons [184; 185; 186]. To simultaneously image distinct cells types, two fluorescent markers of different colors can be considered [187]. As a result, within the same FOV, neurons can be marked with GFP (green fluorescent proteins) and for instance the astrocytes, with RFP (red fluorescent proteins) [188].

To enable the 2-color imaging within our miniaturized microscopes, double fluorescent filters and dichroic mirror must be considered. It's also important to change the excitation light source that needs to contain a larger wavelength spectrum.

- Optogenetics is a technique allowing to use the light to control neurons that have been genetically modified to express light-sensitive ion channels [189]. In this case, the hardware and optical design of the miniaturized microscopes are identical to the previously presented system (2-color). However, the difference is in the control of the light sources (red and green) that must be triggered in a specific way (depending on the user's needs). Trigger control options can be adjusted by modifying/adapting the software (LabView) interface.

- The development of a wireless variant of our miniaturized imaging system is inevitable [28; 46; 48]. The low power and voltage consumption of the TLCL will facilitate the engineering of such a device. Different modifications of the original system must be considered. First, the optical fiber must be replaced by a LED light source that is directly placed on the endoscope. Second, a miniature storage device (memory card) or a wireless microchip (bluetooth) must be installed on the miniscope. Finally, a battery must be installed to ensure the operation of the camera, the light source and the related microelectronics.

# Publication list

## Published papers

1. A. Bagramyan, "Lightweight 1-photon miniscope for imaging in freely behaving animals at subcellular resolution," *IEEE Photonics Technology Letters* **32**, 909–912 (2020).
2. A. Bagramyan, T. Galstian, "Dynamic control of polarization mismatch and coma aberrations in rod-GRIN assemblies," *Optics Express*, OE **27**, 14144–14151 (2019).
3. A. Bagramyan, A. Saghatelian, T. Galstian, "Motion-free endoscopic system for brain imaging at variable focal depth using liquid crystal lenses," *Journal of Biophotonics* **10**, 762–774 (2017).

## Submitted papers

4. A. Bagramyan, L.Tabourin, A.Rastqar, F. Bretzner, T.Galstian, "Focus-tunable microscope for imaging small neuronal processes in freely behaving animals," *submitted, Nature Methods*, 2020.

## Patents

5. T. Galstian, A. Saghatelian, A. Bagramyan, " Tunable optical device, tunable liquid crystal assembly and imaging system using same," US10631715 (2020).

# Bibliography

- [1] D. L. Farkas, C. Du, G. W. Fisher, C. Lau, W. Niu, E. S. Wachman, and R. M. Levenson, "Non-invasive image acquisition and advanced processing in optical bioimaging," *Computerized medical imaging and graphics*, vol. 22, no. 2, pp. 89–102, 1998.
- [2] T. F. Massoud and S. S. Gambhir, "Molecular imaging in living subjects: seeing fundamental biological processes in a new light," *Genes & development*, vol. 17, no. 5, pp. 545–580, 2003.
- [3] G. Giakos, M. Pastorino, F. Russo, S. Chowdhury, N. Shah, and W. Davros, "Noninvasive imaging for the new century," *IEEE Instrumentation & Measurement Magazine*, vol. 2, no. 2, pp. 32–35, 1999.
- [4] E. M. Hillman, "Optical brain imaging in vivo: techniques and applications from animal to man," *Journal of biomedical optics*, vol. 12, no. 5, p. 051402, 2007.
- [5] C. Grienberger and A. Konnerth, "Imaging calcium in neurons," *Neuron*, vol. 73, no. 5, pp. 862–885, 2012.
- [6] A. W. Snyder, "Acuity of compound eyes: physical limitations and design," *Journal of comparative Physiology*, vol. 116, no. 2, pp. 161–182, 1977.
- [7] A. W. Snyder, D. G. Stavenga, and S. B. Laughlin, "Spatial information capacity of compound eyes," *Journal of Comparative Physiology*, vol. 116, no. 2, pp. 183–207, 1977.
- [8] J. Kovac, L. Petermai, and O. Lengyel, "Advanced light emitting diodes structures for optoelectronic applications," *Thin Solid Films*, vol. 433, no. 1-2, pp. 22–26, 2003.
- [9] C. Xu and F. Wise, "Recent advances in fibre lasers for nonlinear microscopy," *Nature photonics*, vol. 7, no. 11, p. 875, 2013.
- [10] Z. Qian, L. Cao, W. Su, T. Wang, and H. Yang, *Recent advances in computer science and information engineering*. Springer Science & Business Media, 2012, vol. 1.
- [11] N. Stuurman and R. D. Vale, "Impact of new camera technologies on discoveries in cell biology," *The Biological Bulletin*, vol. 231, no. 1, pp. 5–13, 2016.

- [12] M. Ormö, A. B. Cubitt, K. Kallio, L. A. Gross, R. Y. Tsien, and S. J. Remington, "Crystal structure of the aequorea victoria green fluorescent protein," *Science*, vol. 273, no. 5280, pp. 1392–1395, 1996.
- [13] R. Y. Tsien, "The green fluorescent protein," 1998.
- [14] R. Malinow, Y. Hayashi, M. Maletic-Savatic, S. H. Zaman, J.-C. Poncer, S.-H. Shi, J. A. Esteban, P. Osten, and K. Seidenman, "Introduction of green fluorescent protein (gfp) into hippocampal neurons through viral infection," *Cold Spring Harbor Protocols*, vol. 2010, no. 4, pp. pdb-prot5406, 2010.
- [15] M. Wilson, "The Fundamentals and History of Fluorescence and Quantum Dots," Nov. 2017. [Online]. Available: <https://www.leica-microsystems.com/science-lab/the-fundamentals-and-history-of-fluorescence-and-quantum-dots/>
- [16] "Hippocampal neuron expressing GFP | Paul De Koninck Lab." [Online]. Available: <https://greenspine.ca/fr/hippocampal-neuron-expressing-gfp>
- [17] J. M. Brinkley, R. P. Haugland, and V. L. Singer, "Fluorescent microparticles with controllable enhanced stokes shift," Jul. 5 1994, uS Patent 5,326,692.
- [18] E. Rojczyk-Gołębiowska, A. Pałasz, J. J. Worthington, G. Markowski, and R. Wiaderkiewicz, "Neurolight—astonishing advances in brain imaging," *International Journal of Neuroscience*, vol. 125, no. 2, pp. 91–99, 2015.
- [19] N. Haruyama, A. Cho, and A. B. Kulkarni, "Overview: engineering transgenic constructs and mice," *Current protocols in cell biology*, vol. 42, no. 1, pp. 19–10, 2009.
- [20] M. S. Siegel and E. Y. Isacoff, "Green fluorescent proteins (gfps) for measuring voltage," *Cold Spring Harbor Protocols*, vol. 2010, no. 4, pp. pdb-top76, 2010.
- [21] M. Kneen, J. Farinas, Y. Li, and A. Verkman, "Green fluorescent protein as a noninvasive intracellular ph indicator," *Biophysical journal*, vol. 74, no. 3, pp. 1591–1599, 1998.
- [22] J. Akerboom, N. Carreras Calderón, L. Tian, S. Wabnig, M. Prigge, J. Tolö, A. Gordus, M. B. Orger, K. E. Severi, J. J. Macklin *et al.*, "Genetically encoded calcium indicators for multi-color neural activity imaging and combination with optogenetics," *Frontiers in molecular neuroscience*, vol. 6, p. 2, 2013.
- [23] J. Akerboom, T.-W. Chen, T. J. Wardill, L. Tian, J. S. Marvin, S. Mutlu, N. C. Calderón, F. Esposito, B. G. Borghuis, X. R. Sun *et al.*, "Optimization of a gcamp calcium indicator for neural activity imaging," *Journal of neuroscience*, vol. 32, no. 40, pp. 13 819–13 840, 2012.

- [24] H. Lodish, A. Berk, S. L. Zipursky, P. Matsudaira, D. Baltimore, and J. Darnell, “The action potential and conduction of electric impulses,” in *Molecular Cell Biology*. 4th edition. WH Freeman, 2000.
- [25] B. P. Bean, “The action potential in mammalian central neurons,” *Nature Reviews Neuroscience*, vol. 8, no. 6, pp. 451–465, 2007.
- [26] P. Li, X. Geng, H. Jiang, A. Caccavano, J.-y. Wu *et al.*, “Measuring sharp waves and oscillatory population activity with the genetically-encoded calcium indicator gcamp6f,” *Frontiers in cellular neuroscience*, vol. 13, p. 274, 2019.
- [27] W. Yang and R. Yuste, “In vivo imaging of neural activity,” *Nature methods*, vol. 14, no. 4, p. 349, 2017.
- [28] W. Zong and L. Chen, “Advanced miniature microscopy for brain imaging,” in *Advanced Optical Methods for Brain Imaging*. Springer, 2019, pp. 167–187.
- [29] J. Voigts and M. Harnett, “An animal-actuated rotational head-fixation system for 2-photon imaging during 2-d navigation,” *BioRxiv*, p. 262543, 2018.
- [30] R. P. Barretto, T. H. Ko, J. C. Jung, T. J. Wang, G. Capps, A. C. Waters, Y. Ziv, A. Attardo, L. Recht, and M. J. Schnitzer, “Time-lapse imaging of disease progression in deep brain areas using fluorescence microendoscopy,” *Nature medicine*, vol. 17, no. 2, pp. 223–228, 2011.
- [31] M. Leinweber, P. Zmarz, P. Buchmann, P. Argast, M. Hübener, T. Bonhoeffer, and G. B. Keller, “Two-photon calcium imaging in mice navigating a virtual reality environment,” *JoVE (Journal of Visualized Experiments)*, no. 84, p. e50885, 2014.
- [32] A. Ayaz, A. Stäuble, M. Hamada, M.-A. Wulf, A. B. Saleem, and F. Helmchen, “Layer-specific integration of locomotion and sensory information in mouse barrel cortex,” *Nature communications*, vol. 10, no. 1, pp. 1–14, 2019.
- [33] D. A. Dombeck, A. N. Khabbaz, F. Collman, T. L. Adelman, and D. W. Tank, “Imaging large-scale neural activity with cellular resolution in awake, mobile mice,” *Neuron*, vol. 56, no. 1, pp. 43–57, 2007.
- [34] Y. Hayashi, S. Yawata, K. Funabiki, and T. Hikida, “In vivo calcium imaging from dentate granule cells with wide-field fluorescence microscopy,” *PloS one*, vol. 12, no. 7, 2017.
- [35] J. Pawley, *Handbook of biological confocal microscopy*. Springer Science & Business Media, 2006, vol. 236.



- [36] K. K. Sellers, D. V. Bennett, A. Hutt, J. H. Williams, and F. Fröhlich, “Awake vs. anesthetized: layer-specific sensory processing in visual cortex and functional connectivity between cortical areas,” *Journal of neurophysiology*, vol. 113, no. 10, pp. 3798–3815, 2015.
- [37] M. T. Alkire, “Loss of effective connectivity during general anesthesia,” *International anesthesiology clinics*, vol. 46, no. 3, pp. 55–73, 2008.
- [38] W. Heinke and S. Koelsch, “The effects of anesthetics on brain activity and cognitive function,” *Current Opinion in Anesthesiology*, vol. 18, no. 6, pp. 625–631, 2005.
- [39] Z. V. Guo, S. A. Hires, N. Li, D. H. O’Connor, T. Komiyama, E. Ophir, D. Huber, C. Bonardi, K. Morandell, D. Gutnisky *et al.*, “Procedures for behavioral experiments in head-fixed mice,” *PloS one*, vol. 9, no. 2, 2014.
- [40] Y.-H. Lee, G. Tan, T. Zhan, Y. Weng, G. Liu, F. Gou, F. Peng, N. V. Tabiryan, S. Gauza, and S.-T. Wu, “Recent progress in pancharatnam–berry phase optical elements and the applications for virtual/augmented realities,” *Optical Data Processing and Storage*, vol. 3, no. 1, pp. 79–88, 2017.
- [41] R. Li, M. Wang, J. Yao, S. Liang, X. Liao, M. Yang, J. Zhang, J. Yan, H. Jia, X. Chen *et al.*, “Two-photon functional imaging of the auditory cortex in behaving mice: from neural networks to single spines,” *Frontiers in neural circuits*, vol. 12, p. 33, 2018.
- [42] P. Ravassard, A. Kees, B. Willers, D. Ho, D. Aharoni, J. Cushman, Z. M. Aghajan, and M. R. Mehta, “Multisensory control of hippocampal spatiotemporal selectivity,” *Science*, vol. 340, no. 6138, pp. 1342–1346, 2013.
- [43] Z. M. Aghajan, L. Acharya, J. J. Moore, J. D. Cushman, C. Vuong, and M. R. Mehta, “Impaired spatial selectivity and intact phase precession in two-dimensional virtual reality,” *Nature neuroscience*, vol. 18, no. 1, pp. 121–128, 2015.
- [44] L. A. Low, L. C. Bauer, M. H. Pitcher, and M. C. Bushnell, “Restraint training for awake functional brain scanning of rodents can cause long-lasting changes in pain and stress responses,” *Pain*, vol. 157, no. 8, p. 1761, 2016.
- [45] M. J. Henckens, K. van der Marel, A. van der Toorn, A. G. Pillai, G. Fernández, R. M. Dijkhuizen, and M. Joëls, “Stress-induced alterations in large-scale functional networks of the rodent brain,” *Neuroimage*, vol. 105, pp. 312–322, 2015.
- [46] D. B. Aharoni and T. Hoogland, “Circuit investigations with open-source miniaturized microscopes: past, present and future,” *Frontiers in cellular neuroscience*, vol. 13, p. 141, 2019.

- [47] K. K. Ghosh, L. D. Burns, E. D. Cocker, A. Nimmerjahn, Y. Ziv, A. El Gamal, and M. J. Schnitzer, "Miniaturized integration of a fluorescence microscope," *Nature methods*, vol. 8, no. 10, p. 871, 2011.
- [48] D. Aharoni, B. S. Khakh, A. J. Silva, and P. Golshani, "All the light that we can see: a new era in miniaturized microscopy," *Nature methods*, vol. 16, no. 1, pp. 11–13, 2019.
- [49] D. J. Cai, D. Aharoni, T. Shuman, J. Shobe, J. Biane, W. Song, B. Wei, M. Veshkini, M. La-Vu, J. Lou *et al.*, "A shared neural ensemble links distinct contextual memories encoded close in time," *Nature*, vol. 534, no. 7605, pp. 115–118, 2016.
- [50] A. D. Jacob, A. I. Ramsaran, A. J. Mocle, L. M. Tran, C. Yan, P. W. Frankland, and S. A. Josselyn, "A compact head-mounted endoscope for in vivo calcium imaging in freely behaving mice," *Current protocols in neuroscience*, vol. 84, no. 1, p. e51, 2018.
- [51] W. A. Liberti III, L. N. Perkins, D. P. Leman, and T. J. Gardner, "An open source, wireless capable miniature microscope system," *Journal of neural engineering*, vol. 14, no. 4, p. 045001, 2017.
- [52] G. Barbera, B. Liang, L. Zhang, C. R. Gerfen, E. Culurciello, R. Chen, Y. Li, and D.-T. Lin, "Spatially compact neural clusters in the dorsal striatum encode locomotion relevant information," *Neuron*, vol. 92, no. 1, pp. 202–213, 2016.
- [53] A. Bagramyan, "Lightweight 1-photon miniscope for imaging in freely behaving animals at subcellular resolution," *IEEE Photonics Technology Letters*, vol. 32, no. 15, pp. 909–912, 2020.
- [54] J. K. Kim, W. M. Lee, P. Kim, M. Choi, K. Jung, S. Kim, and S. H. Yun, "Fabrication and operation of grin probes for in vivo fluorescence cellular imaging of internal organs in small animals," *Nature protocols*, vol. 7, no. 8, p. 1456, 2012.
- [55] S. L. Resendez, J. H. Jennings, R. L. Ung, V. M. K. Namboodiri, Z. C. Zhou, J. M. Otis, H. Nomura, J. A. McHenry, O. Kosyk, and G. D. Stuber, "Visualization of cortical, subcortical and deep brain neural circuit dynamics during naturalistic mammalian behavior with head-mounted microscopes and chronically implanted lenses," *Nature protocols*, vol. 11, no. 3, p. 566, 2016.
- [56] "Inscopix." [Online]. Available: <https://www.inscopix.com>
- [57] "Doric." [Online]. Available: <http://doriclenses.com>
- [58] M. Carlén, R. M. Cassidy, H. Brismar, G. A. Smith, L. W. Enquist, and J. Frisé, "Functional integration of adult-born neurons," *Current Biology*, vol. 12, no. 7, pp. 606–608, 2002.

- [59] F. Ali and A. C. Kwan, "Interpreting in vivo calcium signals from neuronal cell bodies, axons, and dendrites: a review," *Neurophotonics*, vol. 7, no. 1, p. 011402, 2019.
- [60] F. Helmchen, M. S. Fee, D. W. Tank, and W. Denk, "A miniature head-mounted two-photon microscope: high-resolution brain imaging in freely moving animals," *Neuron*, vol. 31, no. 6, pp. 903–912, 2001.
- [61] D. R. Rivera, C. M. Brown, D. G. Ouzounov, I. Pavlova, D. Kobat, W. W. Webb, and C. Xu, "Compact and flexible raster scanning multiphoton endoscope capable of imaging unstained tissue," *Proceedings of the National Academy of Sciences*, vol. 108, no. 43, pp. 17 598–17 603, 2011.
- [62] W. Zong, R. Wu, M. Li, Y. Hu, Y. Li, J. Li, H. Rong, H. Wu, Y. Xu, Y. Lu *et al.*, "Fast high-resolution miniature two-photon microscopy for brain imaging in freely behaving mice," *Nature methods*, vol. 14, no. 7, pp. 713–719, 2017.
- [63] W. Piyawattanametha, E. D. Cocker, L. D. Burns, R. P. Barretto, J. C. Jung, H. Ra, O. Solgaard, and M. J. Schnitzer, "In vivo brain imaging using a portable 2.9 g two-photon microscope based on a microelectromechanical systems scanning mirror," *Optics letters*, vol. 34, no. 15, pp. 2309–2311, 2009.
- [64] F. Helmchen, W. Denk, and J. N. Kerr, "Miniaturization of two-photon microscopy for imaging in freely moving animals," *Cold Spring Harbor Protocols*, vol. 2013, no. 10, pp. pdb-top078 147, 2013.
- [65] B. N. Ozbay, J. T. Losacco, R. Cormack, R. Weir, V. M. Bright, J. T. Gopinath, D. Restrepo, and E. A. Gibson, "Miniaturized fiber-coupled confocal fluorescence microscope with an electrowetting variable focus lens using no moving parts," *Optics letters*, vol. 40, no. 11, pp. 2553–2556, 2015.
- [66] B. N. Ozbay, G. L. Futia, M. Ma, V. M. Bright, J. T. Gopinath, E. G. Hughes, D. Restrepo, and E. A. Gibson, "Three dimensional two-photon brain imaging in freely moving mice using a miniature fiber coupled microscope with active axial-scanning," *Scientific reports*, vol. 8, no. 1, pp. 1–14, 2018.
- [67] Y. Zhang, M. L. Akins, K. Murari, J. Xi, M.-J. Li, K. Luby-Phelps, M. Mahendroo, and X. Li, "A compact fiber-optic shg scanning endomicroscope and its application to visualize cervical remodeling during pregnancy," *Proceedings of the National Academy of Sciences*, vol. 109, no. 32, pp. 12 878–12 883, 2012.
- [68] S. Brown, "Two photons are better than one," *Nature Photonics*, vol. 2, no. 7, pp. 394–395, 2008.
- [69] "Varioptic electrowetting lenses." [Online]. Available: [www.corning.com/worldwide/en/innovation/corning-emerging-innovations/corning-variopic-lenses.html](http://www.corning.com/worldwide/en/innovation/corning-emerging-innovations/corning-variopic-lenses.html)

- [70] S. A. Lee, K. S. Holly, V. Voziyanov, S. L. Villalba, R. Tong, H. E. Grigsby, E. Glasscock, F. G. Szele, I. Vlachos, and T. A. Murray, "Gradient index microlens implanted in prefrontal cortex of mouse does not affect behavioral test performance over time," *PloS one*, vol. 11, no. 1, 2016.
- [71] S. M. Sunkin, L. Ng, C. Lau, T. Dolbeare, T. L. Gilbert, C. L. Thompson, M. Hawrylycz, and C. Dang, "Allen brain atlas: an integrated spatio-temporal portal for exploring the central nervous system," *Nucleic acids research*, vol. 41, no. D1, pp. D996–D1008, 2012.
- [72] S. Sato, "Applications of liquid crystals to variable-focusing lenses," *Optical Review*, vol. 6, no. 6, pp. 471–485, 1999.
- [73] A. Bagramyan, T. Galstian, and A. Saghatelyan, "Motion-free endoscopic system for brain imaging at variable focal depth using liquid crystal lenses," *Journal of biophotonics*, vol. 10, no. 6-7, pp. 762–774, 2017.
- [74] G. Vdovin, M. Loktev, and A. Naumov, "On the possibility of intraocular adaptive optics," *Optics Express*, vol. 11, no. 7, pp. 810–817, 2003.
- [75] T. Galstian and D. Brousseau, "Inductive coil sensor for vision corrective apparatus and methods therefor," May 14 2019, uS Patent 10,285,803.
- [76] B. Bahadur, *Liquid crystals: applications and uses*. World scientific, 1990, vol. 1.
- [77] A. Bagramyan and T. Galstian, "Dynamic control of polarization mismatch and coma aberrations in rod-grin assemblies," *Optics express*, vol. 27, no. 10, pp. 14 144–14 151, 2019.
- [78] F. Reinitzer, "Beiträge zur kenntniss des cholesterins," *Monatshefte für Chemie*, vol. 9, no. 1, pp. 421–441, 1888.
- [79] J. Pavlin, K. Susman, S. Ziherl, N. Vaupotič, and M. Čepič, "How to teach liquid crystals?" *Molecular Crystals and Liquid Crystals*, vol. 547, no. 1, pp. 255–1945, 2011.
- [80] O. Lehmann, "Über fließende krystalle," *Zeitschrift für physikalische Chemie*, vol. 4, no. 1, pp. 462–472, 1889.
- [81] J. A. Castellano, *Liquid gold: the story of liquid crystal displays and the creation of an industry*. World Scientific, 2005.
- [82] J. E. Goldmacher and J. A. Castellano, "Electro-optical compositions and devices," Nov. 17 1970, uS Patent 3,540,796.
- [83] G. Heilmeyer, L. Zanoni, and L. Barton, "Dynamic scattering in nematic liquid crystals," *Applied Physics Letters*, vol. 13, no. 1, pp. 46–47, 1968.

- [84] H. Kelker and B. Scheurle, "A liquid-crystalline (nematic) phase with a particularly low solidification point," *Angewandte Chemie International Edition in English*, vol. 8, no. 11, pp. 884–885, 1969.
- [85] V. G. Chigrinov, *Liquid crystal devices: physics and applications*, 1999.
- [86] A. Sonin, "Inorganic lyotropic liquid crystals," *Journal of Materials Chemistry*, vol. 8, no. 12, pp. 2557–2574, 1998.
- [87] G. Vertogen and W. H. De Jeu, *Thermotropic liquid crystals, fundamentals*. Springer Science & Business Media, 2012, vol. 45.
- [88] I.-C. Khoo, *Liquid crystals*. John Wiley & Sons, 2007, vol. 64.
- [89] P.-G. De Gennes and J. Prost, *The physics of liquid crystals*. Oxford university press, 1993, vol. 83.
- [90] S. Zhang, E. M. Terentjev, and A. M. Donald, "Nature of disclination cores in liquid crystals," *Liquid Crystals*, vol. 32, no. 1, pp. 69–75, 2005.
- [91] L. Guoqiang, "Adaptive lens," in *Progress in optics*. Elsevier, 2010, vol. 55, pp. 199–283.
- [92] T. V. Galstian, *Smart mini-cameras*. CRC press, 2013.
- [93] Y.-H. Lin, Y.-J. Wang, and V. Reshetnyak, "Liquid crystal lenses with tunable focal length," *Liquid Crystals Reviews*, vol. 5, no. 2, pp. 111–143, 2017.
- [94] L. M. Blinov and V. G. Chigrinov, *Electrooptic effects in liquid crystal materials*. Springer Science & Business Media, 1996.
- [95] A. Naumov, M. Y. Loktev, I. Guralnik, and G. Vdovin, "Liquid-crystal adaptive lenses with modal control," *Optics letters*, vol. 23, no. 13, pp. 992–994, 1998.
- [96] M. Ye, B. Wang, M. Uchida, S. Yanase, S. Takahashi, and S. Sato, "Focus tuning by liquid crystal lens in imaging system," *Applied Optics*, vol. 51, no. 31, pp. 7630–7635, 2012.
- [97] A. Naumov, G. Love, M. Y. Loktev, and F. Vladimirov, "Control optimization of spherical modal liquid crystal lenses," *Optics Express*, vol. 4, no. 9, pp. 344–352, 1999.
- [98] F. Goelden, A. Gaebler, O. Karabey, M. Goebel, A. Manabe, and R. Jakoby, "Tunable band-pass filter based on liquid crystal," in *German Microwave Conference Digest of Papers*. IEEE, 2010, pp. 98–101.
- [99] J. Algorri, G. Love, and V. Urruchi, "Modal liquid crystal array of optical elements," *Optics express*, vol. 21, no. 21, pp. 24 809–24 818, 2013.

- [100] G. Sprokel, "Resistivity, permittivity and the electrode space charge of nematic liquid crystals," *Molecular Crystals and Liquid Crystals*, vol. 22, no. 3-4, pp. 249–260, 1973.
- [101] P. Perkowski, D. Łada, K. Ogrodnik, J. Rutkowska, W. Piecek, and Z. Raszewski, "Technical aspects of dielectric spectroscopy measurements of liquid crystals," *Opto-Electronics Review*, vol. 16, no. 3, pp. 271–276, 2008.
- [102] J. Stöhr and M. Samant, "Liquid crystal alignment by rubbed polymer surfaces: a microscopic bond orientation model," *Journal of electron spectroscopy and related phenomena*, vol. 98, pp. 189–207, 1999.
- [103] S. Varghese, S. Narayanankutty, C. W. Bastiaansen, G. P. Crawford, and D. J. Broer, "Patterned alignment of liquid crystals by  $\mu$ -rubbing," *Advanced Materials*, vol. 16, no. 18, pp. 1600–1605, 2004.
- [104] B. Berge, "Liquid lens technology: principle of electrowetting based lenses and applications to imaging," in *18th IEEE International Conference on Micro Electro Mechanical Systems, 2005. MEMS 2005*. IEEE, 2005, pp. 227–230.
- [105] S. Sato, "Liquid-crystal lens-cells with variable focal length," *Japanese Journal of Applied Physics*, vol. 18, no. 9, p. 1679, 1979.
- [106] J. Knittel, H. Richter, M. Hain, S. Somalingam, and T. Tschudi, "Liquid crystal lens for spherical aberration compensation in a blu-ray disc system," *IEE Proceedings-Science, Measurement and Technology*, vol. 152, no. 1, pp. 15–18, 2005.
- [107] A. Tanabe, T. Hibi, S. Ipponjima, K. Matsumoto, M. Yokoyama, M. Kurihara, N. Hashimoto, and T. Nemoto, "Correcting spherical aberrations in a biospecimen using a transmissive liquid crystal device in two-photon excitation laser scanning microscopy," *Journal of biomedical optics*, vol. 20, no. 10, p. 101204, 2015.
- [108] L. Begel and T. Galstian, "Dynamic compensation of gradient index rod lens aberrations by using liquid crystals," *Applied optics*, vol. 57, no. 26, pp. 7618–7621, 2018.
- [109] T. Galstian, O. Sova, K. Asatryan, V. Presniakov, A. Zohrabyan, and M. Evensen, "Optical camera with liquid crystal autofocus lens," *Optics express*, vol. 25, no. 24, pp. 29 945–29 964, 2017.
- [110] G. Li, P. Valley, P. Äyräs, D. L. Mathine, S. Honkanen, and N. Peyghambarian, "High-efficiency switchable flat diffractive ophthalmic lens with three-layer electrode pattern and two-layer via structures," *Applied physics letters*, vol. 90, no. 11, p. 111105, 2007.

- [111] G. Li, D. L. Mathine, P. Valley, P. Äyräs, J. N. Haddock, M. Giridhar, G. Williby, J. Schwiegerling, G. R. Meredith, B. Kippelen *et al.*, “Switchable electro-optic diffractive lens with high efficiency for ophthalmic applications,” *Proceedings of the National Academy of Sciences*, vol. 103, no. 16, pp. 6100–6104, 2006.
- [112] H. E. Milton, P. B. Morgan, J. H. Clamp, and H. F. Gleeson, “Electronic liquid crystal contact lenses for the correction of presbyopia,” *Optics express*, vol. 22, no. 7, pp. 8035–8040, 2014.
- [113] T. Galstian, “Tuneable liquid crystal lens intraocular implant and methods therefor,” Oct. 16 2018, uS Patent App. 13/369,806.
- [114] Y.-H. Lin and H.-S. Chen, “Electrically tunable-focusing and polarizer-free liquid crystal lenses for ophthalmic applications,” *Optics express*, vol. 21, no. 8, pp. 9428–9436, 2013.
- [115] P. D. Gennes, J. Prost, and R. Pelcovits, “The physics of liquid crystals,” *Physics Today*, vol. 48, no. 5, p. 67, 1995.
- [116] H.-S. Chen and Y.-H. Lin, “An endoscopic system adopting a liquid crystal lens with an electrically tunable depth-of-field,” *Optics express*, vol. 21, no. 15, pp. 18 079–18 088, 2013.
- [117] C.-W. Chen, M. Cho, Y.-P. Huang, and B. Javidi, “Three-dimensional imaging with axially distributed sensing using electronically controlled liquid crystal lens,” *Optics letters*, vol. 37, no. 19, pp. 4125–4127, 2012.
- [118] T. Galstian, A. Saghatelian, and A. Bagramyan, “Tunable optical device, tunable liquid crystal lens assembly and imaging system using same,” May 17 2018, uS Patent App. 15/576,716.
- [119] R. P. Barretto and M. J. Schnitzer, “In vivo optical microendoscopy for imaging cells lying deep within live tissue,” *Cold Spring Harbor Protocols*, vol. 2012, no. 10, pp. pdb-top071 464, 2012.
- [120] L. Begel and T. Galstian, “Liquid crystal lens with corrected wavefront asymmetry,” *Applied optics*, vol. 57, no. 18, pp. 5072–5078, 2018.
- [121] T. Galstian, K. Asatryan, V. Presniakov, A. Zohrabyan, A. Tork, A. Bagramyan, S. Careau, M. Thiboutot, and M. Cotovanu, “High optical quality electrically variable liquid crystal lens using an additional floating electrode,” *Optics letters*, vol. 41, no. 14, pp. 3265–3268, 2016.
- [122] B. Wang, M. Ye, and S. Sato, “Liquid crystal lens with stacked structure of liquid-crystal layers,” *Optics communications*, vol. 250, no. 4-6, pp. 266–273, 2005.

- [123] C.-T. Lee, Y. Li, H.-Y. Lin, and S.-T. Wu, "Design of polarization-insensitive multi-electrode grin lens with a blue-phase liquid crystal," *Optics express*, vol. 19, no. 18, pp. 17 402–17 407, 2011.
- [124] Y. Li and S.-T. Wu, "Polarization independent adaptive microlens with a blue-phase liquid crystal," *Optics express*, vol. 19, no. 9, pp. 8045–8050, 2011.
- [125] R. Bao, C. Cui, S. Yu, H. Mai, X. Gong, and M. Ye, "Polarizer-free imaging of liquid crystal lens," *Optics express*, vol. 22, no. 16, pp. 19 824–19 830, 2014.
- [126] T. Galstian and K. Allahverdyan, "Focusing unpolarized light with a single-nematic liquid crystal layer," *Optical Engineering*, vol. 54, no. 2, p. 025104, 2015.
- [127] M. Wahle, B. Snow, J. Sargent, and J. C. Jones, "Embossing reactive mesogens: A facile approach to polarization-independent liquid crystal devices," *Advanced Optical Materials*, vol. 7, no. 2, p. 1801261, 2019.
- [128] H.-S. Chen, Y.-J. Wang, C.-M. Chang, and Y.-H. Lin, "A polarizer-free liquid crystal lens exploiting an embedded-multilayered structure," *IEEE Photonics Technology Letters*, vol. 27, no. 8, pp. 899–902, 2015.
- [129] H. Takehara, Y. Ohta, M. Motoyama, M. Haruta, M. Nagasaki, H. Takehara, T. Noda, K. Sasagawa, T. Tokuda, and J. Ohta, "Intravital fluorescence imaging of mouse brain using implantable semiconductor devices and epi-illumination of biological tissue," *Biomedical optics express*, vol. 6, no. 5, pp. 1553–1564, 2015.
- [130] V. Szabo, C. Ventalon, V. De Sars, J. Bradley, and V. Emiliani, "Spatially selective holographic photoactivation and functional fluorescence imaging in freely behaving mice with a fiberscope," *Neuron*, vol. 84, no. 6, pp. 1157–1169, 2014.
- [131] A. Attardo, J. E. Fitzgerald, and M. J. Schnitzer, "Impermanence of dendritic spines in live adult ca1 hippocampus," *Nature*, vol. 523, no. 7562, p. 592, 2015.
- [132] E. J. Hamel, B. F. Grewe, J. G. Parker, and M. J. Schnitzer, "Cellular level brain imaging in behaving mammals: an engineering approach," *Neuron*, vol. 86, no. 1, pp. 140–159, 2015.
- [133] B. F. Grewe, F. F. Voigt, M. van't Hoff, and F. Helmchen, "Fast two-layer two-photon imaging of neuronal cell populations using an electrically tunable lens," *Biomedical optics express*, vol. 2, no. 7, pp. 2035–2046, 2011.
- [134] Y. Zou, W. Zhang, F. S. Chau, and G. Zhou, "Miniature adjustable-focus endoscope with a solid electrically tunable lens," *Optics express*, vol. 23, no. 16, pp. 20 582–20 592, 2015.



- [135] P. Yeh and C. Gu, *Optics of liquid crystal displays*. John Wiley & Sons, 2009, vol. 67.
- [136] LensVector, *The Solid-State Autofocus Solution*, 2016. [Online]. Available: [lensvector.com](http://lensvector.com)
- [137] M. Bass, C. DeCusatis, J. Enoch, V. Lakshminarayanan, G. Li, C. Macdonald, V. Mahajan, and E. Van Stryland, *Handbook of optics, Volume II: Design, fabrication and testing, sources and detectors, radiometry and photometry*. McGraw-Hill, Inc., 2009.
- [138] F. Kahn, “Electronically variable iris or stop mechanisms,” Jun. 26 1973, uS Patent 3,741,629.
- [139] M. Y. Loktev, V. Belopukhov, F. Vladimirov, G. Vdovin, G. Love, and A. Naumov, “Wave front control systems based on modal liquid crystal lenses,” *Review of Scientific Instruments*, vol. 71, no. 9, pp. 3290–3297, 2000.
- [140] L. Li, D. Bryant, and P. J. Bos, “Liquid crystal lens with concentric electrodes and inter-electrode resistors,” *Liquid Crystals Reviews*, vol. 2, no. 2, pp. 130–154, 2014.
- [141] H. Ren, Y.-H. Fan, S. Gauza, and S.-T. Wu, “Tunable-focus flat liquid crystal spherical lens,” *Applied physics letters*, vol. 84, no. 23, pp. 4789–4791, 2004.
- [142] B. Wang, M. Ye, and S. Sato, “Lens of electrically controllable focal length made by a glass lens and liquid-crystal layers,” *Applied optics*, vol. 43, no. 17, pp. 3420–3425, 2004.
- [143] K. Asatryan, V. Presnyakov, A. Tork, A. Zohrabyan, A. Bagramyan, and T. Galstian, “Optical lens with electrically variable focus using an optically hidden dielectric structure,” *Optics express*, vol. 18, no. 13, pp. 13 981–13 992, 2010.
- [144] A. Hassanfiroozi, Y.-P. Huang, B. Javidi, and H.-P. D. Shieh, “Hexagonal liquid crystal lens array for 3d endoscopy,” *Optics express*, vol. 23, no. 2, pp. 971–981, 2015.
- [145] T. Galstian, V. Presniakov, K. Asatryan, A. Tork, A. Zohrabyan, and A. Bagramyan, “Electro-optical devices using dynamic reconfiguration of effective electrode structures,” Oct. 11 2011, uS Patent 8,033,054.
- [146] V. Breton-Provencher, D. Coté, and A. Saghatelian, “Activity of the principal cells of the olfactory bulb promotes a structural dynamic on the distal dendrites of immature adult-born granule cells via activation of nmda receptors,” *Journal of Neuroscience*, vol. 34, no. 5, pp. 1748–1759, 2014.
- [147] N. Tamamaki, Y. Yanagawa, R. Tomioka, J.-I. Miyazaki, K. Obata, and T. Kaneko, “Green fluorescent protein expression and colocalization with calretinin, parvalbumin, and somatostatin in the gad67-gfp knock-in mouse,” *Journal of Comparative Neurology*, vol. 467, no. 1, pp. 60–79, 2003.

- [148] J. Sun, S. J. Lee, L. Wu, M. Sarntinoranont, and H. Xie, "Refractive index measurement of acute rat brain tissue slices using optical coherence tomography," *Optics express*, vol. 20, no. 2, pp. 1084–1095, 2012.
- [149] R. W. Cole, T. Jinadasa, and C. M. Brown, "Measuring and interpreting point spread functions to determine confocal microscope resolution and ensure quality control," *Nature protocols*, vol. 6, no. 12, p. 1929, 2011.
- [150] D. Miyamoto and M. Murayama, "The fiber-optic imaging and manipulation of neural activity during animal behavior," *Neuroscience research*, vol. 103, pp. 1–9, 2016.
- [151] O. Sadakane, A. Watakabe, M. Ohtsuka, M. Takaji, T. Sasaki, M. Kasai, T. Isa, G. Kato, J. Nabekura, H. Mizukami *et al.*, "In vivo two-photon imaging of dendritic spines in marmoset neocortex," *eNeuro*, 2015.
- [152] W. Mittmann, D. J. Wallace, U. Czubayko, J. T. Herb, A. T. Schaefer, L. L. Looger, W. Denk, and J. N. Kerr, "Two-photon calcium imaging of evoked activity from 15 somatosensory neurons in vivo," *Nature neuroscience*, vol. 14, no. 8, pp. 1089–1093, 2011.
- [153] A. Glas, M. Hübener, T. Bonhoeffer, and P. M. Goltstein, "Benchmarking miniaturized microscopy against two-photon calcium imaging using single-cell orientation tuning in mouse visual cortex," *PloS one*, vol. 14, no. 4, 2019.
- [154] T. Francis, R. Chandra, A. Gaynor, P. Konkalmatt, S. Metzbower, B. Evans, M. Engeln, T. Blanpied, and M. Lobo, "Molecular basis of dendritic atrophy and activity in stress susceptibility," *Molecular psychiatry*, vol. 22, no. 11, pp. 1512–1519, 2017.
- [155] F. Szele, C. Alexander, and M. Chesselet, "Expression of molecules associated with neuronal plasticity in the striatum after aspiration and thermocoagulatory lesions of the cerebral cortex in adult rats," *Journal of Neuroscience*, vol. 15, no. 6, pp. 4429–4448, 1995.
- [156] F. G. Szele and M.-F. Chesselet, "Cortical lesions induce an increase in cell number and psa-ncam expression in the subventricular zone of adult rats," *Journal of Comparative Neurology*, vol. 368, no. 3, pp. 439–454, 1996.
- [157] S. Gulati, V. Y. Cao, and S. Otte, "Multi-layer cortical ca<sup>2+</sup> imaging in freely moving mice with prism probes and miniaturized fluorescence microscopy," *JoVE (Journal of Visualized Experiments)*, no. 124, p. e55579, 2017.
- [158] A. Li, W. Liang, H. Guan, Y.-T. A. Gau, D. E. Bergles, and X. Li, "Focus scanning with feedback-control for fiber-optic nonlinear endomicroscopy," *Biomedical optics express*, vol. 8, no. 5, pp. 2519–2527, 2017.

- [159] Y. Smith, R. Villalba, and D. Raju, "Striatal spine plasticity in parkinson's disease: pathological or not?" *Parkinsonism & related disorders*, vol. 15, pp. S156–S161, 2009.
- [160] T. Bittner, M. Fuhrmann, S. Burgold, S. M. Ochs, N. Hoffmann, G. Mitteregger, H. Kretzschmar, F. M. LaFerla, and J. Herms, "Multiple events lead to dendritic spine loss in triple transgenic alzheimer's disease mice," *PloS one*, vol. 5, no. 11, 2010.
- [161] D. L. Dickstein, C. M. Weaver, J. I. Luebke, and P. R. Hof, "Dendritic spine changes associated with normal aging," *Neuroscience*, vol. 251, pp. 21–32, 2013.
- [162] M. L. Feldman and C. Dowd, "Loss of dendritic spines in aging cerebral cortex," *Anatomy and embryology*, vol. 148, no. 3, pp. 279–301, 1975.
- [163] V. Breton-Provencher, K. Bakhshetyan, D. Hardy, R. R. Bammann, F. Cavarretta, M. Snappyan, D. Côté, M. Migliore, and A. Saghatelian, "Principal cell activity induces spine relocation of adult-born interneurons in the olfactory bulb," *Nature communications*, vol. 7, p. 12659, 2016.
- [164] J. Oh, C. Lee, and B.-K. Kaang, "Imaging and analysis of genetically encoded calcium indicators linking neural circuits and behaviors," *The Korean Journal of Physiology & Pharmacology*, vol. 23, no. 4, pp. 237–249, 2019.
- [165] I. Mollinedo-Gajate, C. Song, and T. Knöpfel, "Genetically encoded fluorescent calcium and voltage indicators," 2019.
- [166] E. Greotti and D. De Stefani, "Biosensors for detection of calcium," in *Methods in Cell Biology*. Elsevier, 2020, vol. 155, pp. 337–368.
- [167] O. Mano, M. S. Creamer, C. A. Matulis, E. Salazar-Gatzimas, J. Chen, J. A. Zavatone-Veth, and D. A. Clark, "Using slow frame rate imaging to extract fast receptive fields," *Nature communications*, vol. 10, no. 1, pp. 1–13, 2019.
- [168] A. Bagramyan, "Lightweight 1-photon miniscope for imaging in freely behaving animals at subcellular resolution," *IEEE PTL*, 2020.
- [169] J. I. Arellano, R. Benavides-Piccione, J. DeFelipe, and R. Yuste, "Ultrastructure of dendritic spines: correlation between synaptic and spine morphologies," *Frontiers in neuroscience*, vol. 1, p. 10, 2007.
- [170] W. Lee and S. Yun, "Adaptive aberration correction of grin lenses for confocal endomicroscopy," *Optics letters*, vol. 36, no. 23, pp. 4608–4610, 2011.
- [171] B. Ruszczycki, Z. Szepesi, G. M. Wilczynski, M. Bijata, K. Kalita, L. Kaczmarek, and J. Włodarczyk, "Sampling issues in quantitative analysis of dendritic spines morphology," *BMC bioinformatics*, vol. 13, no. 1, p. 213, 2012.

- [172] M. Balbi, M. P. Vanni, G. Silasi, Y. Sekino, L. Bolanos, J. M. LeDue, and T. H. Murphy, "Targeted ischemic stroke induction and mesoscopic imaging assessment of blood flow and ischemic depolarization in awake mice," *Neurophotonics*, vol. 4, no. 3, p. 035001, 2017.
- [173] B. Ellenbroek and J. Youn, "Rodent models in neuroscience research: is it a rat race?" *Disease models & mechanisms*, vol. 9, no. 10, pp. 1079–1087, 2016.
- [174] D. Ball, R. Kliese, F. Windels, C. Nolan, P. Stratton, P. Sah, and J. Wiles, "Rodent scope: a user-configurable digital wireless telemetry system for freely behaving animals," *PLoS One*, vol. 9, no. 2, 2014.
- [175] A. Sansone, "A tiny macroscope to look into complex behavior," *Nature methods*, vol. 16, no. 1, pp. 22–22, 2019.
- [176] E. C. Bryda, "The mighty mouse: the impact of rodents on advances in biomedical research," *Missouri medicine*, vol. 110, no. 3, p. 207, 2013.
- [177] E. T. Rolls, A. Treves, and E. T. Rolls, *Neural networks and brain function*. Oxford university press Oxford, 1998, vol. 572.
- [178] O. Sporns, "Network analysis, complexity, and brain function," *Complexity*, vol. 8, no. 1, pp. 56–60, 2002.
- [179] H. Kasai, M. Matsuzaki, J. Noguchi, N. Yasumatsu, and H. Nakahara, "Structure–stability–function relationships of dendritic spines," *Trends in neurosciences*, vol. 26, no. 7, pp. 360–368, 2003.
- [180] M. E. Hatten, "Central nervous system neuronal migration," *Annual review of neuroscience*, vol. 22, no. 1, pp. 511–539, 1999.
- [181] K. Jin, Y. Sun, L. Xie, S. Batteur, X. O. Mao, C. Smelick, A. Logvinova, and D. A. Greenberg, "Neurogenesis and aging: Fgf-2 and hb-egf restore neurogenesis in hippocampus and subventricular zone of aged mice," *Aging cell*, vol. 2, no. 3, pp. 175–183, 2003.
- [182] M. J. Fogarty, E. W. Mu, P. G. Noakes, N. A. Lavidis, and M. C. Bellingham, "Marked changes in dendritic structure and spine density precede significant neuronal death in vulnerable cortical pyramidal neuron populations in the sod1 g93a mouse model of amyotrophic lateral sclerosis," *Acta neuropathologica communications*, vol. 4, no. 1, p. 77, 2016.
- [183] S.-T. Wu and K.-C. Lim, "Absorption and scattering measurements of nematic liquid crystals," *Applied optics*, vol. 26, no. 9, pp. 1722–1727, 1987.

- [184] A. Araque and M. Navarrete, “Glial cells in neuronal network function,” *Philosophical Transactions of the Royal Society B: Biological Sciences*, vol. 365, no. 1551, pp. 2375–2381, 2010.
- [185] W. Boesmans, M. A. Martens, N. Weltens, M. M. Hao, J. Tack, C. Cirillo, and P. Vanden Berghe, “Imaging neuron-glia interactions in the enteric nervous system,” *Frontiers in cellular neuroscience*, vol. 7, p. 183, 2013.
- [186] A. Volterra, N. Liaudet, and I. Savtchouk, “Astrocyte  $Ca^{2+}$  signalling: an unexpected complexity,” *Nature Reviews Neuroscience*, vol. 15, no. 5, pp. 327–335, 2014.
- [187] L. Abdeladim, K. S. Matho, S. Clavreul, P. Mahou, J.-M. Sintes, X. Solinas, I. Arganda-Carreras, S. G. Turney, J. W. Lichtman, A. Chessel *et al.*, “Multicolor multiscale brain imaging with chromatic multiphoton serial microscopy,” *Nature communications*, vol. 10, no. 1, pp. 1–14, 2019.
- [188] P. Kelly, E. Hudry, S. S. Hou, and B. J. Bacsikai, “In vivo two photon imaging of astrocytic structure and function in alzheimer’s disease,” *Frontiers in aging neuroscience*, vol. 10, p. 219, 2018.
- [189] K. Deisseroth, “Optogenetics,” *Nature methods*, vol. 8, no. 1, pp. 26–29, 2011.